Effects of Cyclical Load Conditions on Wear Rate and Wear Scar in a Modified ASTM G65 Abrasion Test

by

Mark Curley

A thesis submitted in partial fulfillment of the requirements for the degree of

Master of Science

In

Mining Engineering

Department of Civil and Environmental Engineering
University of Alberta

ABSTRACT

Wear is an incredibly complicated phenomenon that can occur in many different forms, through a number of modes, facilitated by a variety of mechanisms. Surface mining operations are particularly afflicted by abrasive wear; principally during the excavation process. Shovel geometry has been analyzed and resolved to determine the intensity of abrasive forces acting at the dipper teeth; the predominant site of abrasive wear attack.

Raw field data was scaled down to appropriate laboratory magnitudes in order to facilitate laboratory wear testing. Accurate prediction and classification of wear in a lab setting is crucial to industry, as it provides a quick and rather inexpensive means to better assess wear attack.

A current standardized test often employed by industry is the ASTM G65 Dry Sand/Rubber Wheel Abrasion Test. This test utilizes a rounded quartz grain abrasive, a constant normal load and a predetermined lineal abrasion distance. In order to better reflect practical mining conditions, this standardized test was modified to allow for adjustable load conditions combined with an abrasive media representative of an oil sands mining operation. An apparatus was designed to incorporate a load varying instrument and electrical devices to record the power draw and ultimately calculate the energy used during the abrasion process.

The application of a load varying instrument was successful in mimicking electric shovel digging patterns. Cyclical loading better predicted shovel tooth life in an oil sands operation than its constant load counterpart. Inspection of the wear scars suggests constant and repeated loading conditions generate wear with different levels of severity; cyclical conditions being more damaging.

PREFACE

This thesis is an original work by Mark Curley. The thesis has not been published in part or in full previously. The field data used for analysis in this thesis was provided by Dr. Tim Joseph of the University of Alberta. The geometric analysis of forces acting on cable shovels shown in Chapter 3 was completed by the author and a fellow colleague, Steven Duncan, based off of work completed by Dr. Tim Joseph and Dr. Ning Shi. The technical apparatus described in Section 4.3 was designed and assembled by the author and Lucas Duerksen based off of the ASTM G65 wear test. Optical and SEM images were taken with the help and assistance of Jason Wang at the CCWJ and Nathan Gerein from the Department of Earth and Atmospheric Sciences.

I dedicate this work to Gramma B and my family.

It is their love and support that drives me to success.

ACKNOWLEDGEMENTS

The completion of this work would not have been possible without the help of several groups and individuals that made it possible;

Dr. Szymanski, you were a dedicated professor, a thoughtful and caring supervisor, and a very kind man. Your input and practice of checking on my progress was always appreciated, as was your confidence in my ability to work on my own. Thank you for your time as my professor, graduate supervisor, and friend.

Dr. Tim Joseph was an invaluable resource throughout the entire Master's program. His initial encouragement to apply for graduate studies was a major driving factor in my decision to take the grad student leap. Dr. Joseph provided guidance on which courses to take, supplied and helped analyze the raw field data, and most importantly offered extra support and time after Dr. Szymanski's passing.

I am very grateful to the CCWJ and its supervisors, especially Dr. Leijun Li and Dr. Patricio Mendez, for being very welcoming and accommodating throughout my partnership with them. Dr. Li was also extremely generous with his support and guidance in writing and formatting this thesis. Special thanks to Jason Wang for his help on preparing samples and images from the Scanning Electron Microscope. Thanks to Nairn Barnes and Gentry Wood who were instrumental in obtaining the chromium carbide samples and providing the equipment and lab space to prepare them.

Gratitude is extended to the Department of Earth and Atmospheric Sciences and the scanning electron microscope technician, Nathan Gerein, for taking time out of his day to provide instruction on how to operate and take micrographs of the abrasive and coupon samples.

Special thanks go to Wilkinson Steel and Metals for graciously supplying the samples free of charge, and for providing their support in the goals of this paper. Thanks also go out to Syncrude for supplying the abrasive material used in the tests.

Finally, thank you to my parents Stu and Linda, and my sister, Laura for their continual support throughout my undergrad and graduate studies. The encouraging and supporting atmosphere they create at home is a necessary and relieving contrast to the occasional long days in the laboratory.

TABLE OF CONTENTS

ABSTRACT ii

PREFACE iii

ACKNOWLEDGEMENTS v

LIST OF TABLES ix

LIST OF FIGURES x

LIST OF SYMBOLS xii

GLOSSARY OF TERMS xiv

1 INTRODUCTION 1

1.1 Outline and Objectives 2

2 LITERATURE REVIEW 3

2.1 Alberta's Oil Sands 3

2.1.1 Lithology of the Oil Sands 4

2.1.2 Abrasivity of Oil Sands 5

2.2 Wear in the Surface Mining Industry 5

2.2.1 Adhesion 6

2.2.2 Erosion 6

2.2.3 Corrosion 6

2.2.4 Abrasive Wear 6

2.3 Advances in Abrasive Wear Resistant Materials and Surfacing Techniques 10

2.3.1 Ferrous-based resistant materials 10

2.3.2 Surface Engineering Techniques 11

2.3.3 Elastomers and polymers 11

2.3.4 Ceramics and Cermets 11

2.4 Current Abrasion Tests and Wear Modelling Capabilities 12

2.4.1 Industry Recognized Standardized Abrasive Tests 12

2.4.2 Abrasive Wear Modelling and Prediction Techniques 18

2.5 A Brief Overview of Cable Shovels 22

2.5.1 Operation and General Components of a Cable Shovel 23

2.5.2 GET Interaction with Mining Face 23

2.5.3 Previous GET Models of Kinematics and Geometry 24

2.6 Summary 26

3 DETERMINATION OF RESISTIVE FORCES 27

3.1 Input information required from field 27

3.2 Analyzing Field Data 28

3.2.1 Determination of the digging profile 28

3.2.2 Dig Cycle Trajectory 33

3.3 Determination of Resistive Forces 34

3.3.1 Bucket/Material Weight Moment 34

3.3.2 Handle Weight Moment 35

3.3.3 Hoist Force Moment 37

3.3.4 Total Resistive Moment 39

3.4 Scaling of Field Force Values 43

3.4.1 General Scaling Laws 44

3.4.2 Determining a Scaling Factor 44

3.4.3 Field Force Values 45

4 EXPERIMENTAL PROCEDURE 46

4.1 Characteristics of Abrasives 47

4.1.1 Stripped Oil Sand Particle Size Distribution 50

4.1.2 Friction Angle 50

4.2 Specimen Specifications 51

4.2.1 Coupon Preparation 51

4.2.2 Submerged Arc Weld Parameters 53

4.3 Modified Testing Apparatus 55

4.3.1 Linear Actuator 55

4.3.2 Wheel and Hopper 55

4.4 Modified G65 Test Procedure 56

4.4.1 Outline of Modified Test Sequence 57

4.4.2 Outline of Constant Load Test 57
4.5 Modified Test Parameters 58
5 EXPERIMENTAL RESULTS 60
5.1 Load Varying Capability 60
5.2 Coupon Volume Loss 62
5.2.1 Variably Loaded Coupons 62
5.2.2 Constantly Loaded Coupons 64
5.3 Power Draw & Abrasion Energy 65
5.3.1 Field Data Power Draw 65
5.3.2 Modified Apparatus Power Draw 66
5.3.3 Comparison of Field and Lab Data 67
5.4 Prediction of Field Wear 68
5.4.1 Field Specific Energy 68
5.4.2 Lab Specific Energy 69
5.4.3 Comparing Specific Energies 69
5.4.4 Determining Tooth Life in the Field 70
5.5 Examination of Surface Wear Scar 70
5.5.1 Standard Test Incorporating Dipper Velocity and Modified Distance 71
5.5.2 Investigation of Wear Scar 71
6 DISCUSSION 74
6.1 Raw Force Data Input 74
6.2 Coupon Wear 75
6.2.1 Volume Loss 75
6.2.2 Wear Scars 76
6.3 Power and Energy 76
6.3.1 Field Data 76
6.3.2 Lab Tests 77
6.4 Field Wear Prediction 77
6.5 Contrast of Cyclic and Constant Loading Wear Scars 78

6.5.1 Volume Loss 78
6.5.2 Possibility of Fatigue Wear 79
6.6 Test Adaptability 79
6.7 Issues Encountered 80
7 CONCLUSIONS AND RECOMMENDATIONS 81
7.1 Conclusion 81
7.2 Recommendations 82
8 WORKS CITED 83
Appendix A Sample Raw Data 87
Appendix B Abrasive Media SEM Images 88
Appendix C Additional Coupon Images 93
Appendix D Coupon Loading Patterns 104
Appendix E – Additional Power Draw Graphs 113
Appendix F – Additional Field Wear Predictions 115

LIST OF TABLES

Table 2.1 – Select properties of oil sands (Adapted from Dusseault & Morgenstern, 1978) 4
Table 2.2 - Factors contributing to wear attack severity (Adapted from Hawk & Wilson, 2001) ... 9
Table 2.3 – Characteristics & applications of ferrous-based materials (After Llewellyn, 1996) 10
Table 2.4 - Abrasion and Erosion Test Procedures (Adapted from Hawk, 2000) 12
Table 2.5 - Standard DSRW Abrasion Test Parameters (After Hawk, 2000) 14
Table 2.6 - Procedure outlining the standard WSRW Test 17
Table 3.1 - Field force values and the applied scale & lever arm factors 45
Table 4.1 - Field and lab force categories for the three cyclical test variations 59
Table 4.2 - Test matrix comparing modified and standard G65 tests 59
Table 5.1 - Data after 525 m of lineal abrasion at various normal loads 62
Table 5.2 - Comparison of average volume loss between cyclic and constant load tests 65
Table 5.3 - Comparison of Power and Energy values per field and test cycle 67
Table 5.4 - Mass and Volume Loss data for field shovel teeth 68
Table 5.5 - Energy per unit volume, Field vs. Lab 69
Table 5.6 - Tooth life prediction 70
Table 5.7 - Coupon volume losses from supplementary test 71

LIST OF FIGURES

Figure 2.1 - The hydrophilic tendency of oil sand is crucial for extraction (After Bott, 2011) 3
Figure 2.2 - Uniform quartz grains (white) and bitumen-filled pore spaces (black) (Adapted from Mossop, 1980)........5
Figure 2.3 - Illustrative example of some wear types encountered in mining (Adapted from Hawk & Wilson, 2001)........8
Figure 2.4 - Wear mechanisms on the microscopic scale (After Hawk & Wilson, 2001) 9
Figure 2.5 - Basic setup of DSRW testing apparatus (Adapted from ASTM G65)........13
Figure 2.6 - Schematic of the WSRW Test (Modified from Hawk, 2000) 17
Figure 2.7 - Abrasive wear of ductile material (a) and of brittle material (b) (After Kato & Adachi, 2001) 19
Figure 2.8 - Simple model of abrasive wear by a conical particle (Adapted from Kato & Adachi, 2001) 20
Figure 2.9 - Visual representation of vector translation in microscale dynamic model (After Li *et al.*, 1999) 22
Figure 2.10 - Schematic of P&H 4100 BOSS Cable Shovel (Adapted from Humphrey & Wagner, 2011) 24
Figure 2.11 - Hydraulic shovel geometry (Adapted from Frimpong & Hu, 2004) 25
Figure 2.12 - General dipper-handle free body diagram (After Joseph & Shi, 2012)........25
Figure 3.1 - General diagram of ultra-class mining shovel (Adapted from Joseph & Shi, 2011)..29
Figure 3.2 - More detailed geometry in X-Y plane 30
Figure 3.3 - Layout to derive motion of dipper teeth in X-Y plane (Modified from Joseph & Shi, 2011) 31
Figure 3.4 - Geometric relation of tooth tip to 2-D plane 32
Figure 3.5 - Approximate digging profiles of first three passes 33
Figure 3.6 - Moment arm of dipper & material acting about the saddle........35
Figure 3.7 - Location of handle forces acting about the saddle block........36
Figure 3.8 - Hoist and normal resistive forces shown for dig cycle 1 37
Figure 3.9 - Geometry used to determine hoist moment arm........38
Figure 3.10 - Approach used to determine digging resistance angle from horizontal........40
Figure 3.11 - Geometry of resistance moment arm 41
Figure 3.12 - Geometry of the total resistance moment arm........42
Figure 3.13 - Resolving total resistive force at tooth tip to a normal force 43
Figure 3.14 - Small and large triangles showing the area square law (after Denker, 2015)........44
Figure 4.1 - Close-up image of tailings sand abrasive. Magnification 200x........47
Figure 4.2 - Alternate close-up of tailings sand abrasive material. Magnification 200x 48

Figure 4.3 - Zoomed out image of tailings abrasive sample. Magnification 100x 48
Figure 4.4 - Close-up image of rounded quartz grain abrasive. Magnification 70X 49
Figure 4.5 - Grain size distribution of tailings sand used in modified G65 test 50
Figure 4.6 - Sample coupon before surface grinding had taken place 51
Figure 4.7 - Sample coupon after surface grinding, ready for testing (a) width (b) length 52
Figure 4.8 - Side-view of overlay deposit on base substrate 52
Figure 4.9 - General outline of the SAW process. Weld direction is left to right 53
Figure 4.10 - Image of coupon surface prior to wear testing 54
Figure 4.11 - SEM image of carbides on a sample coupon. Carbides represented by darker grey shaded areas 54
Figure 4.12 - Setup of the modified testing apparatus 56
Figure 4.13 - Outline of proposed modified test 58
Figure 5.1 - Cyclic load pattern on sample coupon 60
Figure 5.2 - Two cycles showing 3 second ramp up period and constant force 61
Figure 5.3 - Image taken at centre of wear scar. Wear direction is right to left 63
Figure 5.4 - Image at same location as Figure 5.3 – dark grey shapes represents carbides 63
Figure 5.5 - Comparison of total volume loss with normal force on coupon 64
Figure 5.6 - Graphs of power draw during typical dig cycles 66
Figure 5.7 - Power Draw of Modified Apparatus at 301 N Normal Force 67
Figure 5.8 - Optical microscope image of the constant load cross-section 72
Figure 5.9 - Optical microscope image of the varied load cross-section 72
Figure 5.10 - SEM image of the constant load cross-section 73
Figure 5.11 - SEM image of the varied load cross-section 73

LIST OF SYMBOLS

A	Bail Point
A'	Availability of the shovel
A_{Tp}	Tooth-area proportion
C_{BC}	Crowd Teeth to bucket + ore centroid
C_e	Crowd Extension
C_H	Crowd Teeth to end of handle
C_L	Crowd Linkage
C_{LT}	Crowd Teeth to tooth tip
C_t	Saddle Block to Bail Point (Crowd)
E_{Avg}	Average field energy per cycle
E_{Fc}	Field energy per cycle, per tooth
E_L	Energy in lab per abrasion cycle
E_{Sl}	Lab Specific Energy
E_{Sf}	Field Specific Energy
F_h	Hoist Force
F_R	Total Resistive Force
F_{Rn}	Normal Resistive Force
g	Acceleration due to gravity
G_{bucket}	Empty bucket weight
G_{ore}	Total weight of ore in bucket
GPa	Giga pascals, unit of pressure
H_e	Handle Extension
$H_{e'}$	Handle Length opposite of Saddle Point
H_L	Total Handle Length
H_W	Handle Weight
H_v	Vickers Hardness
J	Joules, unit of energy
L_{b+o}	Moment arm of bucket and ore
L_h	Moment arm of Hoist Force
L_h	Moment arm of shovel handle
L_{OC}	Saddle Block to tooth tip
L_{PC}	Sheave to tooth tip
L_R	Moment arm of Total Resistive Force
M_{b+o}	Moment from bucket + ore
M_h	Moment from handle

M_{hf}	Moment from hoist force
M_T	Total Moment about saddle block
O	Saddle Block
P	Sheave Wheel centre
P'	Sheave Wheel edge
r_s	Sheave Wheel radius
r_b	Radius of Saddle Block to Bail Point
SF	Swell Factor
ScF	Scale Factor
T	Predicted life time of tooth in field, in hours
T_c	Cycle time for one complete dig cycle
TF	Time Frame of volume loss consideration
U'	Utilization of the shovel
V_L	Volume loss measured from lab samples
V_{Lf}	Volume loss measured from field tooth
V_B	Bucket Volume
W	Boom Length
Z_e	Hoist Extension
Z_L	Hoist Linkage
Z_t	Sheave to Bail Point (Hoist)
α	Saddle – Bail – Sheave Angle
β	Dipper rake angle
γ	Handle angle from horizontal
γ_1	Angle between horizontal and C_t
γ_2	Angle between C_t and the Boom
$\Delta\gamma$	Angle from handle to C_t
δ	Tooth-oil sand friction angle
θ	Angle between Sheave – Bail – Sheave Edge
ρ	Density of oil sand
τ	Angle of handle plus rake
χ	Boom angle from horizontal
ψ	Resistive force angle
ω	Internal tooth angle

GLOSSARY OF TERMS

Term	Definition
Abrasion	Form of wear which occurs when a hard surface, or soft surface containing hard particles, slides on a softer surface. Generally a series of grooves are formed
Actuator	Cylinder that extends and retracts in a linear movement
API	American Petroleum Institute
ASTM	American Society for Testing and Materials
Bitumen	Very dense, viscous form of petroleum
Coupon	Small rectangular samples that are subjected to the abrasive wear tests
Dipper	Refers to the bucket on an excavator
DSRW	Dry-sand rubber-wheel
Durometer	Scale developed by A. Shore to measure Shore hardness. Durometer is used to refer to the measurement and the instrument itself
Fatigue Wear	Contacts between asperities are repeated a number of times. Plastic deformation can cause crack initiation, growth, and failure
GETs	Ground Engaging tools
Hydrophilic	Having a strong affinity for water. Athabasca oil sand itself is water wettable
Load Cell	A device that converts mechanical force into an electrical output signal
Moment	Tendency of a force to rotate an object around an axis or pivot point
Oil Sand	Naturally occurring mixture of sand, water, clay and bitumen. Must be treated and refined before use as fuels such as gasoline or diesel
Overlay	Resistant layer of material applied to a base substrate via welding technique
Post-Hydro oil sand	Oil sand stripped of bitumen that has been hydro-transported via pipeline
PTAW	Plasma transferred arc weld
SAW	Submerged arc weld
SEM	Scanning Electron Microscope
Wear	Removal of material as a result of mechanical actions

1 INTRODUCTION

Surface mining is a continuous process of extracting raw minerals from the Earth through means of excavating and transporting material. Throughout all mining processes, equipment is subjected to external forces and must constantly be maintained or replaced. Wear is a critical factor in both production rate and maintenance costs in all mining operations. Rabinowicz (1965) described wear as “the removal of material from solid surfaces as a result of mechanical action”. Every day, in all aspects of life, materials are being worn down as a result of continual use. Friction is encountered everywhere; between car tires and asphalt; rubber shoe soles and cement sidewalks; and shovel teeth and abrasive earth material. Wear is a very complicated process that involves many factors and parameters making it difficult to quantify.

There are several different types of wear; dominant wear types include abrasive, adhesive, corrosive and erosive wear. Abrasion is particularly dominant in the Athabasca oil sands operations located in Northern Alberta. Abrasion can occur via a variety of modes, and the severity of the wear mechanism governs how a material body is worn down. Llewellyn (1996) reviews the considerable annual costs associated with wear; maintenance, replacement parts, and loss in production due to downtime all contribute to the ever increasing wear budget. The economic implications alone are substantial enough to continually aim at improving laboratory wear test practices. New or improved lab wear tests that produce results which increase industry’s certainty and confidence in predicting field wear would be undeniably beneficial. This thesis will focus on more accurately representing abrasive wear conditions experienced by shovel teeth as they excavate oil sand material. To accomplish this, a standardized wear test (ASTM G65) will be modified to more accurately reflect real-world digging conditions.

Implementation of a linear actuator will facilitate the variation of normal forces on a test coupon in an apparatus similar to the standard ASTM G65 setup. Raw data will be analyzed, scaled down and a typical dig cycle will be recreated from the raw data and simulated in the lab. The actuator provides the means to more accurately reflect the real-world load patterns experienced by the ultra-class electric shovels operating in the oil sands. The coupons that are tested will be hard-faced with chromium carbide, a practice used in the oil sands industry to resist wear attack on shovel teeth. An ammeter and voltmeter are connected to the wheel motor of the modified apparatus to measure the power draw during abrasion. The abrasive material used in the modified test will be bitumen stripped oil sand rather than the rounded quartz grain sand described in the standard G65 test. The oil sand provided is post hydro-transport, but still retains significant abrasivity qualities.

There are many challenges associated with trying to accurately represent real-world conditions in a laboratory setting. Naturally, all laboratory tests come with limitations. Wear tests are far from universal, and modifying a standard test to more accurately reflect real world conditions narrows the scope to an even more specific level. This test will reflect conditions only present in the Athabasca oil sands region. The forces that are scaled down represent just over six minutes' worth of data collected from one shovel operating at an unknown location in an oil sands mine. Forces experienced by the shovel can change from pit to pit depending on material diggability. The season and weather also influence the data, as colder temperatures could lead to a more consolidated face and thus increased forces required to excavate. Nonetheless, this thesis will attempt to show that a modified G65 test can lead to accurate, efficient wear prediction methods and that the existing standard wear test can be improved to more realistically reflect practical wear conditions.

1.1 Outline and Objectives

The thesis will start with an overview of the abrasive environment, modes and mechanisms of wear, tactics used to improve wear resistance, laboratory wear tests, and a breakdown of cable shovel geometry. Resolving the hoist and crowd forces to forces experienced at the teeth will outline how the raw data was analyzed, and the modified test method and procedure will be discussed. Results and analysis will assess the effectiveness of the test modifications, and a section on conclusions and recommendations will be provided.

The following specific objectives in modifying the ASTM G65 test will be targeted:

- Implementation of a linear actuator to vary the force in a manner more realistic to a shovel digging through a face. Current standardized wear tests often utilize a constant load over a specified time. This is not indicative of a mining operation. The incorporation of an actuator and stepper motor will allow the force to be varied in a way that mimics a shovel dig cycle.
- An evaluation of the abrasion resistance of a chromium carbide (Cr_7C_3) weld overlay with the abrasive media being bitumen stripped oil sands. The current ASTM G65 standard uses rounded quartz grain sand which can be better adapted to represent mining settings. The Cr_7C_3 weld overlay is a surface engineering technique often employed to reduce material wear rates. Volume loss using both bitumen-stripped oil sand and silica sand will be recorded and compared.
- A previous field tooth-life prediction technique will be employed using a slightly different approach and data obtained through the lab experiments to attempt to predict tooth-life in real-world circumstances. Comparisons will be made to two teeth that have experienced different periods of wear at an oil sands operation.

Ultimately, it is expected that the utilization of an actuator will significantly improve the standard G65 abrasion test by creating the ability to apply a cyclical set of force data to the wear test. Specific energy will also be evaluated for its capacity to predict field wear of shovel teeth, particularly in the unique digging of the Athabasca oil sands by using stripped oil sand as the abrasive.

2 LITERATURE REVIEW

2.1 Alberta's Oil Sands

Alberta's oil sands host the largest ultimate potential of an oil resource in the world, estimated at 1.7 trillion barrels (Bott, 2011). Oil sand is comprised mainly of quartz sand surrounded by a water film and covered in heavy oil called bitumen. The bulk of the Albertan resources are located in three main deposits: Athabasca, Cold Lake, and Peace River. From this ultimate potential, nearly 170 billion barrels are proven reserves with twenty percent of these reserves recoverable through surface mining processes. Approximately 26 billion barrels are currently under development using surface mining and in-situ techniques (Bott, 2011). This thesis will focus primarily on the Athabasca deposit, as it is the largest and currently has surface mining operations.

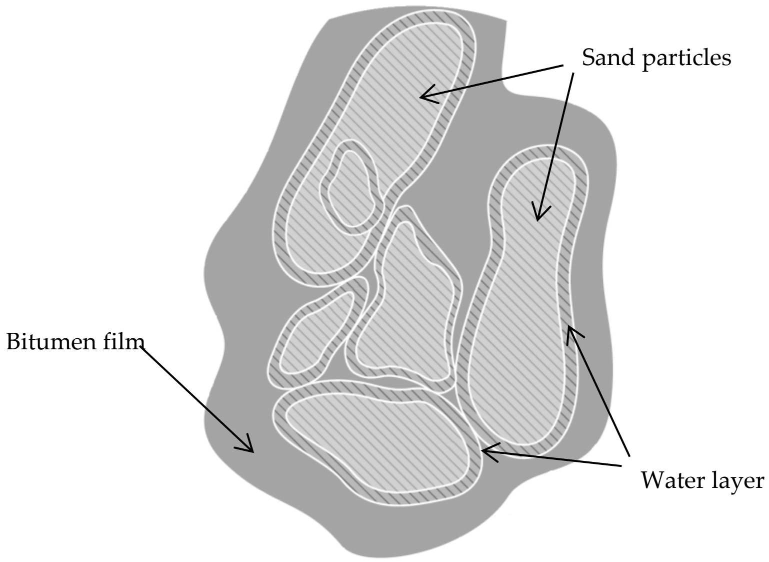

Figure 2.1 - The hydrophilic tendency of oil sand is crucial for extraction (After Bott, 2011)

The physical characteristics of Alberta's oil sands vary significantly from conventional crude oil. The bitumen in the oil sands is much heavier than conventional oil, with an API (American Petroleum Institute) gravity of 8 to 10 compared to 25 to 40 for most conventional crudes (Mossop, 1980). Oil with an API gravity that is 10 or lower will sink in water, which is why most conventional oils float but bitumen oil does not. Bitumen oil is also highly viscous and will not readily flow in its natural state; it will only ooze from the mine face on the hottest summer days. Similarities between oil sands and conventional reserves include: the degree of oil saturation is dependent on porosity, the oil is contained within the pore spaces, porous sand bodies control the distribution of rich and lean zones, and geological analyses can apply to both oil types (Mossop, 1980).

Intact oil sand displays an unusually high strength that can result in very steep natural and man-made slopes. The natural slopes can range from 50° to 55° with man-made highwalls reaching as high as 75°; as such, it is realistic to use a friction angle of 50° to describe undisturbed oil sands (Dusseault & Morgenstern, 1978; Joseph & Shi, 2012).

Table 2.1 – Select properties of oil sands (Adapted from Dusseault & Morgenstern, 1978)

Physical Property	Typical Values
In situ bulk density	2.11 ± 0.06 t/m^3, coarse-grained sands 2.21 ± 0.06 t/m^3, fine-grained sands 2.32 ± 0.06 t/m^3, sand & clayey silts
Mineralogy	90-98% Quartz 1-5% feldspar 0-3% muscovite 0-4% clay minerals
Approximate Bitumen Content	0-1% clay shales & clayey silts 0-10% sandy silts & silty sands 8-16% fine-medium grained sands 12-16% coarse-grained sands

The diggability of the oil sands is directly related to the geology of the formation and geotechnical parameters such as shear strength, density, bitumen content, viscosity and particle size to name a few. Consolidated faces or ground freezing from extreme cold can also influence a shovel's ability to excavate material (Patnayak & Tannant, 2005). Lower temperatures in winter result in higher bitumen viscosity.

2.1.1 Lithology of the Oil Sands

Lithology is a term that describes the unique characteristics of a rock of interest from the surrounding rock. Changes in lithology can be recognized by variations in colour, grain size, bedding, weathering resistance and many other factors (Carrigy, 1966). Grain size in particular plays a key role in determining the oil distribution in the reservoir. High-grade oil sands are predominately fine-grained oil sands, ranging from approximately 60 to 250 microns (Mossop, 1980). Much of the Athabasca deposit can be classified as well sorted. The absence of significant matrix fines is a primary reason for the reservoir's excellent quality (Mossop, 1980).

Figure 2.2 below demonstrates the lack of matrix particles. The white particles are quartz, and are sub-angular to angular in shape. The black background substance is bitumen.

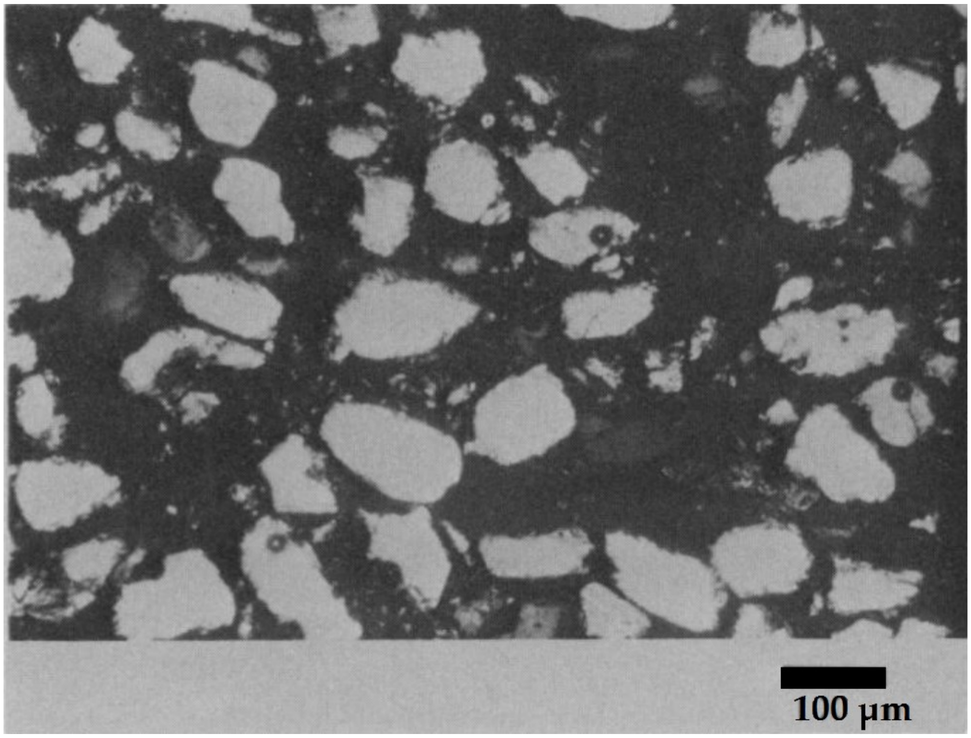

Figure 2.2 - Uniform quartz grains (white) and bitumen-filled pore spaces (black) (Adapted from Mossop, 1980)

2.1.2 Abrasivity of Oil Sands

Oil sand is extremely abrasive. The sand is composed of up to 95% quartz with the remaining 5% being feldspar grains, mica flakes and clay minerals (Mossop, 1980). Present are also traces of other minerals such as zircon, titanium, nickel, and iron. Oil sand is generally quite angular, contributing to the abrasivity. Quartz has been measured to have a Vickers Hardness (H_V) rating of 850 to 900, meaning that even the hardest steels only provide moderate protection. This is a concern, as quartz is the predominant abrasive encountered in oil sand operations (Llewellyn, 1996). Comparing wear rates of different ores in the field, it is typically found that higher silica content will result in higher wear rates (Tylczak *et al.*, 1999).

2.2 Wear in the Surface Mining Industry

Ground engaging tools (GETs) are constantly interacting with ore deposits and waste materials in mining operations. As a result, all equipment associated with the excavation and transportation of ground material is subject to wear attack. The impact of wear in the mining industry is undeniably significant. It has been considered a conservative estimate that over $1 billion in costs annually can be attributed to wear damage and friction in the Canadian mining and mineral processing industry. These costs stem from replacement of equipment parts to losses in production due to downtime (Llewellyn, 1996).

In most instances, several forms of wear act in collaboration to inflict damage on earthmoving equipment. Wear types that are present in the mining industry include, but are not limited to, abrasion, adhesion, erosion, corrosion and rolling contact wear. Abrasive wear is considered to be the most dominant wear type in the mining industry and is the wear type the experiments performed in this thesis will focus on.

2.2.1 Adhesion

Adhesive wear occurs when two surfaces slide against each other, without the presence of an abrasive medium, and the pressure between the two surfaces is large enough to cause plastic deformation (Eyre, 1978). As the surface asperities grow, they eventually break off resulting in material transfer from one surface to the other. As Eyre (1978) noted, the contact area is inversely proportional to hardness and therefore wear decreases with increasing asperity hardness. Due to the intense stresses, the two surfaces have the potential to be pressure welded, especially if they are chemically cleaned and mutually soluble.

2.2.2 Erosion

Erosive wear is similar to abrasion in the sense that hard particles slide against a wear surface. It is generally treated differently from abrasion due to the contact stresses arising from the kinetic energy of the abrasive particles encountering a surface (Eyre, 1978). Low impingement angles result in micro-scratching or cutting wear, indicating that hardness is the critical factor for the wear surface. At high impingement angles, deformation or micro-fracturing are the prevailing wear mechanisms creating a more complex wear solution (Eyre, 1978; Llewellyn, 1996).

2.2.3 Corrosion

Corrosive wear occurs when a sliding surface interacts chemically with the environment it is operating in. If a naked surface (such as a metal) is exposed to an environment that it can react chemically in, there is an initial rapid reaction which then slows over time (Rabinowicz, 1965). For some combinations of environment and material, the reaction ceases due to a film forming on the surface separating the metal surface and corrosive substance. However, this reaction product film can be worn away due to the sliding action that takes place. This can lead to continued corrosive attack (Rabinowicz, 1965).

2.2.4 Abrasive Wear

Abrasion is the most common wear type in the mining industry, and is most simply described as the removal of material from a surface by an abrasive medium. The severity of the wear attack relies on a number of factors, most broadly stated as the properties of the wear material, the abrasive properties, and the interaction between these two materials (Hawk & Wilson, 2001).

2.2.4.1 Abrasive Wear Modes

Accurately defining the mode of abrasive wear depends on the individuals' own interpretation of the wear result and the application of many existing, and varying, definitions of abrasive wear. Several recognized authors and reputable publications describe abrasive wear with similar terms but contradictory meanings, depending on the individual classifying the mode of abrasion. Phrases such as two-body and three-body abrasive wear attempt to provide a general description of common wear modes, yet there are discrepancies within industry that lead to confusion. No universally recognized definitions of the terms exist as there are several different interpretations.

The dominant interpretation is to evaluate if the abrasive particles are constrained (two-body) or free to roll (three-body). This definition generally results in two-body wear being much more severe (Gates, 1998). Alternatively, the second major interpretation emphasizes the presence (three-body) or absence (two-body) of a rigid counter-face backing the abrasive. This view results in three-body (high-stress) abrasive wear being more severe than two-body (low-stress) abrasive wear, a result completely opposite from the first interpretation (Gates, 1998).

Rock crushing is an example of a situation that results in confusion from the two-body or three-body classification. Gates (1998) notes that some authors believe it is a three-body, or loose abrasive, condition as the two jaw plates and free flowing rock material create the three-body system needed. However, the large rocks and gripping force from the crusher can create abrasion grooves implying that the abrasive material is being rigidly held. It is this grinding action that leads some authors to equate three-body abrasion with high-stress abrasion and two-body with low-stress (Gates, 1998).

An alternative classification scheme is presented by Llewellyn (1996) and Hawk & Wilson (2001). This scheme is more straightforward and is how abrasive wear modes will be described in this thesis. The terminology is broken down in to three different wear modes summarized below:

- **Low Stress Abrasion –** Low contact force between abrasive and material surface. The abrasive remains mainly intact and the material is worn through a micro-cutting action. This wear type can occur as ore slides down a hopper or as shovel teeth dig through soft ore.
- **High Stress Abrasion –** The abrasive particles are trapped between two hard surfaces in moving contact. Material is removed due to scratching, ploughing and fracture. Often seen in equipment undercarriages or grinding mills.
- **Gouging –** Abrasive interacts with wear surface with sufficient force to plow out material via plastic flow. Typically seen in primary crushers and grinders (Hawk & Wilson, 2001).

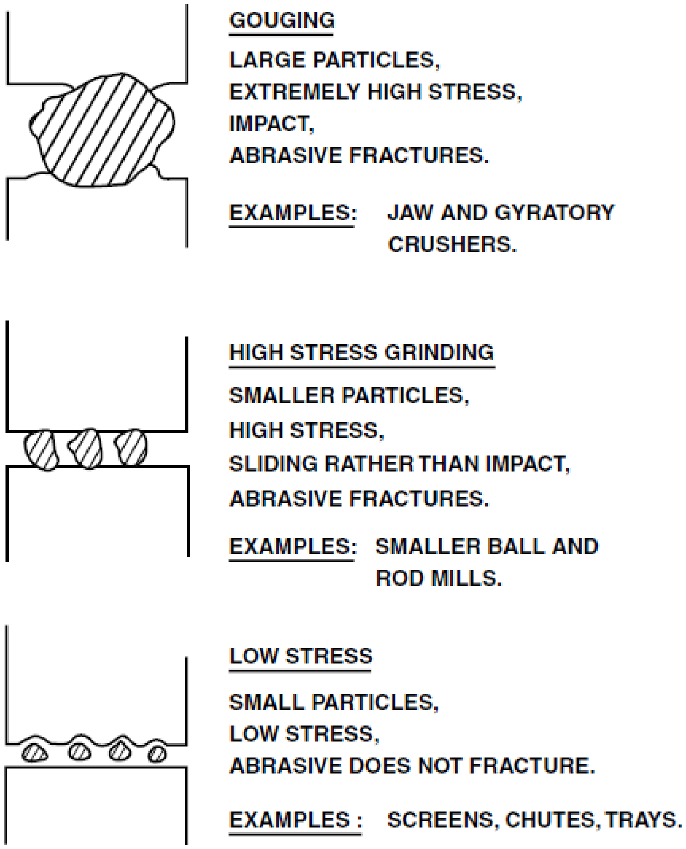

Figure 2.3 - Illustrative example of some wear types encountered in mining (Adapted from Hawk & Wilson, 2001)

Typically, an excavator operating in an oil sands environment experiences low stress abrasion as oil sand is not subjected to blasting and the abrasive particles do not fracture during excavation. It is possible for a ground engaging tool (GET) operating in the oil sands environment to experience high stress abrasion if the deposit face is particularly consolidated. Depending on the operating conditions and bucket/tip design, the GET may experience high impact wear from repeated blows against the face (Joseph, 2013). With proper technique and sufficient operator skill this type of wear can be minimized in the excavation process. This thesis and the experiments within will focus on a low stress abrasion scenario.

2.2.4.2 Abrasive Wear Mechanisms

A number of factors influence the severity of a wear attack. The mechanical properties of both the abrasive and wear material are the most crucial in determining the wear behaviour. The interaction of these mechanical properties is also vital to consider (Hawk & Wilson, 2001). Table 2.2 below summarizes the most important factors to consider.

Table 2.2 - Factors contributing to wear attack severity (Adapted from Hawk & Wilson, 2001)

Abrasive Properties	Contact Conditions	Wear Material Properties
Particle Size	Force/Impact level	Hardness
Particle Shape	Velocity	Yield strength
Hardness	Impingement angle	Elastic modulus
Yield Strength	Sliding or rolling	Ductility
Fracture properties	Temperature	Toughness

A more in-depth investigation of the contact conditions allows for a study of the wear mechanism by which material is removed. Hawk & Wilson (2001) summarized wear mechanisms that can occur, depending on abrasive and material properties, as shown in Figure 2.4 below:

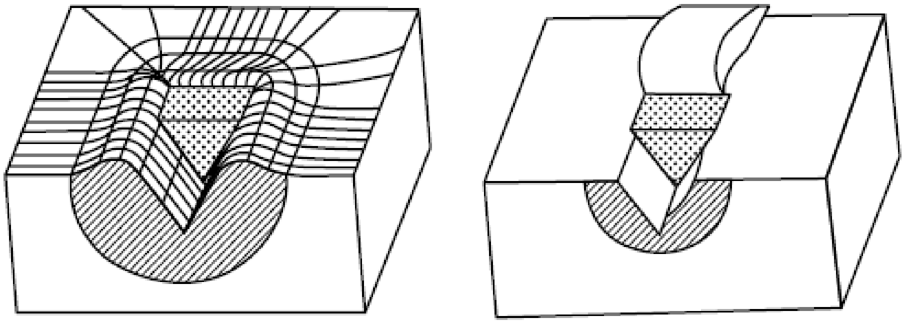

Microploughing

Microcutting

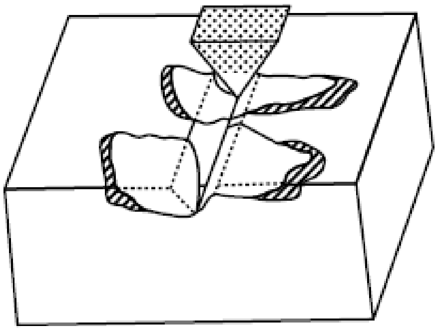

Microcracking

Figure 2.4 - Wear mechanisms on the microscopic scale (After Hawk & Wilson, 2001)

The abrasive and wear material properties determine which wear mechanism will occur. The different wear mechanisms are summarized below (Zum Gahr, 1988; Hawk & Wilson, 2001):

- **Ploughing –** Grooves are formed as material is displaced to the side. Generally, no material is displaced in a single pass, as the mechanism involves plastic flow. Material can be removed if there is an excess of abrasive particles passing over the ridges that were created by the ploughing action.

- **Cutting –** The wear material is separated as a primary chunk of debris in a much cleaner, crisper fashion. The volume lost is equal to the volume of the wear grooves, supporting why this mechanism resembles conventional machining.
- **Cracking –** The cutting process and high stresses imposed by the abrasive particles causes fracture. These localized fracture zones then cause crack formation and propagation resulting in additional removal of wear debris via spalling.

As the ploughing and cutting mechanisms primarily involve plastic deformation, they are primarily associated with ductile material. The cracking or fragmenting mechanism is then associated with brittle materials.

2.3 Advances in Abrasive Wear Resistant Materials and Surfacing Techniques

Wear resistance comes in many different forms. A variety of components and protection systems for overcoming wear are available to the mining industry. Generally, they are classified into four primary groups: ferrous-based materials, surface engineering techniques, elastomers/polymers, and ceramics/cermets (Llewellyn, 1996).

2.3.1 Ferrous-based resistant materials

Iron and steels are the most extensively used group, varying in carbon content from low-carbon steels to cast iron with alloy contents greater than 30 %. A main advantage is the comparatively low cost combined with greater availability due to standard manufacturing and processing methods (Llewellyn, 1996). The most pertinent ferrous wear materials can be categorized by pearlitic and martensitic steels; austenitic manganese steels; and abrasion resistant white irons.

Table 2.3 – Characteristics & applications of ferrous-based materials (After Llewellyn, 1996)

Composition	Characteristics	Industry Applications
Pearlitic Steels	250 – 550 HB Hardness Good impact/abrasion resistance	Cone/gyratory crusher segments
Martensitic Steels	230 – 530 HB Hardness Variety of strength, toughness, weldability. Hardfacing can also be applied.	Bucket lips & corners, ripper teeth, hopper/chute liners, sheaves/pulleys
Austenitic Mn Steels	Very tough. 200 HB but can work-harden to > 500 HB under impact or high stress loading. Low strength and weldability.	Jaws, concaves in crushers. Shovel dippers, rigging parts
White Irons	High sliding abrasion/erosion resistance. 10 to 40 % carbide constituents. Excess of 550 HB	Slurry pumps and pipe components. Chute/hopper liners

2.3.2 Surface Engineering Techniques

Bulk materials can be used to provide the necessary protection but will be very costly and not particularly efficient. Alternatively, performance and economics of wear resistance can be improved by the application of a wear coating to the wear surface. This allows for the base material to be chosen for its structural properties, reduced cost, and ease of manufacturing (Smart & Moore, 1979). It is well known that the presence of carbides has a positive influence on wear behaviour. The presence of these hard phases and their composition, amount, and morphology all affect the level of improvement. A coarse carbide distribution under conditions of pure abrasion is best, whereas finer well-distributed carbides are preferred if there is some degree of impact involved (Smart & Moore, 1979). There are a variety of methods to apply surface coatings including electrodeposition, chemical coating, spraying, welding, and many others. This thesis will focus primarily on weld overlays, as all test coupons were prepared in this manner.

2.3.2.1 Weld Overlays

Weld deposition hardfacing is the most common surface engineering technique used in surface mining (Llewellyn, 1996). It allows for the bulk base materials to still be used, helping to reduce cost. Hardfacing can also be very selective in its application and the worn components can be replaced more easily. Additionally, the materials that can be deposited are exceptionally wear resistant, with chromium carbide and tungsten carbide providing extreme abrasion resistance.

Welded overlays can be applied via a variety of processes such as Rod and Powder Brazing, Flux-Cored Arc Welding, Plasma Transferred Arc Welding (PTAW), and Shielded Metal Arc Welding (Harper *et al.,* 2002). PTAW-applied tungsten carbide overlays have shown excellent wear resistance combined with consistent quality and reasonable cost (Anderson *et al.,* 2003). Submerged Arc Welding (SAW) is another method used in hardfacing applications, and is the process by which the coupons tested in this thesis were created.

2.3.3 Elastomers and polymers

The role that elastomers and polymers play in wear protection in the mining industry is primarily in conveyor belts and off-road tires. These materials are very resilient and have high toughness, corrosion resistance, and are generally more easily fabricated (Llewellyn, 1996). Weaknesses come in the form of tear and gouging resistance, and these materials cannot be used as slurry linings if particles sizes exceed 64 mm. Other applications include truck box linings, pump linings, idler covers, and shovel bumpers (Llewellyn, 1996).

2.3.4 Ceramics and Cermets

Ceramics are characterized by high hardness and excellent abrasion resistance, but their brittle qualities limit their use in surface mining. Ceramics main applications are used in conjunction with rubber and polyurethanes (Llewellyn, 1996).

Cermets are a combination of a metal with one or more ceramic phase which makes up most of the material. Industrial applications include cemented tungsten carbides. These carbides exhibit very high abrasion resistance and hardness, as well as toughness qualities (Llewellyn, 1996).

2.4 Current Abrasion Tests and Wear Modelling Capabilities

Accurate prediction of material wear rates and patterns is very important to any industrial manufacturer that deals with excavation, transportation, or processing of material. Abrasive testing is a crucial aspect in determining the wear performance of a material and can also create laboratory standards that can reduce the costs of testing in the future (Hawk, 2000). Computer modelling techniques allow for improvements in product design as well as the development of more suitable testing methods. Improvements in computer processing have allowed for many aspects of wear to be studied simultaneously, resulting in the ability to identify the most important wear factors (Zum Gahr, 1988). Several abrasion tests and modelling techniques will be discussed below. This thesis will focus primarily on a modified version of the ASTM G65 Dry Sand Rubber Wheel Test (DSRW) as it is most applicable to a shovel digging in oil sand material.

2.4.1 Industry Recognized Standardized Abrasive Tests

The goal of any laboratory test is to simulate real-world conditions as closely as possible. Ideally, the test performed is exactly what occurs in the field; however cost, scale, and practicality almost always prevent this. For laboratory wear tests, the goal is to produce a wear mode that is as similar as possible to the real world application, and that the wear mechanism observed in the field is the primary mechanism in the laboratory test. Other important factors to consider include the acceleration (reduced cost and time of the test compared to real world practice), specimen preparation, a test control, wear measurement, and data reporting (Hawk, 2000). Table 2.4 below highlights some standardized abrasion testing procedures:

Table 2.4 - Abrasion and Erosion Test Procedures (Adapted from Hawk, 2000)

ASTM Standard No.	Test Description
G56	Abrasiveness of Ink-Impregnated Fabric Printer Ribbons
G65	Measuring Abrasion Using the Dry Sand Rubber Wheel Apparatus
G75	Slurry Abrasivity and Slurry Abrasion Response of Materials
G76	Conducting Erosion Tests by Solid Particle Impingement Using gas Jets
G81	Jaw Crusher Gouging Abrasion Test
G105	Conducting Wet Sand Rubber Wheel Abrasion Tests
G132	Pin Abrasion Testing

Not all of the above abrasive tests are pertinent to this thesis topic, and therefore will not all be described in detail. Important industry wear performance tests that will be discussed include ASTM G65, G81, G105 as well as some industry modified non-standardized wear tests.

2.4.1.1 ASTM G65 Dry Sand Rubber Wheel Test

The ASTM G65 Dry Sand Rubber Wheel (DSRW) test is used to measure the resistance of chosen materials to scratching abrasion under a specific set of conditions. The test results are generally reported as a volume loss, in the form of mm^3. In this test, the abrasive particles are not fixed. The particles are free to slide and rotate simulating low-stress three-body abrasive wear (Hawk, 2000). Figure 2.5 below shows a general schematic of a standard G65 apparatus.

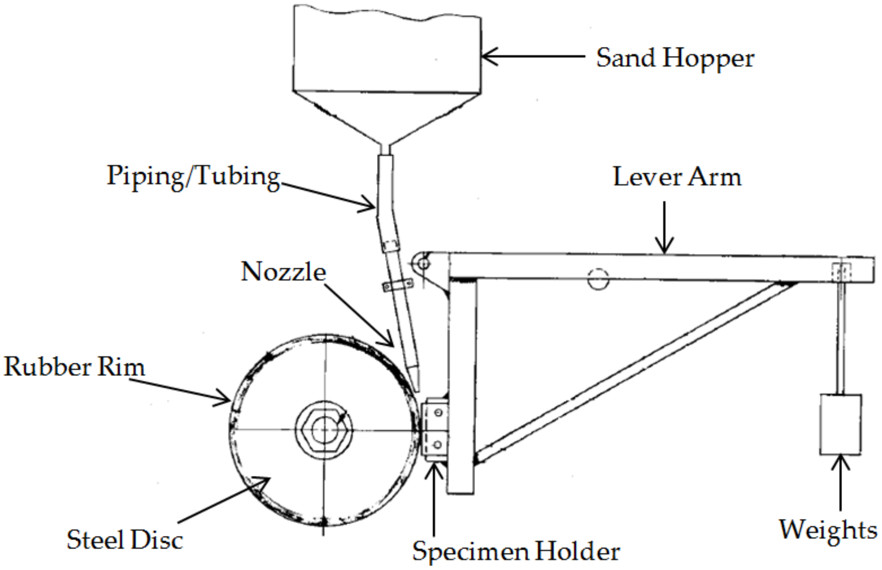

Figure 2.5 - Basic setup of DSRW testing apparatus (Adapted from ASTM G65)

It is important to note that the DSRW test is intended only to rank various materials, and not for determining absolute wear values. Hawk (2000) states that one material that wears half as much as another may not last twice as long in the field. This is because the test tends to exaggerate differences in the materials. The hardness and particle size of the abrasive media will affect the absolute values of wear more than they affect the ranking.

Within the G65 test, there are five different procedures that can be performed depending on the thickness of the test material and its wear resistance. Table 2.5 outlines the different test procedures and the specifications of each.

Table 2.5 - Standard DSRW Abrasion Test Parameters (After Hawk, 2000)

Procedure	Normal Force on Specimen (N)	# of Wheel Revolutions	Total distance abraded (m)	Procedure Description
A	130	6000	4309	Very severe. Can rank low to high resistance
B	130	2000	1436	Short term version of A. Use when material ΔV > 100 mm^3 in A
C	130	100	71.8	Short term version of A for thin coatings
D	45	6000	4309	Similar to A for low abrasion resistance materials
E	130	1000	71.8	Short term version of B for low to medium resistance

2.4.1.1.1 Apparatus and Abrasive Material Specifications

In a standard dry sand/rubber wheel abrasion test, an abrasive grit of controlled size and composition is aligned to flow between a test coupon and the rotating rubber wheel. A load is introduced to act normally against the wheel via a lever arm and weighted plates (ASTM G65, 1980(2010)). The rubber wheel is rotated such that it contacts the coupon face in the same direction as the grit flow. The amount of wheel revolutions and force applied varies depending on which of the above five procedures is chosen.

The rotating wheel used in the G65 test consists of a steel disk with a chlorobutyl rubber layer shaped around the outside circumference. The standard G65 test specifies that the optimum hardness of the rubber wheel is Durometer A-60, with a range from A58 to A62 being tolerable. It is recommended that four hardness readings be taken along the periphery of the wheel, preferably 90° apart, using a Shore durometer tester following test method D2240 (ASTM G65, 1980(2010)). It is also good practice to allow the rubber wheel to cool between tests, preventing a warmer, softer wheel from degrading in future runs.

The original G65 test incorporates a custom designed nozzle to ensure accurate sand flow distribution and rate. The optimum positioning of the nozzle is as close to the wheel-coupon contact interface as possible. Generally, nozzle construction out of stainless steel is preferred due to its workability and ease of welding. The G65 test dictates an abrasive flow rate of 300-400g/min with the sand being rounded quartz grain sand that is notably dry (ASTM G65, 1980(2010)).

The G65 test specifies that the moisture content cannot exceed 0.5 weight percent, as wet abrasive can clog the nozzle and affect test results. The abrasive size is controlled using U.S. sieves where a maximum of 5% is retained on U.S. sieve size 50 and a minimum of 95% is retained on sieve size 70.

2.4.1.1.2 Specimen Characteristics and Preparation

The G65 test was designed such that material of any types could be investigated; including castings, gas or electric weld overlays, plasma spray deposits, cermets, ceramics and many others. The test coupon is normally rectangular in shape, with dimensions of 25 x 76 x 8 mm. It is noted that the thickness can range between 3.2 and 13 mm depending on the user's needs. The wear surface should be ground flat and the density of the material must be known.

When testing electric or gas weld deposits, the ASTM standard recommends double weld passes to prevent weld dilution of the base metal. It is also recommended that the coupon surface be at least 63.4 mm long and 19.1 mm wide in order to produce a suitable wear scar. It is important to be aware that many aspects of the weld and how it is applied can have significant effects on the abrasion resistance of the weld deposit (ASTM G65, 1980(2010)). The full procedure of how to prepare samples and perform the test is listed in the ASTM G65 document.

2.4.1.2 ASTM G81 Jaw Crusher Abrasion Test

The jaw crusher abrasion test is a test that gives high-stress, three-body abrasive wear. The standardized jaw crusher test involves two test plates and two reference plates. One test plate and one reference plate are attached to the stationary jaw, and the remaining two plates are attached to the movable jaw. The plates are arranged such that a test plate and reference plate are opposite one another (Hawk, 2000). Once the test is complete, a mass loss is recorded and a volume loss calculated by dividing by the material density. A wear ratio is then obtained by dividing the volume loss of the test plate by the volume loss of the reference plate. Note that this is done separately for the stationary and movable plates (ASTM G81, 1997(2013)). A final wear ratio is obtained by averaging the stationary and movable ratios.

2.4.1.2.1 Apparatus and Abrasive Material Specifications

The apparatus should be designed to accept two identical plates on the stationary jaw and two identical plates on the movable jaw. As specified above, the plates will have one test material and one reference material on each plate. The feed opening is approximately 100 x 150 mm and the minimum jaw opening is set to 3.2 mm.

The ASTM G81 test involves a substantial amount of material; a minimum of 225 kg per test run is required. Runs are completed until a minimum of 900 kg of material is crushed. For this reason, alternate procedures have been investigated so that the test may be performed on a smaller scale. The abrasive used can be matched to the field applications; material such as limestone, granite, and quartz sand are all common (Hawk, 2000).

2.4.1.2.2 Specimen Characteristics and Preparation

The G81 standard calls for reference plates that are as close to possible to 269 HB hardness. It is recommended that a large plate is purchased and plates machined to the appropriate size (ASTM G81, 1997(2013)). The test plates shown in the ASTM standard have dimensions of 230 x 83 x 19 mm.

One non-standard alteration to the G81 test is to supplement the reference plates with plates of another test material. The rock is crushed as per ASTM standard and once the samples are cleaned and weighed they are reversed in the jaw assembly (i.e. switched from stationary to movable), yet still keeping two different test materials opposite of each other (Hawk, 2000). The test is then run again and an average mass loss is calculated for each of the two plates of the same material. Volume loss is again calculated from the density, and data from two test specimens is obtained as compared to one in the standardized test.

One advantage of the standardized test is the ability to check if the performance of the jaw crusher is still within specifications. The non-standard test allows for two materials of similar hardness to be tested simultaneously. It also eliminates the possibility of a weaker material wearing at an accelerated rate which can skew the ratio in respect to the reference material (Hawk, 2000).

Many researchers believe that the G81 test most closely represents wear experienced by ground engaging tools such as excavator teeth, shovel buckets, graders, as well as real jaw crusher wear (Hawk *et al.*, 1999). However, the purpose of the jaw crusher test is to evaluate gouging abrasion. This is not the abrasion mode of interest in this thesis. For this reason the jaw crusher abrasion test will not be investigated any further in this thesis.

2.4.1.3 ASTM G105 Wet Sand Rubber Wheel Test

The Wet Sand Rubber Wheel (WSRW) Test is very similar in principle to the G65 test. As the title implies, the main difference is that the abrasive grit particles are suspended in a slurry and are introduced to the specimen by a partially submerged rotating wheel (ASTM G105, 2002(2007)). Contrary to the G65 test, where the abrasive is gravity-fed, the slurry in the G105 test is agitated by paddles attached to the spinning rubber wheel (Hawk, 2000). The motion of the paddles causes the abrasive to be carried upward across the wear specimen. Similar to the G65 test, wear losses are reported in mm^3 and the normal force is applied using a lever arm and appropriate weights. Unlike the G65 test, which has five possible procedures, the G105 test has only one that is a recognized standard.

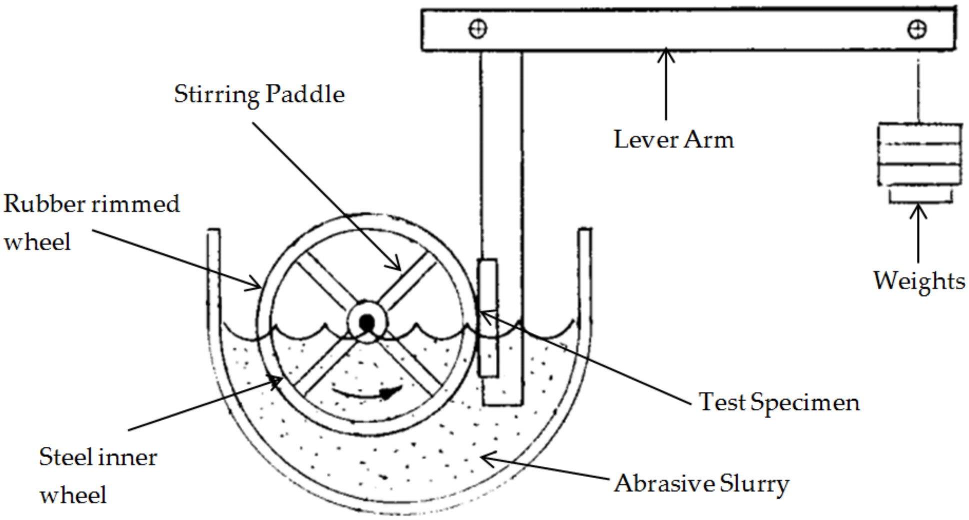

Figure 2.6 - Schematic of the WSRW Test (Modified from Hawk, 2000)

The above diagram is a schematic of the test setup for the WSRW abrasion test. The wheel in this diagram rotates in a counter-clockwise direction.

Table 2.6 - Procedure outlining the standard WSRW Test

Procedure	Normal Force on Specimen (N)	# of Wheel Revolutions	Total Distance Abraded (m)	Procedure Description
A	222	1000*	558.6	Can rank low to high resistance

*The test is initially run with 1000 revolutions to expose fresh material not affected by surface preparation. Tests afterwards are run at 1000 revolutions or until a designated count is reached.

2.4.1.3.1 Apparatus and Abrasive Material Specifications

The G105 test utilizes three rubber wheels with Shore A Durometer hardness' of 50, 60, and 70. It is once again recommended that the hardness ratings be taken at points 90° apart, with a tolerance of ± 2 being acceptable (Hawk, 2000). The reason behind using three wheels of varying hardness is to normalize the mass loss for each wheel. The logarithms of mass loss are plotted as a function of the wheel hardness. By fitting a least squares line to the three data points a test value for mass loss is determined using Durometer 60 (Hawk, 2000; ASTM G105, 2002(2007)). The volume loss is then calculated using the density of the material.

The slurry mixture is composed of 0.94 kg of deionized water and 1.50 kg of rounded quartz grain sand. The abrasive used is the same as the ASTM G65 test. Other abrasive-slurry mixtures can be incorporated; however these tests are not standardized.

2.4.1.3.2 Specimen Characteristics and Preparation

The specimen in the WSRW Test is a different shape than in the DSRW Test, with dimensions of 25 x 57 x 16 mm. The density of the material is required to calculate the volume loss, reported in mm^3. Before the actual wear test begins, the test specimen is placed in the holder, loaded with 222 N of normal force and run for 1000 revolutions in order to expose fresh material not affected by surface preparation. The specimen is removed, cleaned, weighed and is ready to begin the wear testing (Hawk, 2000).

As with the G65 test, double weld passes are recommended and specimens may also be machined right to size directly from raw material. Coatings are acceptable, as long as the abrasive does not penetrate through to the substrate material. The full procedure of how to prepare samples and perform the test is listed in the ASTM G105 document.

2.4.1.4 Other Wear Tests

Many other wear tests exist for a variety of wear types including adhesion, impact abrasion, corrosion and erosion. Bond (1964) developed a laboratory scale impact abrasion wear test to simulate the wear conditions on impact hammers and blow bars during the ore crushing process. This process led to the definition of Bond Energy. The impeller and abrasive particles sit inside a larger, slowly rotating drum. The impeller and drum rotate in the same direction, and the slow (45 rpm) rotation of the drum allows for abrasive particles to be lifted along the walls until gravity overcomes friction and the particles fall against the rapidly (620 rpm) rotating impeller paddles (Hawk, 2000).

Erosion testing can be performed by the standard ASTM G76 test method. This test is another example of an impact abrasion process. Typically with solid particle erosion, the particle size is small (in the range of tens to hundreds of microns) but the particle velocity is quite high, at ten to several hundred metres per second (Hawk, 2000). A number of other wear tests performed in industry and the laboratory exist but are beyond the scope of this thesis and therefore will not be discussed any further.

2.4.2 Abrasive Wear Modelling and Prediction Techniques

The ability to model and predict outcomes with inexpensive, reproducible tests is a valuable asset of laboratory testing. Modelling wear is difficult due to the complex conditions wear is experienced in. Fluctuating loads, velocities, material properties, contact geometry and the working environment are a few of the aspects that can affect the wear of materials. As previously discussed, abrasive wear can be classified as either two-body or three-body wear. Intuitively, two-body wear is easier to understand from a modelling perspective (Torrance, 2005).

There have been several attempts to determine accurate wear models. Not surprisingly, an accurate wear model depends on the specific conditions of the test. This has resulted in models representing isolated situations rather than a uniform abrasive wear model. Modelling factors such as material hardness, abrasive shape and attack angle, and degree of penetration can all influence the construction of a wear mode diagram. Modelling theories involving boundary slip line theory, finite element analysis, wear maps, microscale dynamic models, molecular dynamic simulations, and others have been created for particular wear situations. Below are some general descriptions of selected models of wear.

2.4.2.1 Cone Model

The shape of an abrasive will directly influence the wear rate. Different abrasive shapes will have different attack angles, and the geometry of the abrasive will affect the cross sectional area of the scratch it makes. Ploughing can take place during sliding where if the contact interface between two surfaces has interlocking of inclined or curved surfaces (Kato & Adachi, 2001). Wear patterns and volume will differ if the wearing material has ductile or brittle properties, as indicated by Figure 2.7 below:

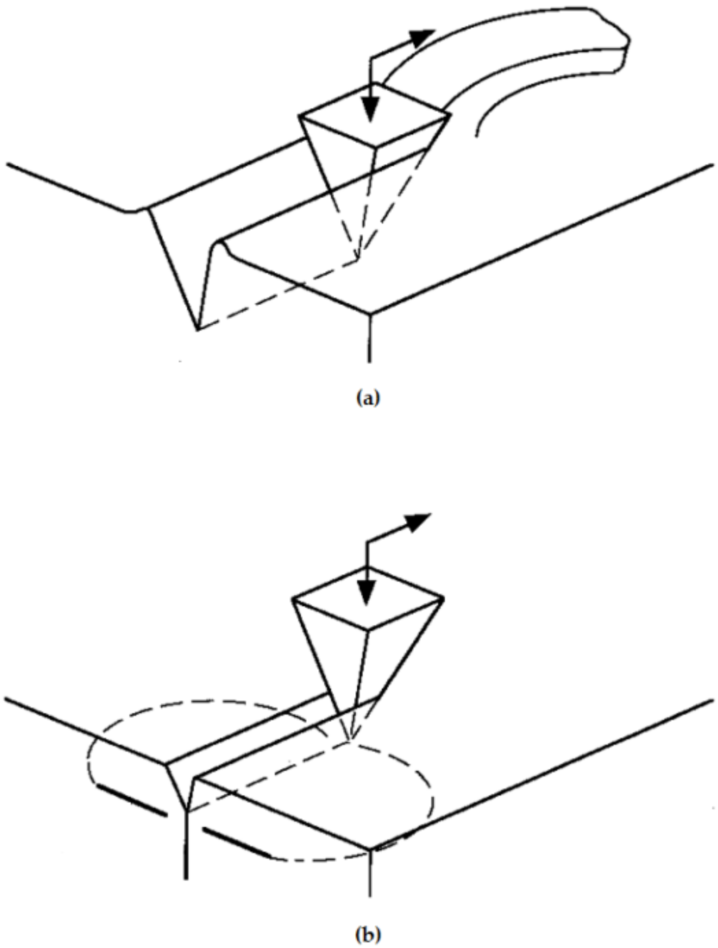

Figure 2.7 - Abrasive wear of ductile material (a) and of brittle material (b) (After Kato & Adachi, 2001)

A simple and straightforward method to modelling wear based on the wear particle geometry is to imagine an abrasive with a conical shape moving through the contact interface. Figure 2.8 outlines the typical model created when using this assumption.

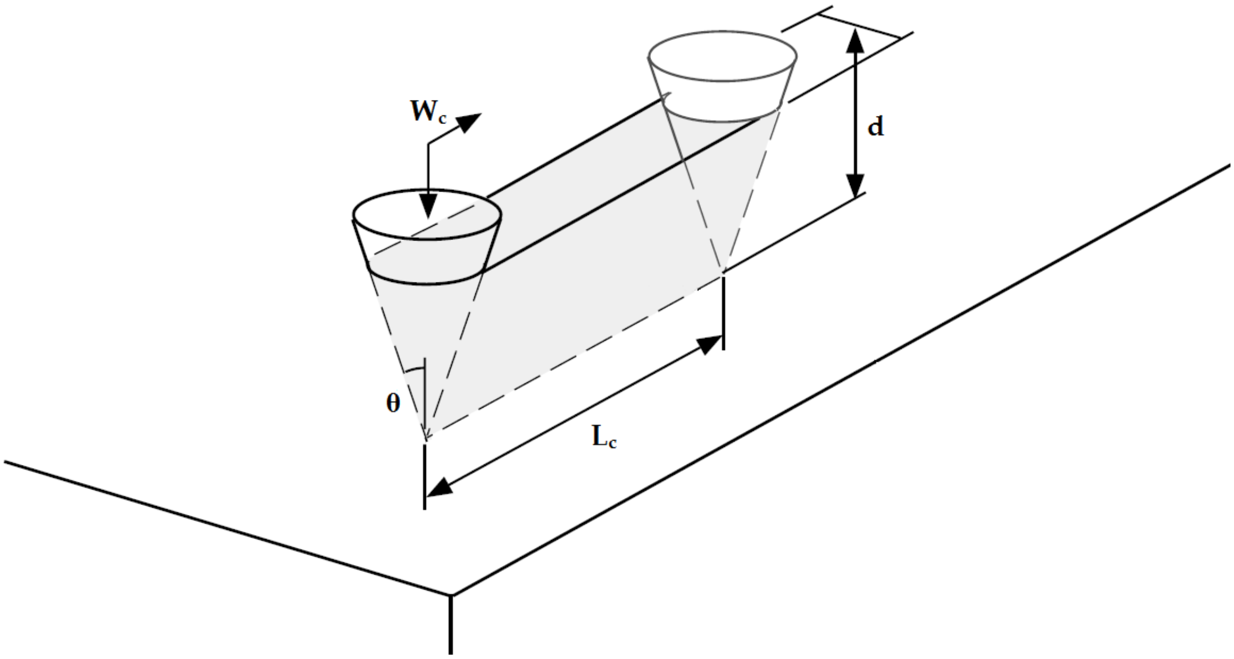

Figure 2.8 - Simple model of abrasive wear by a conical particle (Adapted from Kato & Adachi, 2001)

By assuming a conical wear particle the volume loss, which is dominated by plastic deformation, can be estimated using the following equations (Kato & Adachi, 2001). The wear volume in a ductile material, created by a ploughing action of the harder asperities over a distance of L_c, is given by:

$$V_c = d^2 * \tan\theta * L_c \tag{2-1}$$

When normal contact pressure under plastic content is assumed to be equal to the hardness value H_c of the material, the real contact area of the modified cone is expressed by:

$$\frac{W_c}{H_c} = \frac{\pi * (d * \tan\theta)^2}{2} \tag{2-2}$$

Combining Equations 2-1 & 2-2 yields the possible wear volume V_c (shaded region in Figure 2.8) under the applied load and total sliding distance:

$$V_c = \frac{2}{\pi * \tan\theta} * \frac{W_c * L_c}{H_c} \tag{2-3}$$

Kato & Adachi (2001) explain that Equation 2-3 gives the wear volume for the ideally plastic abrasive grooving in microcutting case, but also show that there are other scenarios of wedge forming where the wear volume does not always equal the groove volume. To accommodate all possibilities, a wear coefficient K_{ab} is introduced in place of the $\frac{2}{\pi * \tan\theta}$ term. This implies that the wear volume is directly proportional to the applied load and sliding distance, while being inversely proportional to the hardness of the wearing material (Kato & Adachi, 2001).

Kato & Adachi (2001) also outlined the formula for estimating wear volume in a brittle material, where the wear particles are generated mainly from brittle fractures caused by the propagation of cracks. Following a certain set of assumptions, the wear volume V_{bc} is given by:

$$V_{bc} = \alpha_3 * \frac{W_c^{\frac{9}{8}}}{K_c^{\frac{1}{2}} * H_c^{\frac{5}{8}}} * \left(\frac{E}{H_c}\right)^{\frac{4}{5}} * L_c \qquad \textbf{(2-4)}$$

Where α_3 is a material-dependant constant, K_c is fracture toughness, E is Young's Modulus, and W_c, H_c, and L_c are as before.

2.4.2.2 Microscale Dynamic Model

Many existing wear models are only appropriate for macroscopic situations. Inherently, this makes the models unsuitable for characterizing wear behaviour in finer detail such as the influence of microstructure on wear (Li *et al.*, 1999). One attempt to develop a more fundamental model is the molecular dynamic simulation technique; however this technique is impractical for realistic systems as it is limited severely by computing capabilities. The microscale dynamic model is an attempt to link the atomistic simulation of the molecular dynamic technique with current macro models.

The premise of the microscale dynamic model is to discretize a material system and represent it using a discrete lattice (not to be confused with crystal lattice). Each lattice site represents some volume of the wear material, and the wear process is simulated using Newton's equation of motion on each lattice site (Li *et al.*, 1999). For simplicity, this model is performed in two dimensions and the wear specimens are discretized using a square lattice. An example is shown in Figure 2.9 This simplification is also a drawback, as it considers the specimens to be homogenous. Additionally, computing time would increase significantly if the unit length of each lattice site was decreased.

The final position of each lattice site is influenced by the external force during a wear process and by the interaction of the lattice sites with one another. This internal lattice site interaction is dependent on the mechanical properties (such as elastic modulus, yield stress, tensile strength, ductility, and work-hardening) of the material (Li *et al.*, 1999).

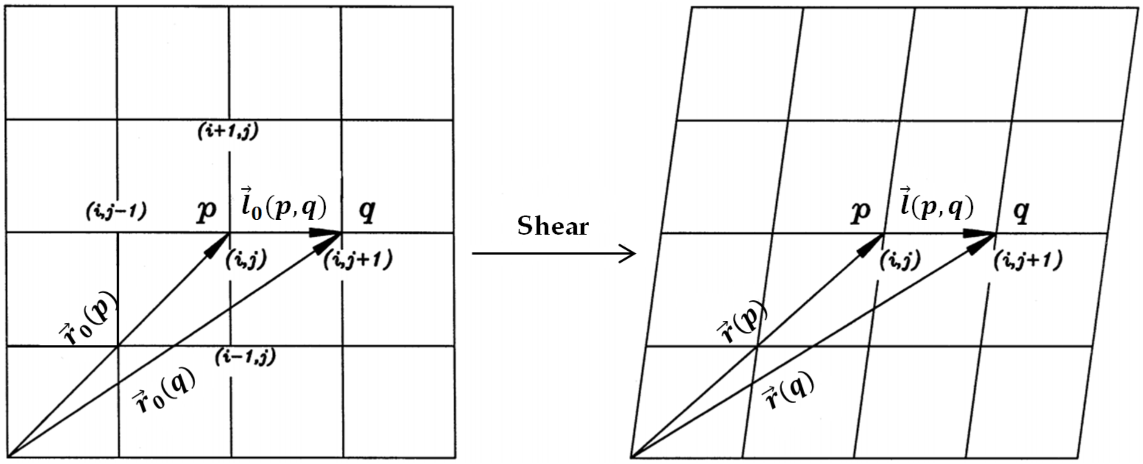

Figure 2.9 - Visual representation of vector translation in microscale dynamic model (After Li *et al.*, 1999)

2.4.2.3 Wear Maps

Wear maps are designed based on the recognition that there are many variables involved in modelling wear. The idea is that the independent variable is wear; the independent variables are divided into continuous variables and discrete variables. Continuous variables are entities such as speed, load, temperature, and time. Discrete variables are more general, and include dry, nonreactive or reactive lubricant, the environment, and contaminants (Hsu & Shen, 2001). The thought process is then to create three-dimensional maps of wear versus combinations of the continuous variables to describe the wear systematically.

Hsu & Shen (2001) note that a complete set of wear maps will often not be necessary; a selected set of maps will define the critical limits or boundaries for the materials pair in terms of acceptable wear behaviour. However, each discrete parameter will result in the material pair exhibiting wear transitions, tribochemical reactions, oxide formation, plastic deformation, and fracture. The conditions that these phenomena occur under will differ as the discrete parameter changes from one to another.

The variations of wear behaviour take place in experiments sometimes under controlled conditions and others accidentally. This leads to confusion in determining definitive wear behaviours, ultimately resulting in the conclusion that a single wear model will not be sufficient to predict wear behaviour of a material pair in general (Hsu & Shen, 2001).

2.5 A Brief Overview of Cable Shovels

Electric cable shovels have been an integral part of earth-moving operations for over 100 years. In open-pit mining, cable shovels represent the most extensively used high volume excavators (Shi & Joseph, 2005). This is due in large part to their high production capacity and low operating cost per tonne of material excavated. The combination of electric shovels and heavy haulers in the Athabasca oil sands is vital in maintaining high production rates over an extended period of time.

2.5.1 Operation and General Components of a Cable Shovel

2.5.1.1 Movements of Cable Shovels

A cable shovel will operate with four major movements: drive motion, hoist motion, crowd motion and swing motion. The drive motion controls the shovel's proximity to the face, as well as its ability to move to a different location. The swing movement is initiated as the shovel exits the face (full of ore or waste material) to load a waiting haul truck and after it has dumped the material allowing it to re-enter the face. Neither the drive nor swing movement are crucial to the objectives of this thesis and will not be investigated in detail any further.

The hoist motion is the upward movement of the dipper through the mining face and requires sufficient power and force to overcome the weight and frictional forces of the virgin ground. The crowd travel is the position of the dipper into the face of the bank. It retracts and extends along a rotating handle and serves to ensure that the shovel bucket is filled during each pass. It is the combination of the hoist and crowd actions, particularly the force generated from the hoist motion, which this paper will investigate to determine the resistive forces experienced by the shovel teeth.

2.5.1.2 Components

A cable shovel has an enormous number of components and parameters involved to effectively complete its tasks. A particular set of these will be isolated to identify the magnitude and orientation of resistive forces experienced by the GETs teeth as it moves through a mining face.

Figure 2.10 shows a general schematic of a P&H 4100C BOSS cable shovel. Major mechanisms of the shovel include the crawler tracks, swing gear, housing for the drive motors, counterweight, boom, hoist rope, dipper handle and the dipper. The mechanisms that are most crucial in determining the forces experienced by the shovel teeth include the drive motors, boom, hoist ropes, dipper handle, and the dipper/dipper teeth.

2.5.2 GET Interaction with Mining Face

In any earthmoving operation, the ground engaging tool completes different actions as it undergoes its dig cycle. As a shovel engages a face three primary actions occur. The dipper must first penetrate the face to start the dig cycle. Once the blade has penetrated the earth, cutting can take place. The cutting action is a lateral motion made by a single, blade-like object; with the penetration and cutting actions working in conjunction, the excavation of material can take place (Blouin *et al.*, 2001).

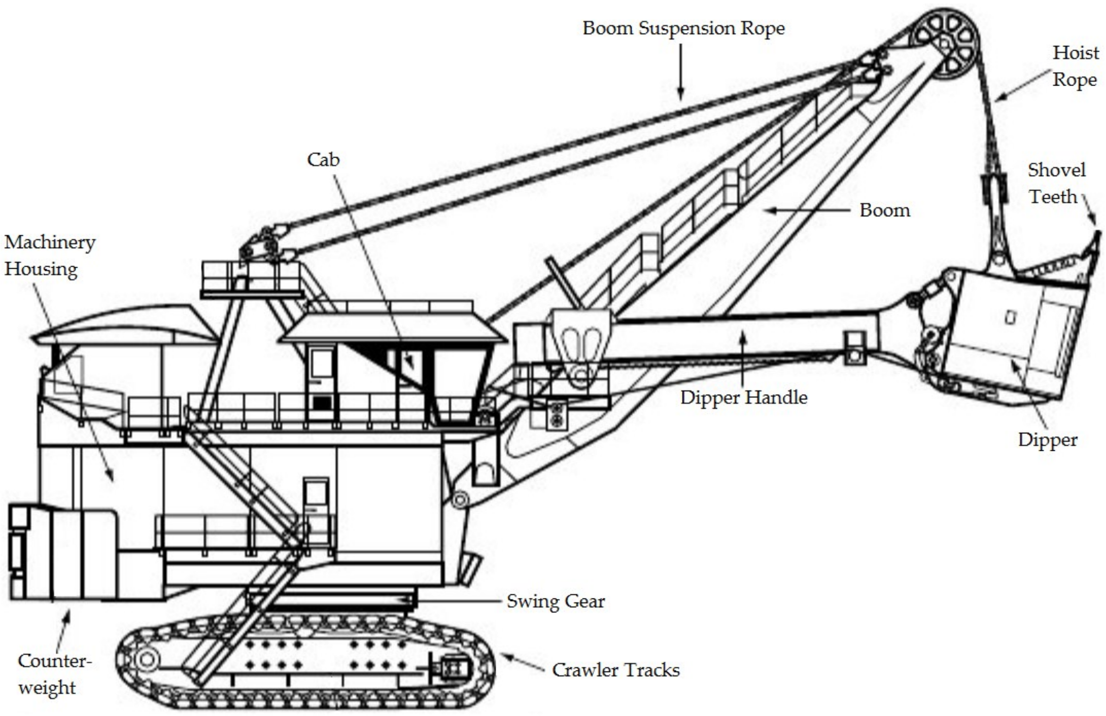

Figure 2.10 - Schematic of P&H 4100 BOSS Cable Shovel (Adapted from Humphrey & Wagner, 2011)

2.5.3 Previous GET Models of Kinematics and Geometry

Simulating the kinematics and geometry of a mining shovel has been attempted by several authors in the past. A simple kinematic model was proposed by Daneshmend *et al.* (1993) where the position of the dipper was determined from boom length, handle extension, and hoist rope length referenced to the dipper teeth. This model considered the handle a beam, and used the saddle block as the origin.

Frimpong & Hu (2004) attempted to simulate the kinematic and dynamic behaviour of hydraulic shovels by varying certain digging parameters when operating in an oil sands environment. Comparisons of shovel performance were made by varying parameters including oil sands properties, oil sands-bucket interactions, bucket dynamics, and operating variables. In order to determine the digging trajectory, reference coordinates had to be resolved about the tooth tip. Figure 2.11 below outlines the coordinate orientations used by Frimpong & Hu for a hydraulic excavator.

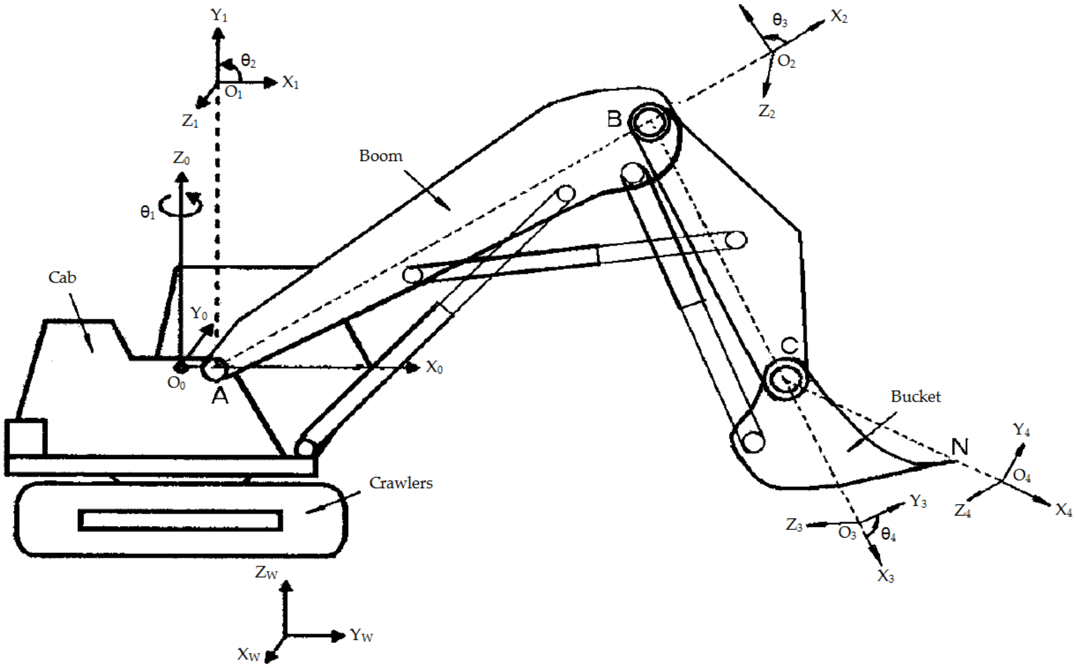

Figure 2.11 - Hydraulic shovel geometry (Adapted from Frimpong & Hu, 2004)

Stavropoulou *et al.* (2013) created a simplified analytical model to determine the forces exerted on a cable shovel dipper. One assumption the previous authors made was to neglect the radius of the sheave wheel, something that was included in the geometric analysis presented in this thesis. Recent work completed by Joseph & Shi (2011; 2012) focused on determining kinematics for cable shovels and a revised dipper-ground equilibrium model for oil sands. The geometry used in their work is similar to the methods that will be employed in this thesis. In the investigation of shovel performance, the forces acting on the handle and dipper are of primary concern. Joseph & Shi (2012) generalized the problem by identifying eleven key forces acting on the handle and dipper, shown by Figure 2.12 below:

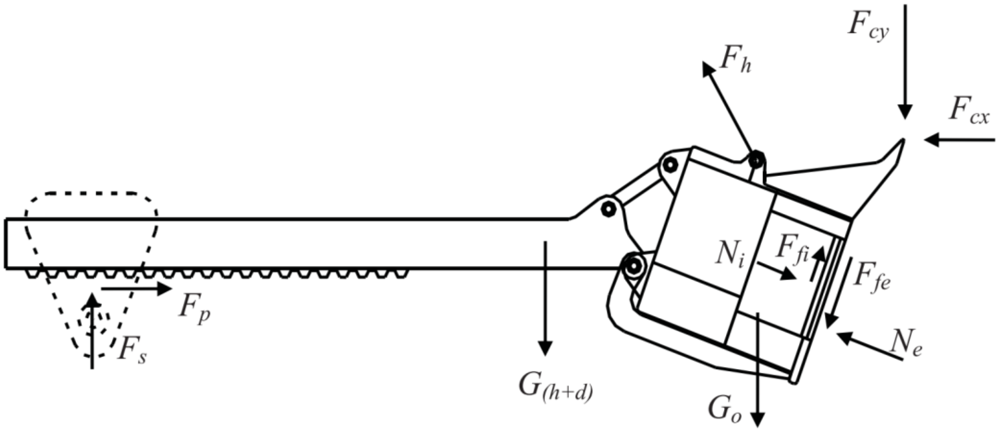

Figure 2.12 - General dipper-handle free body diagram (After Joseph & Shi, 2012)

2.6 Summary

The Athabasca oil sands remain a substantial source of bitumen for Alberta and world markets. The oil sands are much more viscous than conventional oil, and are suspended between extremely abrasive quartz particles. These quartz particles cause significant wear in the surface mining industry. Several wear mechanisms such as microcutting, microploughing, and microfracturing affect GETs and other surface mining equipment.

Investigations into ferrous-based materials and surface engineering techniques have greatly improved abrasion resistance. Advances in chromium and tungsten carbide weld overlays have shown particular promise in surface mining operations including the Athabasca oil sands. Several industry-recognized wear tests are available to help predict wear rates. Most of the standardized tests are for general wear circumstances and need to be tailored to accurately represent specific wear situations.

Recently, computer modelling practices have been applied in order to determine more accurate wear equations and models for a variety of wear circumstances. A crucial part of most wear tests is the ability to scale down real world situations to appropriate laboratory experiments. In the case of GETs and mining operations, shovel performance indicators such as hoist force, hoist and crowd armature voltage and current, dig time and dig velocity are all crucial indicators that can be used to assess a shovel's performance.

In order to accurately determine the forces directly causing abrasive wear on shovel teeth, the forces a shovel experiences while digging through a face need to be resolved to a resistive force acting at the dipper teeth. Previous work on resolving this geometry has been done in the past, and provides the basis to the geometrical analysis performed in this thesis.

3 DETERMINATION OF RESISTIVE FORCES

3.1 Input information required from field

In order to design an experiment that accurately represents real world digging conditions, certain input data was needed from the field. Shovel performance parameters have been measured by a number of individuals in the past including Hendricks (1990), Karpuz *et al.* (1992), and Patnayak & Tannant (2005). Parameters of key interest in predicting shovel performance that have been measured include: hoist rope position, crowd extension, hoist armature voltage and current, crowd armature voltage and current, loading cycle time, dipper fill factor and power on the main AC drive motor.

Through their analysis, Patnayak & Tannant were able to conclude that indicators such as dig cycle time, the hoist motor energy and power, and crowd motor energy and power are useful in evaluating a shovel's performance. However, inconsistency in the digging trajectory can cause significant variability in these indicators even while digging through uniform ground (Patnayak & Tannant, 2005).

The data analyzed in this thesis utilizes many of the performance indicators that were observed by the authors above. Sample data can be seen in Appendix A. Hoist and crowd force values were measured, and also calculated from the recorded armature voltage and current values. Dig velocity was tabulated and the frequency of data collection was 10 Hz. The data was organized in a Microsoft Excel™ spreadsheet and calculations were undertaken in order to determine the resultant resistive forces felt by the dipper teeth throughout the dig cycle. Equations 3-1 and 3-2 allow for the calculation of hoist and crowd force using voltage, current and motor efficiency values to establish a comparison between the measured and calculated values. The additional "2" in Equation 3-1 refers to the presence of two matching hoist motors, whereas there is only one acting crowd motor. The hoist efficiency is taken to be 86.5 %. The crowd efficiency is not included, as it is assumed to be 100 % since it is a much smaller motor compared to the hoist system.

$$F_{Hoist} = \frac{2 * U_{Hoist} * I_{Hoist}}{v_{Hoist}} * \eta_{Hoist} \tag{3-1}$$

$$F_{Crowd} = \frac{U_{Crowd} * I_{Crowd}}{v_{Crowd}} \tag{3-2}$$

3.2 Analyzing Field Data

Raw shovel data was interpreted in order to determine normal resistant forces on shovel teeth operating in a typical oil sands environment. Hoist and crowd positions were resolved and ultimately used to generate an x-y coordinate system to map the shovel's dig trajectory through the face. With the digging profile estimated, resistive forces can be determined as the dipper moves upwards through the face while continually increasing the amount of ore material being excavated. By summing the moments around the intersection of the shovel boom and dipper handle (the saddle point) the total digging resistance was obtained. Resolving this to a normal resistance felt by the shovel teeth permitted the determination of normal resistant forces that could be scaled down to values that were appropriate for experimentation.

3.2.1 Determination of the digging profile

It is difficult to profile the actual dig (or duty) cycle due to the complexity of the motion. The data that was analyzed focused on the excavation movements of the shovel only, and not its absolute position relative to the face. Another key aspect of the digging profile is the degree of dipper penetration. Depending on the crowd extension, the operator can thicken the digging profile (with more crowd extension) or make it relatively thin if the degree of penetration is less. The diggability of the face can also influence the profile as material that is easier to dig through will result in a higher dig velocity and can impact an operator's cut shape.

During the process of determining normal resistive forces, it was assumed that once the shovel had reached the end of its pass, the bucket was completely full of material. A total of 9 dig cycles were analyzed, all of different lengths, so the rate at which the dipper was filled varied from cycle to cycle but the total material being excavated each cycle did not. Following the work laid out by Joseph & Shi (2011) and by obtaining values from a specification sheet of a P&H 4100C BOSS shovel, the appropriate lengths and angles were calculated allowing for the trajectory of the teeth at their tips to be illustrated.

3.2.1.1 Geometry of Dipper Motion

The specifications of the 4100C BOSS shovel were taken from a Joy Global spec sheet and a schematic used by Joseph & Shi (2011). The cable shovel schematic allowed for the measurements of constant values such as boom length, sheave radius, hoist linkage, crowd linkage and others. The geometric motion of the shovel dipper was calculated by combining measurements from the P&H shovel schematic with the methodology outlined by Joseph & Shi (2011).

The specification sheet had a scale where roughly 1 cm = 2 m. It was found that not all squares were precisely the same dimensions thus an average was taken over the majority of the squares on the grid diagram. It was determined that an average of 1 cm = 2.195 m would be used to measure and scale the constant values used in subsequent calculations. The origin of the (X, Y) axis was taken at the centreline of swing rotation of the shovel and ground level. Figure 3.1 below outlines a general diagram of an ultra-class shovel dimensions.

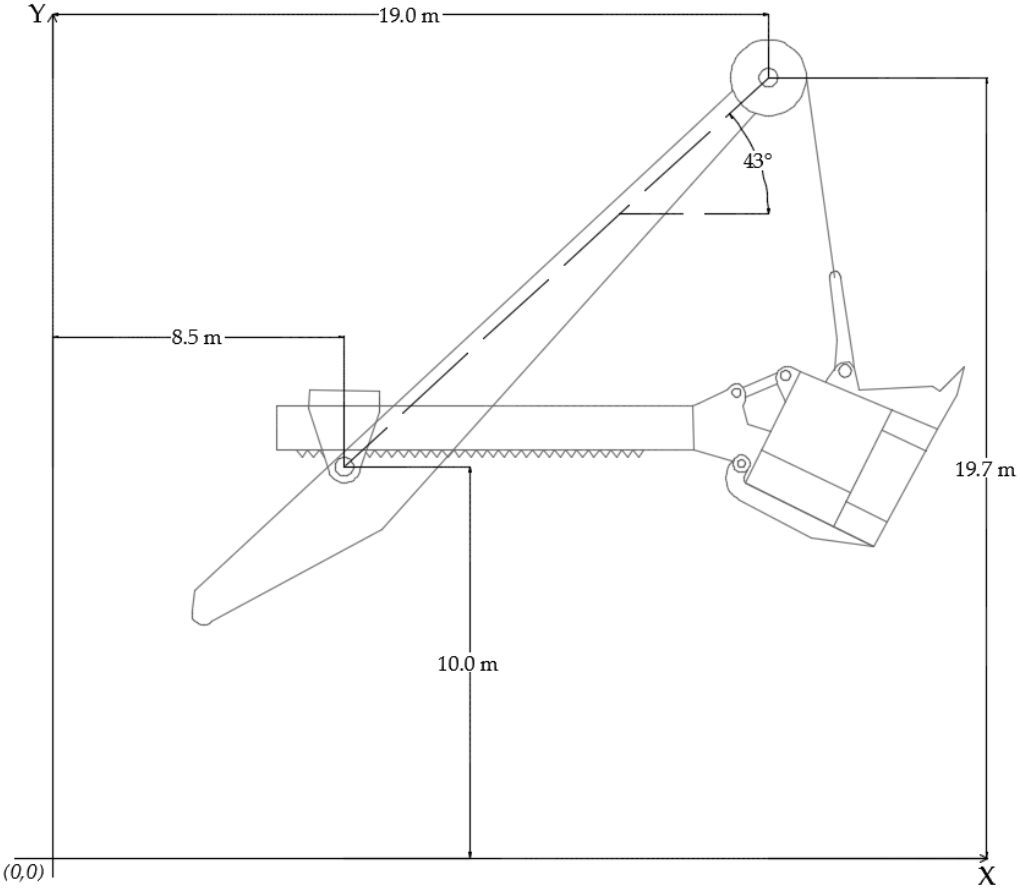

Figure 3.1 - General diagram of ultra-class mining shovel (Adapted from Joseph & Shi, 2011)

Figure 3.2 shows more detailed geometry of the shovel in the X-Y plane. Note that both the total hoist and crowd extension values are measured to a bail point, *A*. In the 2-D plane, the saddle block (*O)* and centre of sheave, *P*, are fixed. In a real world case, the shovel also rotates about the vertical y-axis at some angle η.

The hoist rope moves over the sheave wheel such that the position of P' is not fixed, but the distance from $P - P'$ is fixed. This is the sheave radius, and was measured from the P&H specification sheet; along with boom length, hoist linkage and crowd linkage. The crowd extension and hoist extension values were provided by the raw data. The crowd total value C_t is measured at an angle in Figure 3.3 because calculations involving the shipper shaft and angles to the bail point were made easier by using this distance. This will become clearer in subsequent sections deriving the formulas.

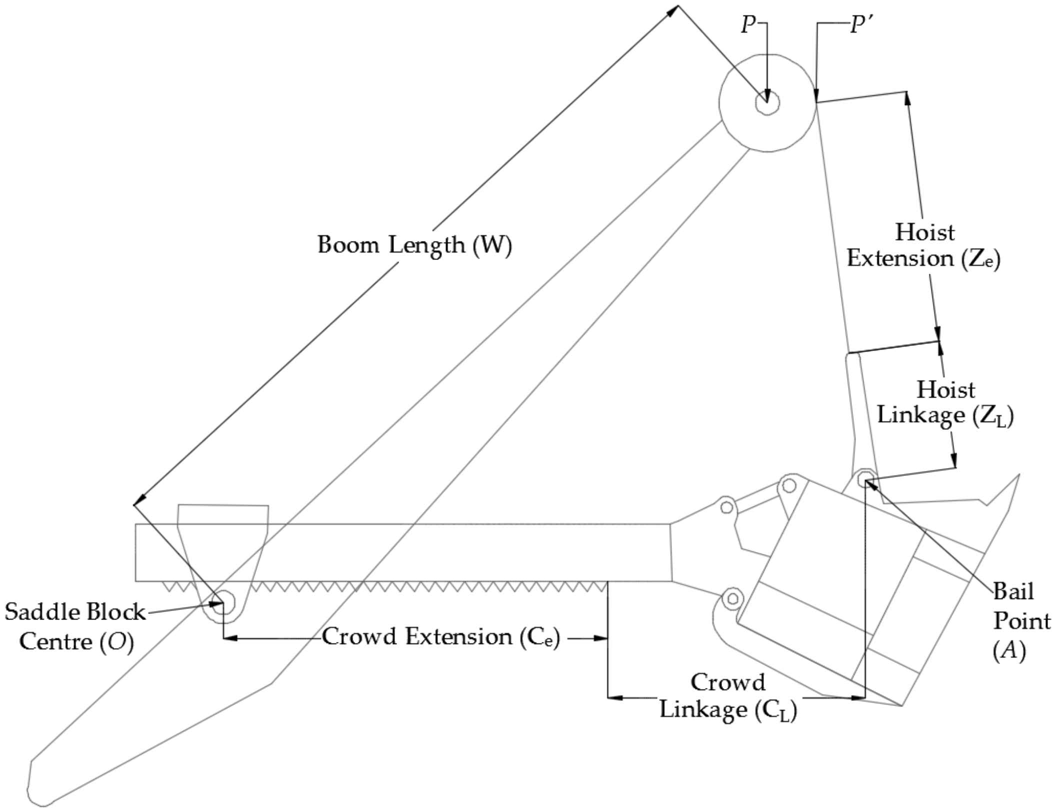

Figure 3.2 - More detailed geometry in X-Y plane

3.2.1.2 *Derivation of Dipper Teeth Motion*

The position of the dipper can now be represented by developing a series of triangles within the existing geometry of the shovel. The following process has been outlined by Joseph & Shi (2011) and is convenient for use here. The triangle *OAP*, represented by the bold lines, uses the bail point to represent the motion of the dipper. The angle created between line *OP* and the horizontal is represented by χ, and is calculated using Equation 3-3:

$$\chi = \tan^{-1}\left(\frac{Y_{sheave} - Y_{saddle}}{X_{sheave} - X_{saddle}}\right) \tag{3-3}$$

The coordinates of the sheave and saddle points are given in Figure 3.1 and yield an angle of χ= 43°. The given values of Z_e and C_e in conjunction with the measured sheave radius allow for the determination of total hoist length Z_t and total crowd length C_t with Equations 3-4 & 3-5:

$$Z_t = \sqrt{(Z_e + Z_L)^2 + r_s^2} \tag{3-4}$$

$$C_t = \sqrt{(C_e + C_L)^2 + r_b^2} \tag{3-5}$$

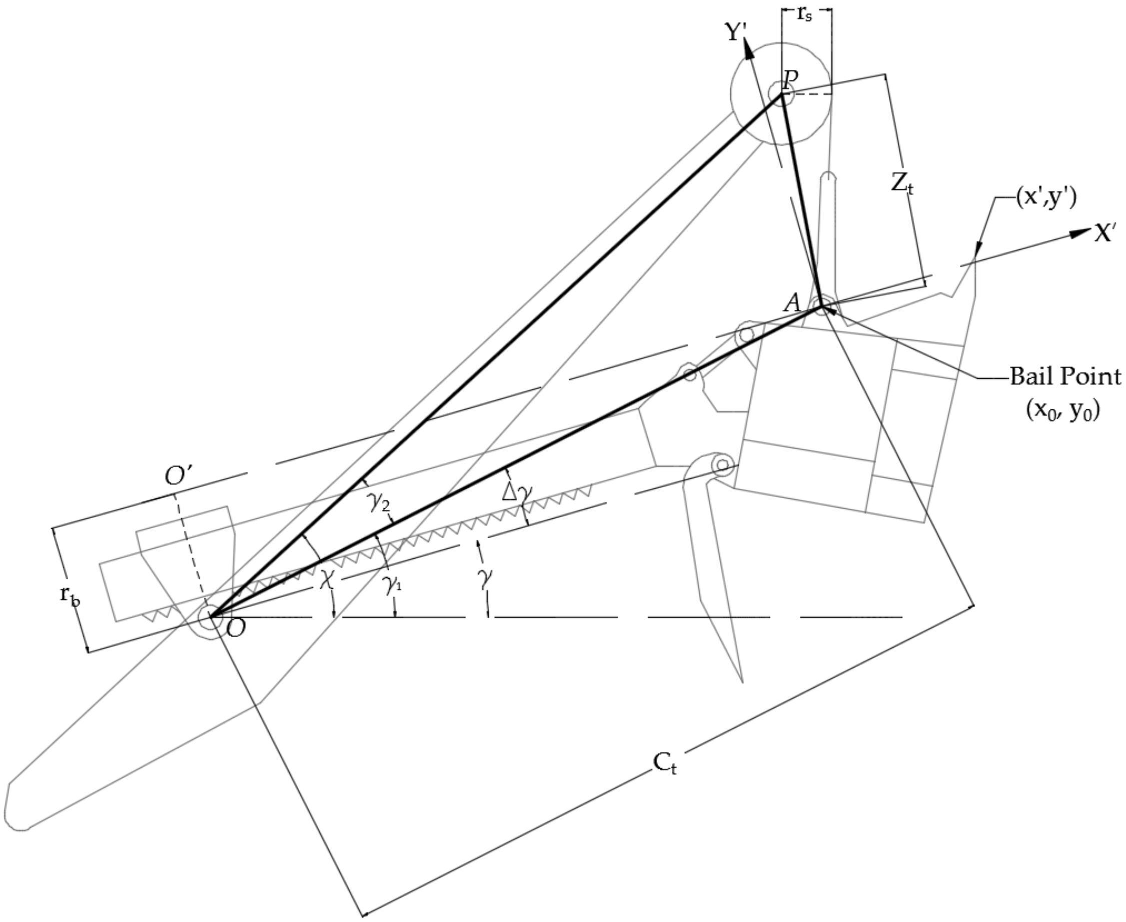

Figure 3.3 - Layout to derive motion of dipper teeth in X-Y plane (Modified from Joseph & Shi, 2011)

Triangle *OAP* (bolded) also provides us with the means to calculate the listed angles. The angle between the boom and the bail point (*A*) can be determined with the boom length, C_t, and Z_t with the application of the cosine law:

$$\gamma_2 = \cos^{-1}\left(\frac{{C_t}^2 + W^2 - {Z_t}^2}{2 * W * C_t}\right) \tag{3-6}$$

It follows that the angle from the horizontal to the bail point is:

$$\gamma_1 = \beta - \gamma_2 \tag{3-7}$$

The internal angle *OAO′* is found via Equation 3-8:

$$\Delta\gamma = \tan^{-1}\left(\frac{r_b}{(C_e + C_L)}\right) \tag{3-8}$$

Therefore γ, the effective handle angle relative to the horizontal, is found via Equation 3-9:

$$\gamma = \gamma_1 - \Delta\gamma \tag{3-9}$$

It is now possible to determine the X-Y coordinates of the bail point (x_0, y_0) and thus possible to determine the coordinates of (x′, y′) with respect to the major X-Y axis which will yield the digging profile from the tooth tip. The coordinates of point *A* are easily found:

$$x_0 = X_{saddle} + C_t \cos \gamma_1 \tag{3-10}$$

$$y_0 = Y_{saddle} + C_t \sin \gamma_1 \tag{3-11}$$

With the coordinates of the bail point determined, it is now a matter of translating the local (X′, Y′) coordinate system back to the 2-D X-Y coordinate system the shovel is operating in:

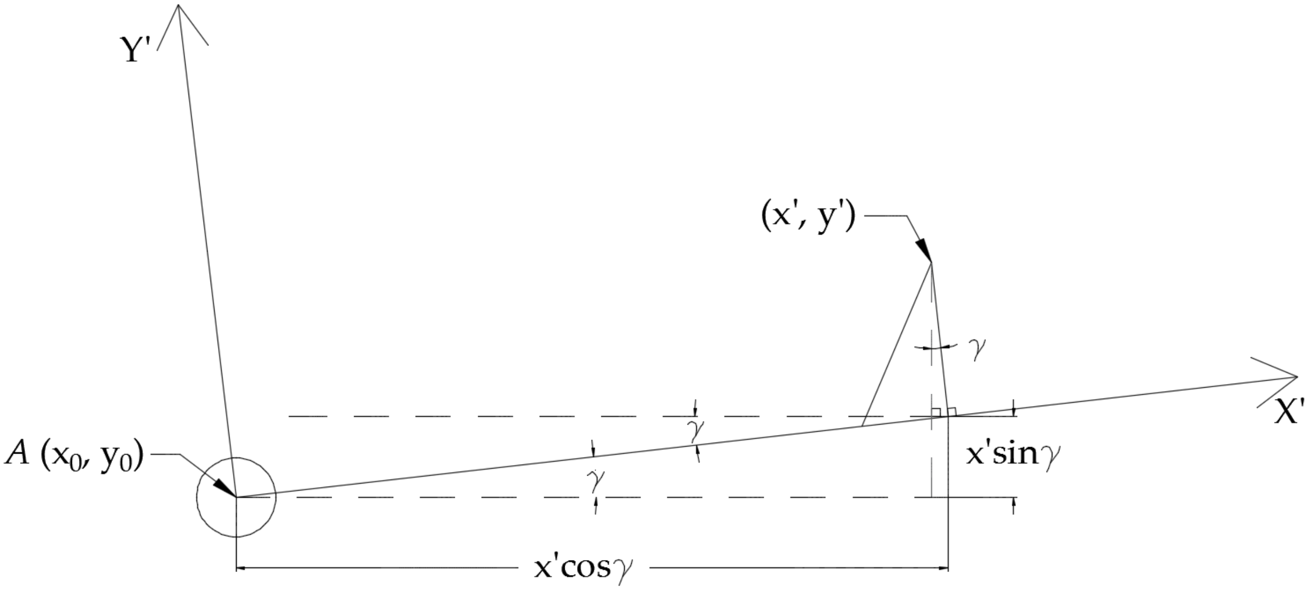

Figure 3.4 - Geometric relation of tooth tip to 2-D plane

Figure 3.4 allows for the (x′, y′) coordinates of the dipper teeth to be determined in relation to the two dimensional (X, Y) plane the shovel is excavating in. There is an assumption that the bottom (or front) side of the shovel tooth is perpendicular to the X′ axis. The x′ and y′ value were measured from the P&H 4100 specification sheet, and were translated to the X and Y axis using Equations 3-12 and 3-13:

$$\boldsymbol{X} = x_0 + (x' \cos\gamma - y' \sin\gamma) \tag{3-12}$$

$$\boldsymbol{Y} = y_0 + (x' \sin\gamma + y' \cos\gamma) \tag{3-13}$$

3.2.2 Dig Cycle Trajectory

Figure 3.5 below illustrates the digging profiles created from the first three passes of the raw shovel data. It is crucial to note that the overall position of the shovel was not known; it is impossible to ascertain if the shovel operator moved toward or away from the face, or if a pass was taken at an angle η different than that of perpendicular to the mining face. Additionally, material may be knocked loose during the previous pass, adding to the unpredictability of the digging profile. The following profiles were created under the assumption that the shovel stayed perpendicular to the face; a procedure that is quite common in oil sands operations. The origin (0, 0) is the centreline of the shovel's swing rotation (y-axis) and ground level beneath the crawlers (x-axis). These dig cycles illustrate a shovel operating in a face approximately 12 metres high, a typical height for oil sands and well within an ultra-class shovel's range.

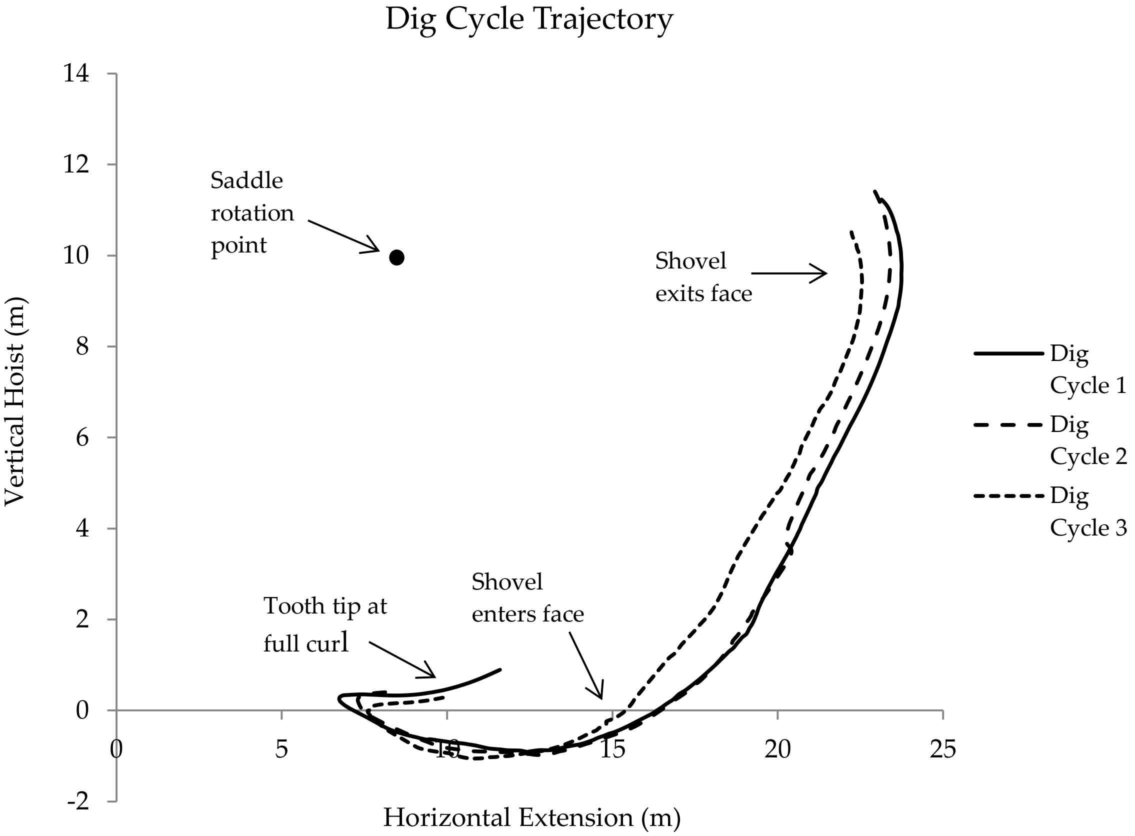

Figure 3.5 - Approximate digging profiles of first three passes

The digging profile was essential in determining the magnitude of the resistive forces acting on the teeth. As the dipper moves upwards through the face, more material rolls in to it, continuously increasing the force acting downward. With the profiles graphed, the amount of material in the dipper at any given point in the dig cycle could be determined and a resultant force calculated.

3.3 Determination of Resistive Forces

In order to determine the normal resistive forces felt on the dipper teeth, several forces had to be considered. Upwards hoist forces were counteracted by the constantly increasing weight of the bucket + material; the point of action of the downward handle force varied with the degree of crowd extension. The author decided that the most effective way of combining all forces would be to compute a resultant moment about the stationary saddle rotation point.

3.3.1 Bucket/Material Weight Moment

With the digging profile estimated and graphed, the calculations of the resistive forces could take place. As the dipper moves upward through the face, the amount of ore in the bucket increases. Therefore the total force exerted downward, and thus the moment felt about the saddle point, is constantly changing. In order to account for this constantly increasing weight, a cumulative area of the dig profile was determined.

With a list of (X, Y) coordinates generated, segments or "strips" of dig area could be found by multiplying the difference in the current and preceding coordinate values. That is:

$$Dig\ Segment\ Area = |(X_i - X_{i-1}) * (Y_i - Y_{i-1})| \qquad \textbf{(3-14)}$$

By summing all segment areas generated from Equation 3-14 a total dig value was obtained. A unitless area ratio could then be computed by dividing each dig segment area by the total dig area. Subsequently, a cumulative area ratio was calculated to represent the amount of material in the dipper at each given coordinate. As previously mentioned, it was assumed the bucket was 100 % full at the end of each pass, so the cumulative area value was equal to one at the end of each cycle, indicating a full bucket. Any spillage due to the excavating process was considered negligible and the material was assumed to be homogeneous.

Multiplying the cumulative area value by the weight of material in a full bucket yielded the total force, in kN, experienced due to the dipper weight and increasing material weight at each respective coordinate point. The total weight of material in a full bucket was determined via Equation 3-15:

$$G_{ore} = \rho * \left(\frac{V_B}{SF}\right) * g \qquad \textbf{(3-15)}$$

Where ρ is density of oil sand, V_B is the total bucket volume; SF is swell factor (taken to be 1.3) and g is acceleration due to gravity. The total weight of the empty bucket was taken from Lin (2013) and is equal to 792.76 kN.

The centroid of the bucket and ore was assumed to be in the same place to simplify the moment arm calculations. In reality, the centroid of the empty bucket remains constant in the centre and the centroid of the material mass would change as more ore flows into the bucket. This has been investigated previously (Hemami *et al.*, (1994); Stavropoulou *et al.*, (2013)) and as the bucket becomes more and more loaded it is clear the centroid of material moves towards the centroid of the empty bucket. For this reason the moment arm of the bucket/dipper combination was taken to be at one location. The moment arm was calculated as follows:

$$L_{b+o} = (C_e + C_{BC}) * \cos\gamma \tag{3-16}$$

Where C_{BC} represents the constant length from the edge of the crowd teeth to the centroid of the bucket + ore.

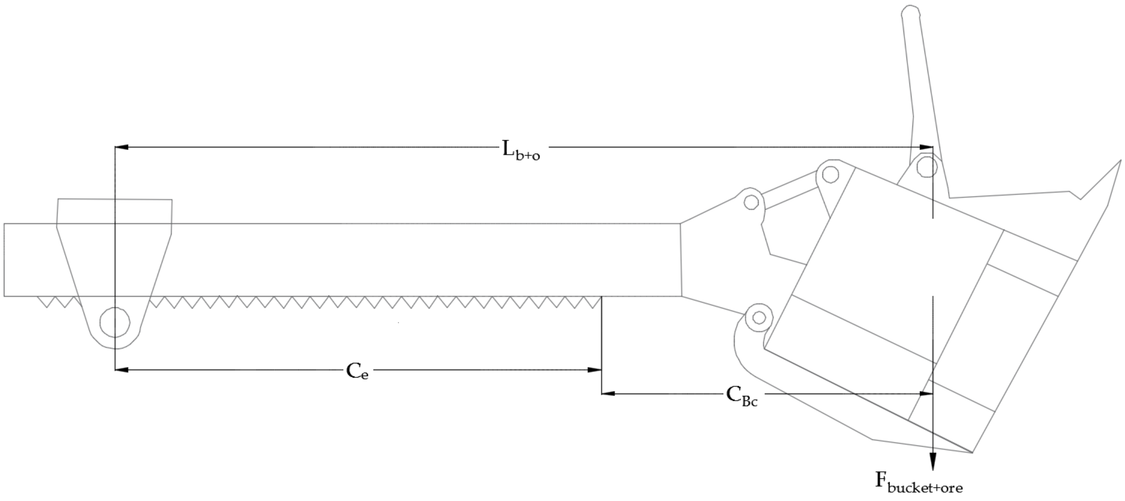

Figure 3.6 - Moment arm of dipper & material acting about the saddle

The total moment caused by the bucket and ore at any instant in the duty cycle:

$$M_{b+o} = (G_{bucket} + G_{ore}) * (L_{b+o}) \tag{3-17}$$

3.3.2 Handle Weight Moment

In order to determine the moment induced by the handle weight, the total handle length had to be known. This value was measured from the schematic of the P&H 4100C BOSS spec sheet. The total handle weight was taken from Lin (2013) to be 380.79 kN. As the handle extended and retracted, the moment about the saddle changed. To improve accuracy, the remaining handle length behind the saddle (opposite to the dipper) was also accounted for. This opposite handle measurement counteracts the moment created by the handle on the side of the mining face. The magnitude of the handle moment varies throughout the dig cycle, as it depends on the degree of crowd extension, and thereby dipper penetration.

The handle extension is calculated by:

$$H_e = C_e + C_H \tag{3-18}$$

The crowd extension, C_e, provided in the raw data was assumed to be from the saddle rotation point to the end of the teeth that the handle can travel on. The constant value C_H was measured on the specification sheet from end of the crowd teeth to the edge of the handle. In Figure 3.7, the edge of the handle from the spec sheet is represented by the bottom rotation point of the bucket, and was assumed to be rectangular for ease of calculation purposes.

The extension on the opposite side of the saddle is given by:

$$H_{e'} = H_L - H_e \tag{3-19}$$

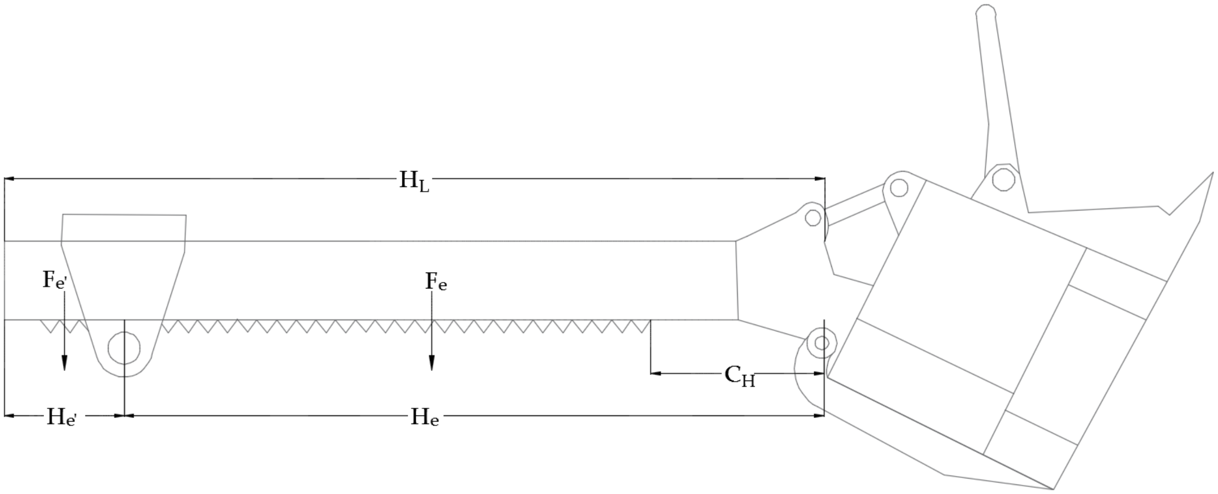

Figure 3.7 - Location of handle forces acting about the saddle block

F_e and $F_{e'}$ are located at the centroids if the handle was treated as two separate rectangles split at the saddle point. They can be represented by the total handle length and its unit weight. This reduces the net moment of the rectangular handle about the saddle point to:

$$M_h = \left(\frac{H_W}{H_L}\right) * \left(H_e^2 - H_{e'}^2\right) * 0.5 * \cos\gamma \tag{3-20}$$

3.3.3 Hoist Force Moment

It was determined that the hoist force rather than crowd force is the dominant force contributing to the digging resistance, which is consistent with the results found by Stavropoulou *et al.* (2013) comparing hoist and crowd specific energies.

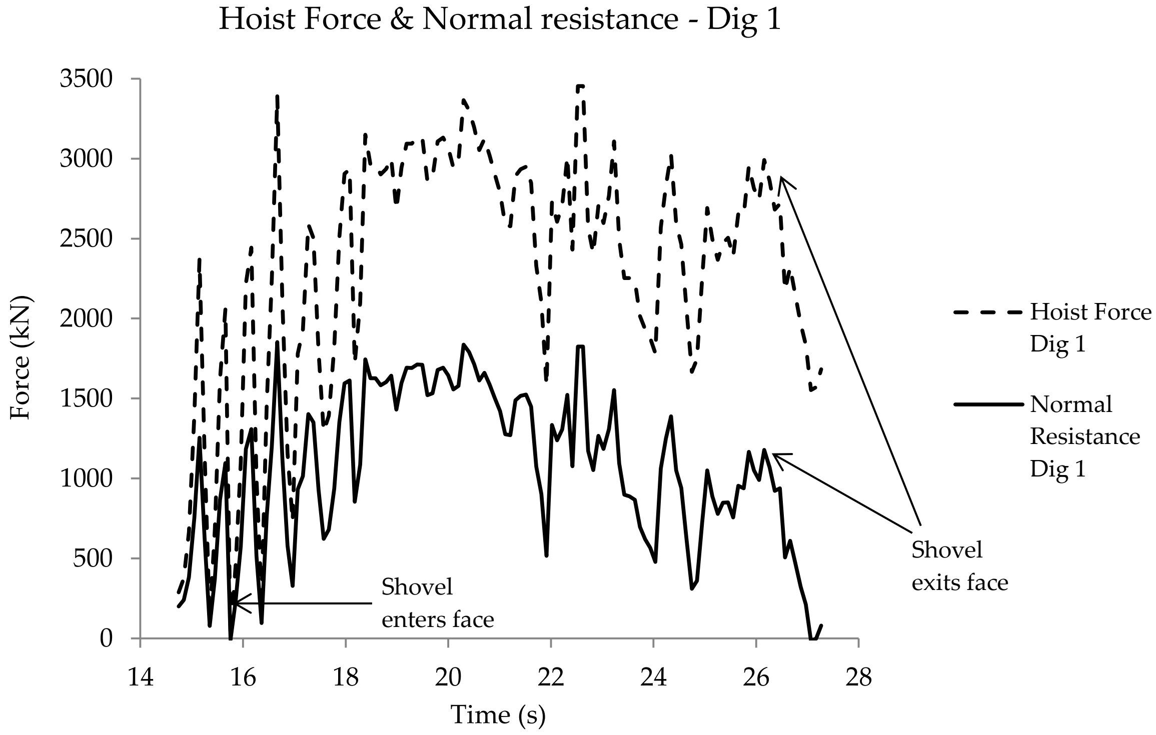

Figure 3.8 - Hoist and normal resistive forces shown for dig cycle 1

Figure 3.8 shows the hoist force experienced by the shovel (dashed line) compared to the normal resistance force (solid line) that the shovel teeth experience. The graphs have a similar shape but the magnitudes are significantly different. The hoist force values are taken directly from the raw data.

The initial ramp up from t = 15 s to approximately 18 s is expected as the dipper engages the face and begins to cut through the oil sand material. The force then remains relatively constant as the shovel moves through the face with the fluctuations due to varying diggability throughout the face. The sudden drop in both hoist force and resistive force at approximately 26 seconds indicates that the shovel bucket has exited the face.

The moment arm of the hoist force was taken to be the distance from the saddle block to the hoist rope. Unlike the bucket + ore and handle moments, the direction of the hoist force was not directly vertical. Instead, the hoist force direction varied slightly as the hoist crowd handle extended and retracted, changing the position of the rope on the sheave wheel. Equation 3-4 showed that the effective hoist release Z_t is the hypotenuse of triangle PAP'. It follows then that the internal angle between the hoist rope and effective hoist release is:

$$\theta = \tan^{-1}\left(\frac{r_s}{Z_e + Z_L}\right) \tag{3-21}$$

The angle between the saddle-bail point and sheave-bail point (OAP) is found with the cosine law:

$$\alpha = \cos^{-1}\left(\frac{Z_t^2 + C_t^2 - W^2}{2 * Z_t * C_t}\right) \tag{3-22}$$

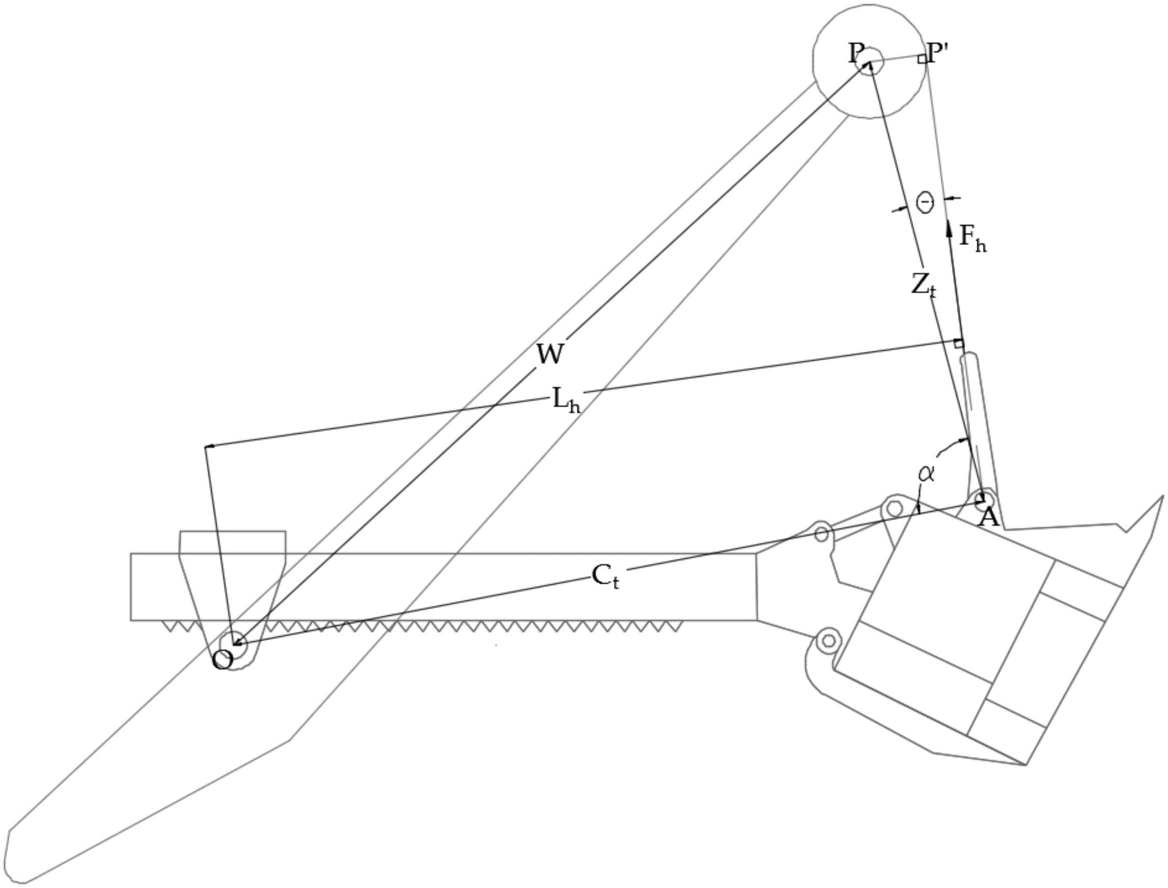

Figure 3.9 - Geometry used to determine hoist moment arm

Thus the moment arm of the hoist force is determined by:

$$L_h = C_t * \sin(\theta + \alpha) \tag{3-23}$$

The moment created by the hoist force is then found:

$$M_{hf} = F_h * L_h \tag{3-24}$$

3.3.4 Total Resistive Moment

With three moments acting about the saddle point calculated, the total resistive moment acting at the shovel teeth about the saddle could be determined. This total moment is equal to the moment created by the action of the shovel digging through the face. That is, the total digging effort P is equal to the total digging resistance F_R. What remained was the angle that the resistant force acted, relative to the horizontal, and the length from the saddle block that the resistance force occurred at. Dividing the total moment by the resistance force moment arm would yield the total resistive force acting on the dipper teeth. This could then be resolved into a normal force acting upon the teeth, providing the means to set up the laboratory wear test.

The hoist force acts in the opposite direction to the forces experienced by the handle and dipper, so summing the moments around point O yields:

$$M_T = M_{hf} - (M_{b+o} + M_h) \tag{3-25}$$

Following the work of Joseph & Shi (2012) and their revised model for dipper-ground interactions, the angle of total digging resistance was found using the dipper rake angle β, the angle between the handle and horizontal γ, and the tooth-oil sand friction angle δ. The total digging effort P and total resistive force F_R, act in exact opposite directions. The dipper rake angle was measured in AutoCAD to be 61°, and it was considered reasonable to use 37° as the tool-oil sand friction angle; determined as the peak friction angle for compacted oil sand by Dusseault & Morgenstern (1978). In this work, the angle from the handle to horizontal γ is negative below the horizontal and positive above it. Following this, Equation 3-26 outlines the calculation of τ:

$$\tau = \beta + \gamma \tag{3-26}$$

And the resistance angle ψ:

$$\psi = \tau + \left(\frac{\pi}{2} - \delta\right) \tag{3-27}$$

Figure 3-10 on the following page outlines the geometry used to determine the resistance angle.

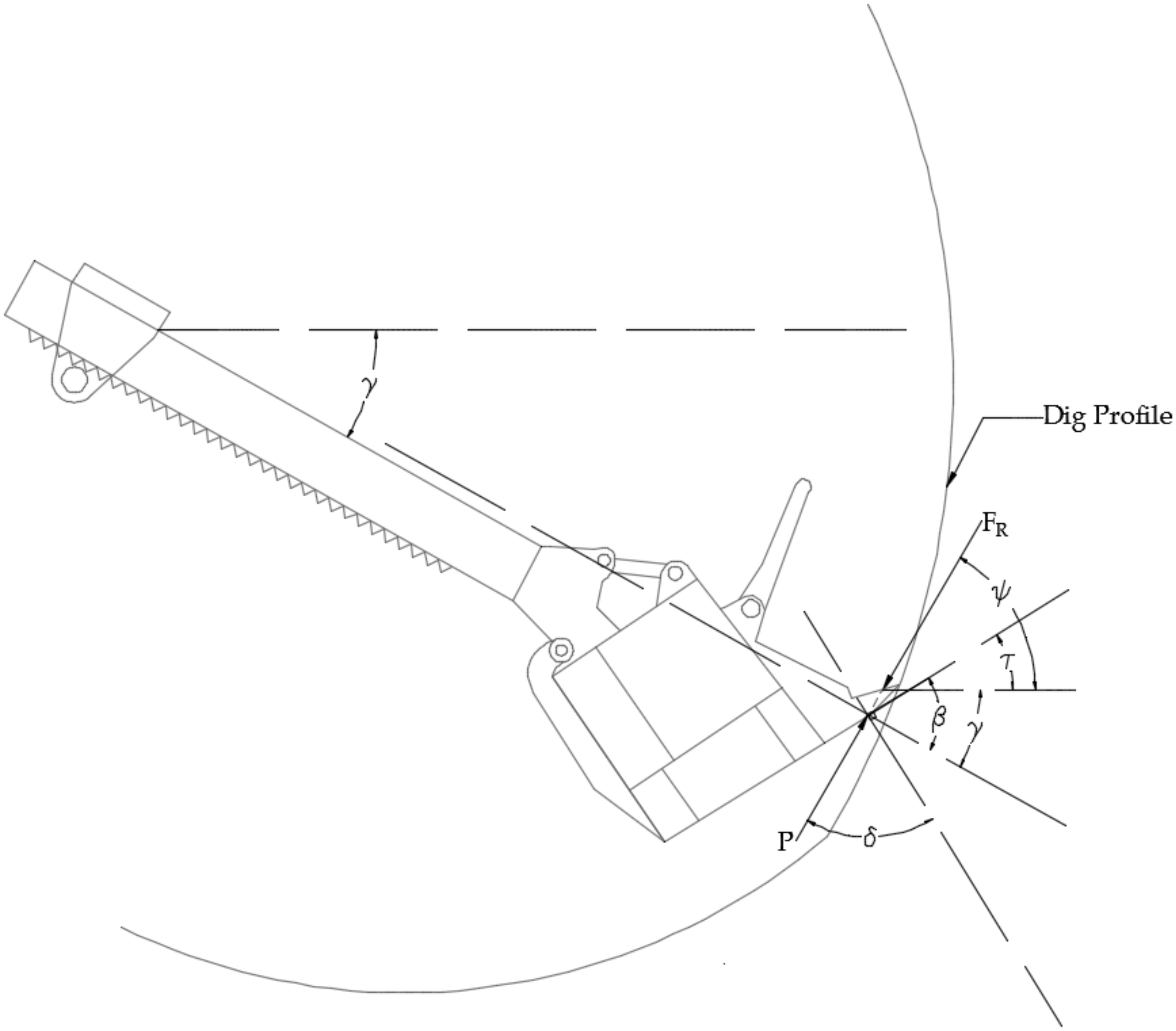

Figure 3.10 - Approach used to determine digging resistance angle from horizontal

This angle of resistance allows for the calculation of the moment arm that the force is acting at. In order to determine the length of the constantly changing total resistance arm, angles between the saddle block, sheave wheel and dipper teeth have to be calculated. The spot of resistive action on the teeth was taken to be the location that a line travelling through the bail point, parallel to the shovel handle, would intersect. In practice, the whole tooth is engaged in the face so the precise location of this force was not considered to be consequential. The length L_{OC}– the distance from the saddle block to the tooth point of action – was determined from:

$$L_{OC} = \sqrt{(C_e + C_{LT})^2 + r_b^2} \tag{3-28}$$

The distance C_{LT} represents the constant length from the end of the crowd teeth to the location of the resistant force; taken from the P&H 4100 specification sheet. The distance from the saddle block to the bail point is given by Equation 3-5. The small internal angle between the teeth, saddle block, and bail point can be determined via:

$$< COA = \cos^{-1}\left(\frac{(L_{OC}^2 + C_t^2 - L_{AC}^2)}{2 * L_{OC} * C_t}\right) \tag{3-29}$$

The constant length L_{AC}, identified from P&H 4100 specs, is equal to rotation height of the bail point with respect to the saddle block, r_b.

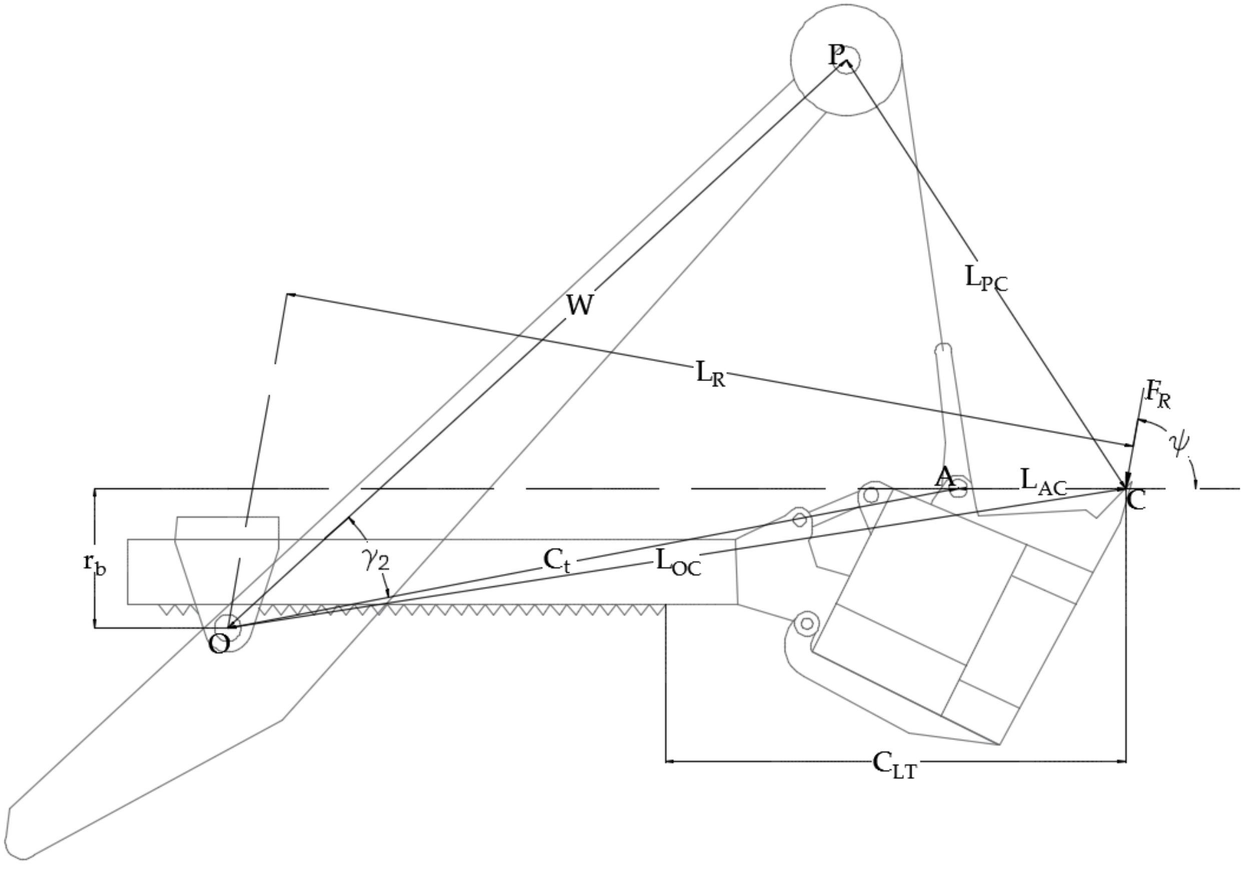

Figure 3.11 - Geometry of resistance moment arm

The length from the centre of the sheave wheel P to point C can now be ascertained by:

$$L_{PC} = \sqrt{W^2 + L_{OC}^2 - 2 * W * L_{OC} * \cos(< COA + \gamma_2)} \tag{3-30}$$

Determining $<OPC$ and $<OCP$ using the cosine law similar to $<COA$ in Equation 3-29 yields:

$$< OPC = \cos^{-1}\left(\frac{(W^2 + L_{PC}^2 - L_{OC}^2)}{2 * W * L_{PC}}\right) \tag{3-31}$$

$$< OCP = \pi - < OPC - (< COA + \gamma_2) \tag{3-32}$$

The boom angle *β*, dig resistance angle *ψ*, and internal angles of the triangle *OPC* are the necessary parameters to determine L_R, the resistance arm value.

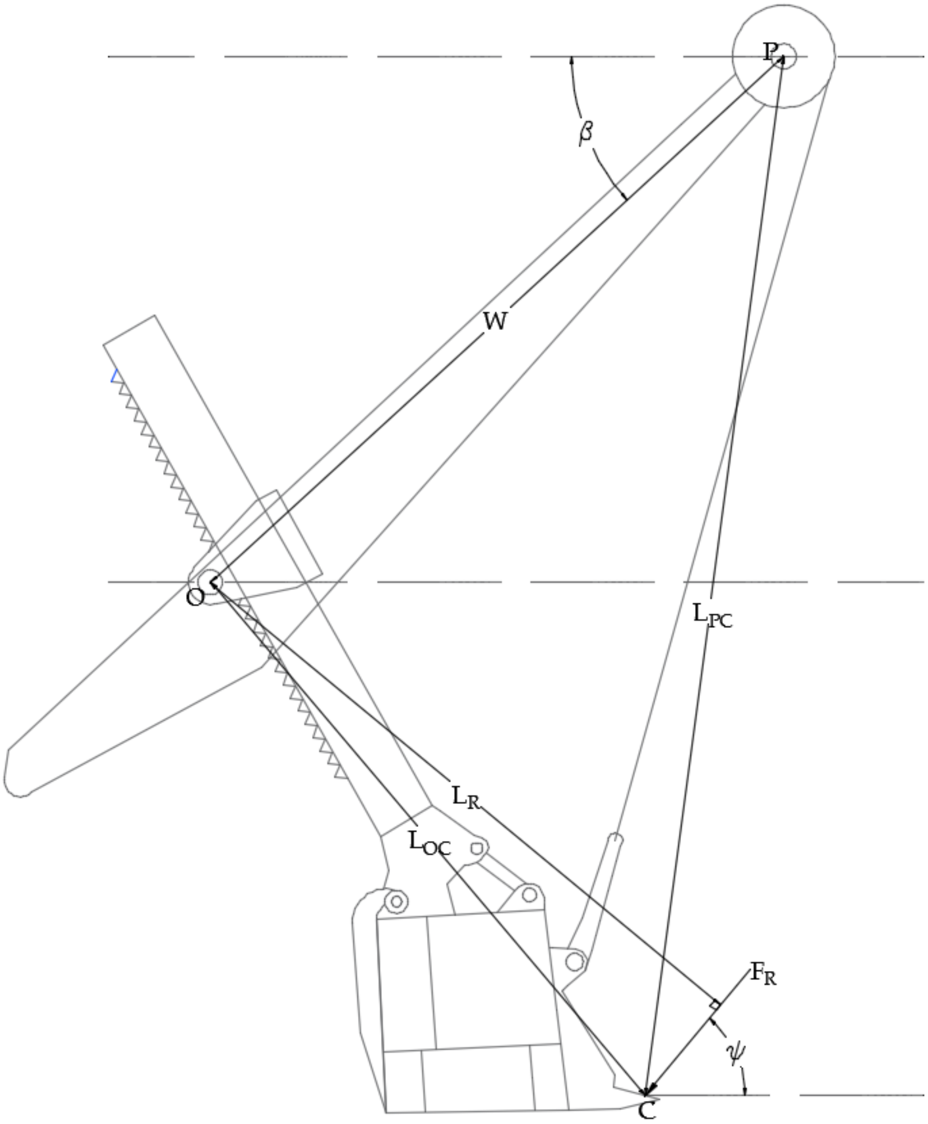

Figure 3.12 - Geometry of the total resistance moment arm

Finally, the resistance arm length L_R can be established from:

$$L_R = L_{OC} * \sin(\beta + < OPC + < OCP - \psi) \tag{3-33}$$

By dividing the total moment about point *O* by the resistance arm L_R, the total resistive digging force can be computed. For the purpose of this thesis, this total resistance was resolved in to a normal force acting on the top side of the dipper tooth face. The geometry of this is represented by Figure 3.13 and Equation 3-34:

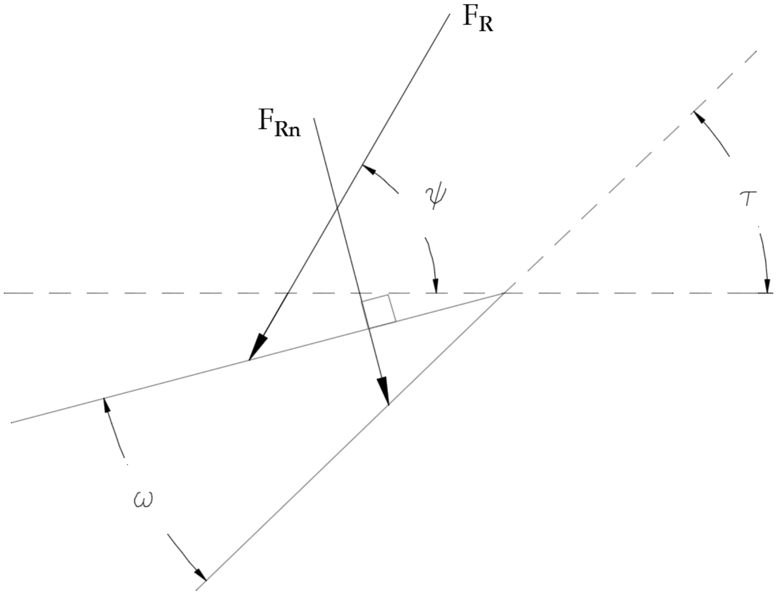

Figure 3.13 - Resolving total resistive force at tooth tip to a normal force

$$F_{Rn} = F_R * \sin(\psi - \tau + \omega) \tag{3-34}$$

The internal tooth angle ω was measured from unused shovel teeth and was found to be 17°.

3.4 Scaling of Field Force Values

Scaling is a powerful tool that, when properly used, enables an individual to take a complex engineering task and reduce it down to a measureable, testable size. Practically all surface mining operations function on a scale that is too large to re-create in a lab setting. The equipment is far too massive and resulting forces too great to create repeatable experiments. Ground engaging tools such as shovels can frequently (over 25% of the time) experience forces between 2000 and 3500 kN when digging through a face. These large digging resistance forces cause significant wear on shovel teeth and bucket linings. This is a testament to how important it is to design a scaled down lab test that can be repeatedly and accurately used to predict or evaluate wear in the field.

3.4.1 General Scaling Laws

It is well known that the scaling law between area and length is a square-power law. That is to say, if a square of side x becomes a square of side $2x$ then it follows that every length in the original square has doubled, but the total area has actually squared. The same pattern is observed when dealing with a square of side $3x$. The total length of each side has tripled, but the total area has increased to $9x^2$. That is, the ratio of areas is equal to the ratio of lengths, squared (Denker, 2015).

This trend is not limited to square shapes. A triangle of base x that is increased to $2x$ will have the corresponding area increased by four times, following the square law discussed previously. The key idea is that if the width and height are both scaled up by some factor K then the area is scaled by a factor of K^2. Figure 3.14 illustrates this below:

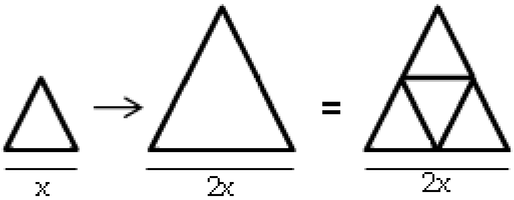

Figure 3.14 - Small and large triangles showing the area square law (after Denker, 2015)

Scaling of volumes follows a similar trend, but is a cube-power law. Consider the original square of side length x now forming a cube of volume x^3. Once again, increasing every length to $2x$ makes the cube twice as tall, twice as wide, and twice as deep. This is three factors of two, increasing the volume by eight, or 2^3, hence the cube-power law. The surface area, however, increases by a factor of four (as per the square-power law) because none of the six surfaces actually have any depth (Denker, 2015).

3.4.2 Determining a Scaling Factor

In order to accurately perform the modified G65 test, the normal resistance force values were scaled down to appropriate magnitudes. The scaling factor was calculated by determining an area ratio from a shovel tooth compatible with a P&H 4100 BOSS shovel and a wear scar created using the modified apparatus and an extra sample coupon. The surface area of one shovel tooth that interacts with material during excavation was measured to be 1126 cm^2, calculated from adding the top and side surfaces of the field tooth. The sample test done on an extra hard-faced coupon generated a wear scar with an area of 4.4 cm^2. The scale factor was determined using Equation 3-35:

$$ScF = \sqrt{\frac{A_{Tooth}}{A_{Coupon}}} \tag{3-35}$$

Inputting the measured area values yields:

$$ScF = \sqrt{\frac{1126}{4.4}} = 16$$

In order to scale the field force values down to a lab suitable magnitude, this scaling factor was applied in a cube-root fashion.

$$ScF = \sqrt[3]{\frac{F_{Tooth}}{F_{Coupon}}} = 16 \tag{3-36}$$

3.4.3 Field Force Values

The incorporation of the linear actuator allowed for the force exerted on the coupon to change throughout the testing process. As Figure 3.8 shows, there is an initial ramp-up period when the bucket engages the face. This was represented in the test by constantly increasing the force in a more or less linear fashion until a maximum was reached.

The maximum value was determined from averaging the normal forces experienced once the bucket was moving through the face to when it exited. The instant the bucket was considered to be moving through the face was judged graphically based on when the ramp-up sequence seemed to end. The exit of the bucket from the face was very apparent as there was a sudden drop in the forces being exerted. Each of the nine cycles had their max force averaged, and then all nine of the averages were taken to create one representative magnitude. Throughout the data, there were some erroneous values that were not considered as they were either far too great of a magnitude or were negative values and represented data anomalies rather than accurate readings. The standard deviation of force values for each cycle was calculated; an average of these values was used with the average force magnitude in order to find the maximum and minimum test values in the laboratory.

Table 3.1 - Field force values and the applied scale & lever arm factors

Description	Value
Avg. Peak Field Normal Force	1231 kN
Field Std. Deviation	403 kN
Scale Factor	16
Lever Arm Factor	2.82

The average length of the ramping period was three seconds, and the average amount of time digging through the face was approximately ten seconds. These are very typical values for ultra-class cable shovels operating in oil sands environments. The differences between the cycle times would correlate to the diggability of certain sections in the face as well as operator intention.

4 EXPERIMENTAL PROCEDURE

The standard ASTM G65 abrasion test has five procedures to choose from (A, B, C, D, and E) depending on the test specimen's wear resistance. All five procedures detail application of a constant load over an established lineal abrasion distance. The abrasive material used is rounded quartz (or silica) sand, and the rotation speed of the wheel is 200 RPM. The proposed modified G65 test performed in this thesis incorporates several important changes to the standardized test in order to more accurately reflect field conditions of a GET digging through an oil sands mining face. The material used as the abrasive throughout the modified tests is bitumen stripped post hydro-transport oil sand, substituted for the standard silica sand. The wheel revolution rate is also modified; the rotation speed of the wheel is set to match the average digging speed of the shovel bucket from once it enters the mining face to when it exits. Considering the diameter of the wheel used in this thesis, the linear velocity converted to revolutions is equal to 100 RPM. Attached to the laboratory wheel motor is an ammeter and voltmeter to measure the power draw during the abrasion process. This will help validate the modified tests ability to predict field wear. The most important feature of the modified test is the implementation of a linear actuator & stepper motor. This combination is what facilitates the force-varying capability. It can be varied via manual control or by the use of a computer program, thereby realistically reflecting real-world conditions.

Supplement to performing the proposed modified test, a constant load test on two re-surfaced coupons was run that can compare volume loss results obtained from the modified test to similar G65 conditions. This additional test will subject the coupons to a constant 130 N normal load as per G65 standard and use rounded quartz sand as the abrasive media. Although the standard G65 test lists procedures with set lineal abrasion distances, the additional test performed here will not adhere exactly to the stated G65 test conditions. Instead, the total lineal abrasion distance will match the distance used in the proposed modified test, 525 metres, to allow for more accurate analysis of volume loss and wear scars between the cyclical and constant load tests. The listed abrasion distances in the G65 standard are all too high or too low to meaningfully compare results, which could appear significantly skewed by the discrepancies in abrasion distance.

The rotation rate of the wheel during the constant load test will similarly be altered from practiced G65 procedures. The wheel will rotate at 100 RPM, in order to keep the linear velocities of the proposed modified test and additional test equal. However, standard G65 parameters such as a constant normal force and the type of abrasive media will be observed.

An analysis of the wear results between the proposed modified test and the supplementary test can be made to investigate the effects a fluctuating load has on wear rate and wear properties compared to a constantly applied load.

Section 4.3 details how the actuator and lever arm were mounted, as well as the hopper and nozzle setup that fed abrasive media between the wheel and coupon. All of the cyclical and constant load tests were completed in a laboratory at 20° C, with the proposed modified test following the same repeatable procedure outlined in Section 4.4.

4.1 Characteristics of Abrasives

Particle size has a significant effect on the wear rate of materials. In metals, abrasive particles with a size of 100 μm or more have a minimal effect on the wear material. For abrasives with a particle size less than this threshold, the wear rate decreases rapidly with decreasing particle size. This result can be attributed to smaller particle sizes favouring elastic contact rather than plastic (Hawk & Wilson, 2001). A standard G65 test uses silica test sand as the abrasive medium. The material used for the modified experiments performed in this thesis is bitumen stripped oil sand from a deposit located in Northern Alberta. The material is post hydro-transport, but still retains significant abrasive qualities as the sand is not ground or crushed during transport. The transport slurry is approximately 70 % fluid and 30 % solids, resulting in particle suspension during transport. Approximately 31 kg of material was used, and this material was dried and sieved before testing.

Figures 4.1 and 4.2 below are detailed images of the bitumen stripped, post-hydro transport oil sand abrasive taken with a scanning electron microscope. The close-ups show that the particles are still quite angular, and vary in size from approximately 50 – 200 μm across.

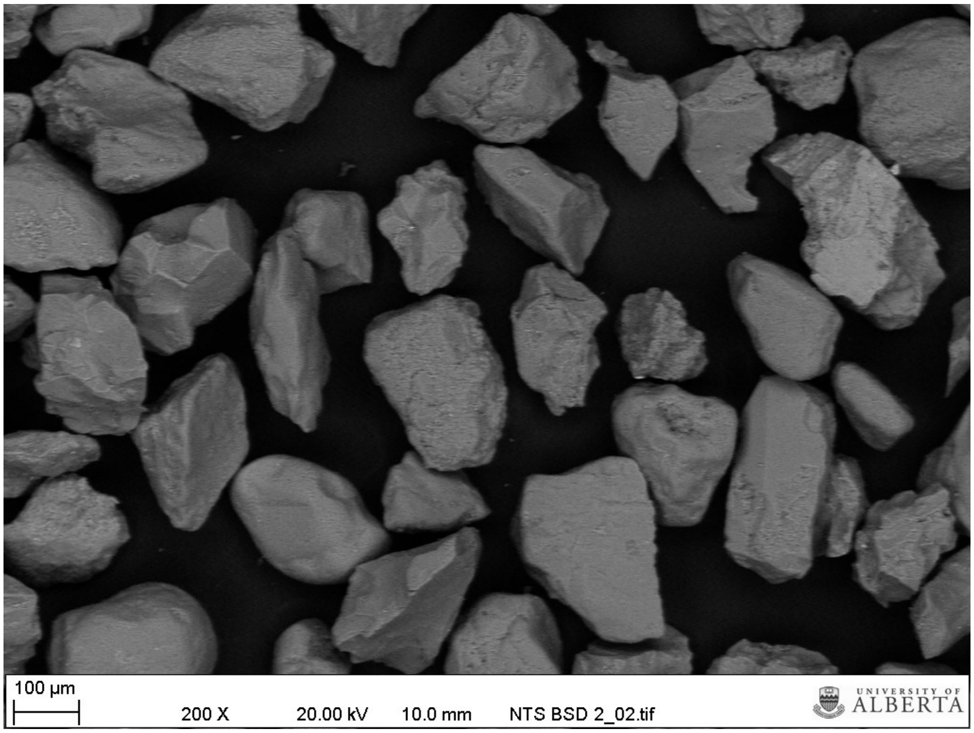

Figure 4.1 - Close-up image of tailings sand abrasive. Magnification 200x

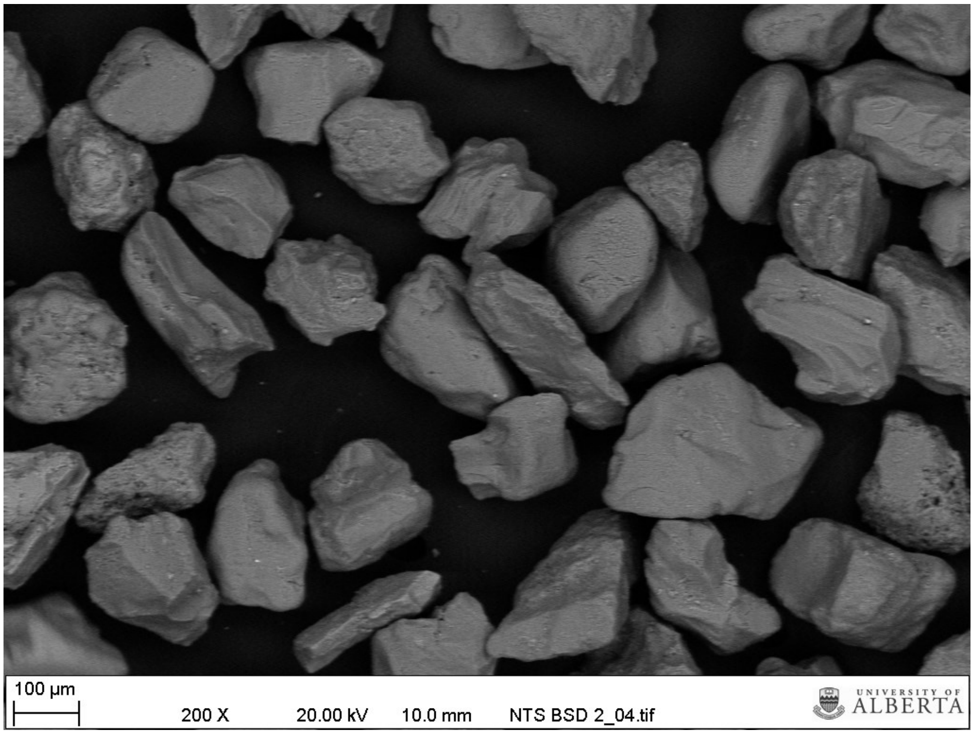

Figure 4.2 - Alternate close-up of tailings sand abrasive material. Magnification 200x

Figure 4.3 below shows many more particles and better displays the size variability. It is clear the particles are sub-angular to angular and differ in shape quite dramatically.

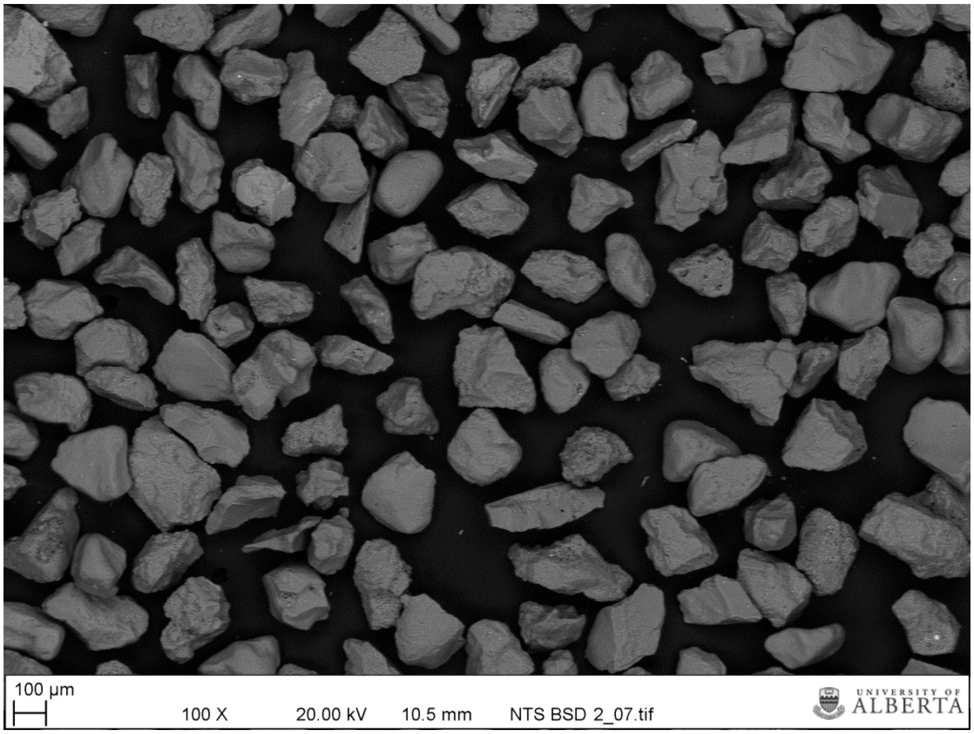

Figure 4.3 - Zoomed out image of tailings abrasive sample. Magnification 100x

In all of the above images, the white particles represent the oil sand tailings abrasive used. Each particle may not be the same material, however. Most will be quartz while others will be different constituents of oil sands. The black background is not bitumen (see Figure 2.2) but instead is the carbon tape the samples were prepared on. To produce the image, the particles were carbon coated to make them conductive. More images of the abrasive can be viewed in Appendix B.

The thought process behind using bitumen stripped oil sand material rather than the standard rounded quartz grain sand is to more accurately represent the digging conditions of GETs in the Athabasca oil sands. This substitution follows that any material reduced to an appropriate size distribution has the potential of being substituted in as the abrasive media. This modification has a wide variety of applications. Shovels experiencing wear in blasted hard rock mines could be analyzed by using the crushed rock as the abrasive material in the modified G65 test. The size of the nozzle opening can be adjusted to represent the particle size of the material in question and ensure proper flow. For the experiments performed in this thesis, the flow of abrasive was between 350 – 400 g/min; the recommended flow rate of the standard G65 test.

Figure 4.4 below is a SEM image of silica sand used in the standard G65 test and as the abrasive in the constant load tests. The particles are more uniform and are more rounded than the stripped oil sand material; even after having been hydro-transported. The image is taken at a larger scale than in Figures 4.1 – 4. 3 and it is clear that the silica sand particles are larger than the stripped oil sand.

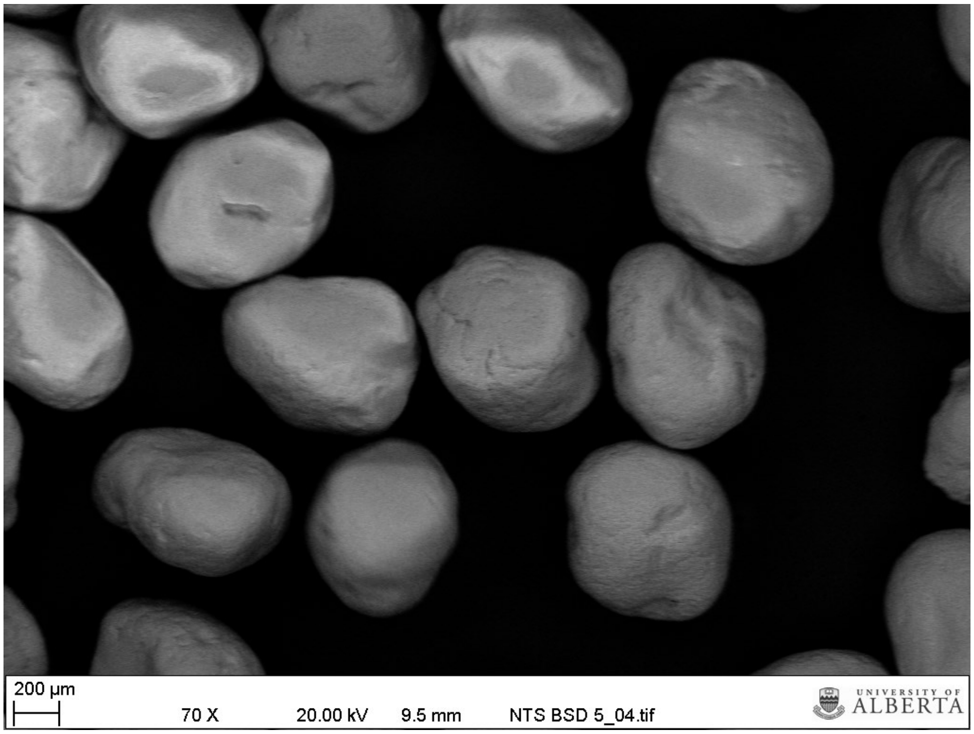

Figure 4.4 - Close-up image of rounded quartz grain abrasive. Magnification 70X

4.1.1 Stripped Oil Sand Particle Size Distribution

The oil sand material was dried to room temperature over the course of three weeks by being spread out over the floor. It was stirred and re-handled in order to ensure all portions of the material were sufficiently dried. Drying the sand in the oven creates the potential for over-drying which can result in the sand absorbing excess water moisture as it cools. Once the material was deemed suitable, a sieve analysis was performed. In order to decrease the amount of time needed to sieve through all the material, two nearly identical stacks of sieves were assembled. The sizing of the sieve meshes (in μm) was as follows: 250-212/208-180-150-106-75-Pan. The 208 and 212 μm sieves were the only sieves that were different sizes in the two stacks. It is important to note that all other sieve measurements remained the same, although two independent stacks were created in order to avoid confusion. Figure 4.5 below shows the particle size distribution of the tailings beach sand that included the 208 μm sieve plate. The grain size distribution with the 212 μm sieve can be found in Appendix B. No sieve analysis was performed on the rounded quartz grain sand, as it was assumed to be uniform in nature.

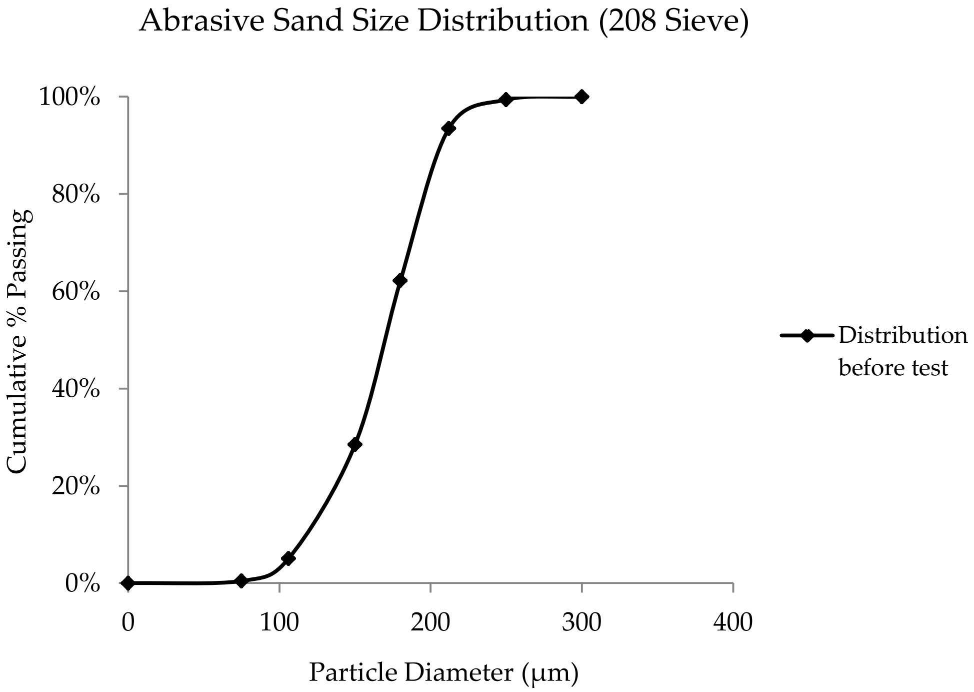

Figure 4.5 - Grain size distribution of tailings sand used in modified G65 test

4.1.2 Friction Angle

Lin (2013) showed that sand-metal wear will occur before sand-sand shear, due to the much higher internal friction angle of sand compared to sand-metal contact. A far greater force is needed to cause shear between two sand particles than to cause frictional wear between sand-metal interfaces.

4.2 Specimen Specifications

The test coupons in the modified test are wider than the standard setup, measuring 76 mm long by 63.5 mm by 8 mm thick compared to 76 mm long by 25 mm wide and 8 mm thick. The thickness of the test coupons is split between approximately 50% chrome carbide (CrC) overlay and 50% of 44W steel base plate. The Cr_7C_3 overlay was applied via Submerged Arc Welding (SAW) powder addition and the samples were cut in to the required shape using a water jet. A plasma cutter was investigated to cut the coupons but was found to be undesirable due to the possibility of the intense heat affecting the composition of the weld overlay. Water jetting also offered significantly neater and more accurate cut lines. The samples were then ground down using a surface grinder equipped with a diamond blade until there were no noticeable surface asperities.

The standard G65 test is set up to allow for the abrasion testing of any material form, including wrought metals, forgings, gas or electric weld deposits, plasma spray deposits, cermets, ceramics and so forth (ASTM G65, 1980(2010)). The ASTM standard also outlines that the specimen may be mechanically straightened or ground, with the only stipulation stating that the coupon be of appropriate size to develop an acceptable wear scar. In this regard, the coupons used in this test do not differ from any that could be used in a standard G65 test.

4.2.1 Coupon Preparation

The material that was tested in this thesis was supplied by Wilkinson Steel and Metals Inc. The chromium carbide overlay was applied via submerged arc weld on a 44W base steel. Chromium carbide is a material that is used frequently in oil sand operations to coat dipper teeth, ripper shanks, and crusher feed/discharge areas to prevent wear (Llewellyn, 1996).

Figure 4.6 - Sample coupon before surface grinding had taken place

When the overlay is applied, slag material builds up on the sample surface. In order to prepare the samples for testing, this material had to be removed by a diamond wheel surface grinder. Figure 4.6 above shows how the sample surface appeared before surface grinding took place.

The coupons were surface ground until there were no noticeable asperities, and all slag material had been removed. The test-ready coupons had a silver finish, and the only signs of deformities were small dark pits on one of the coupons. These pits are formed as a result of the welding process and are filled on-site in real-world applications. An example of the pits can be seen in Appendix C.

The transverse cracking observed below on the coupon surfaces results from the contraction of the weld as it cools; often called relief or check cracking (Fisher *et al.*, 2011). These are normal and are not an issue. Any sand particles caught in the cracks were vacuumed or blown out with air power.

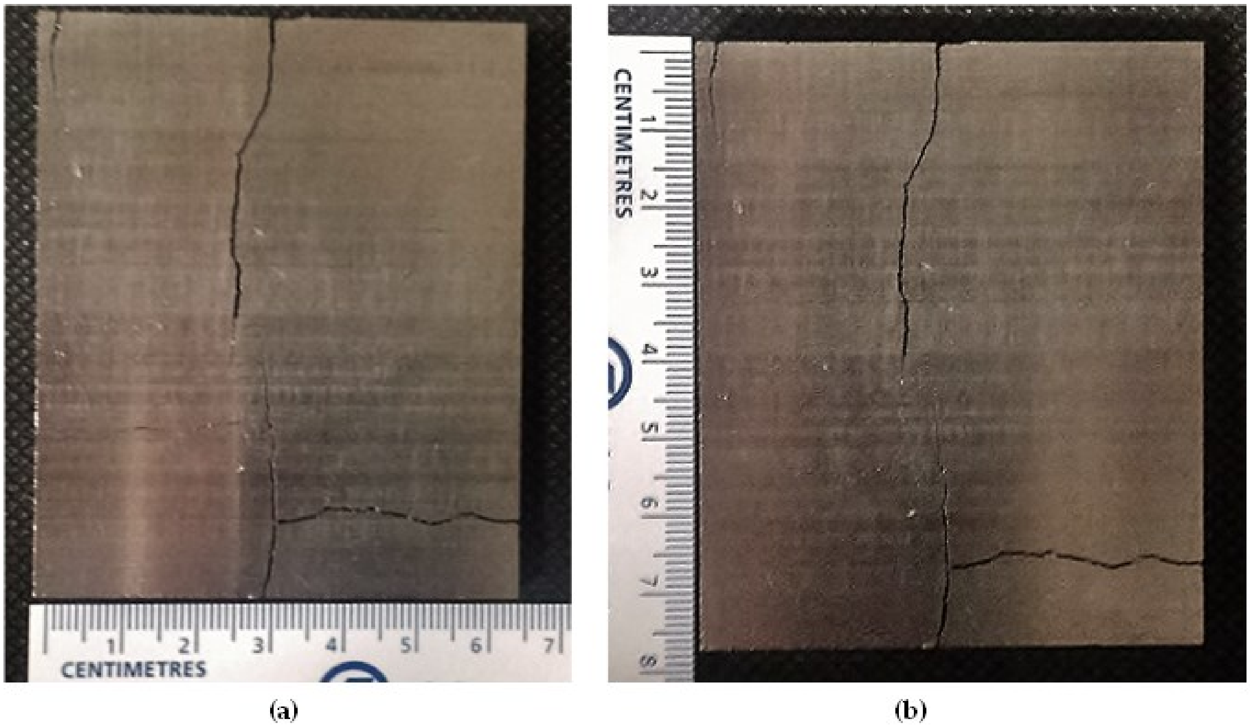

(a) (b)

Figure 4.7 - Sample coupon after surface grinding, ready for testing (a) width (b) length

Figure 4.8 details the side-view of the samples and the penetration of the Cr_7C_3 overlay applied via submerged arc weld. An additional side-view of the sample can be seen in Appendix C.

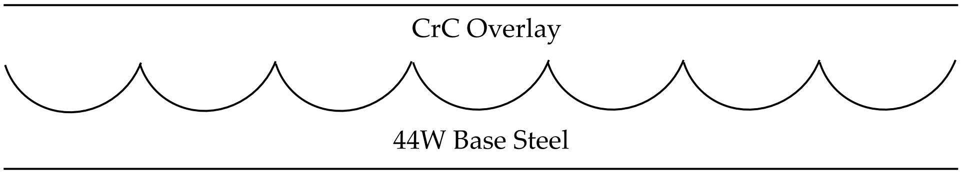

Figure 4.8 - Side-view of overlay deposit on base substrate

4.2.2 Submerged Arc Weld Parameters

The composition of typical chromium carbide based hardfacing alloys contains roughly 25 to 32 weight % chromium and up to 5% carbon. The microstructures generally contain large amounts of M_7C_3 carbides, where M represents a number of metals such as chromium, iron or manganese (Fisher *et al.*, 2011). The samples used in this thesis are hypo-eutectic Cr_7C_3 overlays containing an average of 28% chromium, 4% carbon, 2% manganese, 1% molybdenum & boron, and the remaining balance being iron. Although not all specific weld parameters and operating variables (such as the voltage & current levels, the travel speed, and the deposition rate) of the test samples are known, an estimation of the overlay density and hardness can be made. Figure 4.9 illustrates a basic analysis of a SAW process.

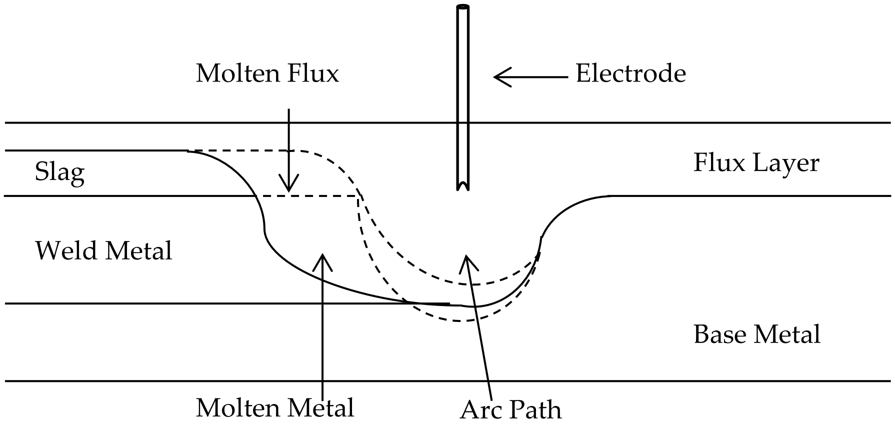

Figure 4.9 - General outline of the SAW process. Weld direction is left to right

Through the application of X-Ray powder diffraction techniques, the density of chromium carbide Cr_7C_3 has been calculated to 6.877 g/cm^3 (JCPDS Associateship, 1986). Using this density and applying pressure sintering techniques, the Vickers Hardness (converted to a GPa value) of Cr_7C_3 can range from 16 – 17 GPa (Hirota *et al.*, 2005). The H_V value of other chromium carbide compounds (Cr_3C_2 and $Cr_{23}C_6$) is reported to range from 10 – 18 GPa (Pierson, 1996). The carbide microstructure is usually aligned parallel to the heat flow direction of the weld deposition, and therefore roughly perpendicular to the substrate material surface.

Figure 4.10 is a SEM image of the surface of the coupon after it had been ground with the diamond surface grinder but before wear testing took place. The ridges that are visible are created from the diamond surface grinder. Figures 4.10 and 4.11 were taken in the exact same location on the surface of the sample coupon and at the same magnification. Figure 4.11 shows the carbides present beneath the coupon surface – represented by the darker grey patches. It is very evident that the carbides in the samples are deposited rather irregularly, and are more concentrated in some areas than others.

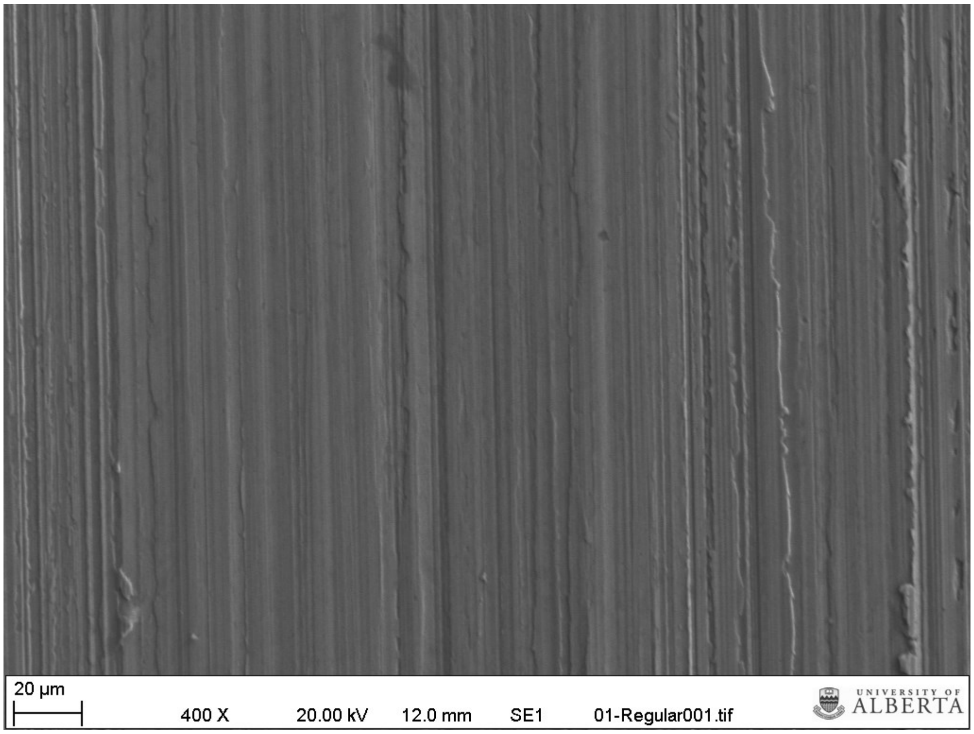

Figure 4.10 - Image of coupon surface prior to wear testing

Figure 4.11 - SEM image of carbides on a sample coupon. Carbides represented by darker grey shaded areas

The overlays on these samples are single-pass overlays; however they are often deposited in two passes. This is to account for dilution of the alloy with the base material, and to help facilitate growth of the acicular carbides that provide the wear resistance (Fisher *et al.*, 2011). Additional images of the coupons and cooling cracks can be seen in Appendix C.

4.3 Modified Testing Apparatus

4.3.1 Linear Actuator

The most significant addition to the standard G65 apparatus was the incorporation of a linear actuator. This actuator facilitates the repeatable load by varying its linear position. It was installed vertically at the end of a horizontal lever arm – similar to the standard apparatus where the weighted plates hang at one end. A simple moment diagram was constructed in order to determine the downward vertical force necessary to generate the scaled down normal resistive force.

The actuator position was controlled with a connected laptop that allowed for retraction and extension with simple mouse clicks. A load cell was installed between the end of the lever arm and the tip of the actuator cylinder. The load cell was connected to a secondary PC that recorded the variations in force when the actuator was extended and retracted. Thus the displacement of the actuator corresponded to a change in load that could be monitored and recorded. Test runs using scrap metal and the abrasive material were run in order to evaluate the system and calibrate it. A major component of the test runs was to determine the force values generated when the actuator was extended or retracted linearly. Another additional advantage of using the actuator is the ability to act as a rigid beam. In the traditional G65 system, weighted plates hang on the end of the lever arm and have a potential to bounce off of the spinning wheel, particularly at low weights. The actuator extends and retracts and holds the desired position acting as a rigid bar allowing for more accurate force readings. Some vibrations in the system still exist, due to the rotating wheel, however the vibrations are minor and are not substantial enough to cause significant fluctuations in the force values.

4.3.2 Wheel and Hopper

In order to maintain wheel velocity despite the fluctuating force, a 10:1 worm gear was installed to supply the drive motor with sufficient torque. The mounted rubber wheel is also different than a standard G65 test, having a diameter of 148 mm compared to the 228.6 mm steel disk/rubber sheath combo. Furthermore, the wheel used has a width of 51 mm compared to the standard width of 12.7 mm.

The wheel RPM was determined from the dig velocity of the dipper through the face. The velocity of the dipper from the moment it entered the face to when it exited was averaged over all nine cycles and found to be 0.775 m/s. Accounting for the radius of the wheel, the corresponding RPM value is equal to 100. This value remained constant throughout the test.

The final notable change to the standard test was the customized hopper. Although this does not have a significant effect on the results of the test, the larger hopper volume allows for fewer refills of material and easier access to dump material in. The flow rate of the abrasive was controlled with a valve such that the material flowed smoothly out of the nozzle in a fan that had the same width as the wheel. The nozzle opening was equal to approximately 1 mm, which is greater than three times the particle diameter which helps prevent clogging. The only aspect that needs continual attention is the collection of used material under the rubber wheel and replacing it back in to the hopper, a feature present in both the standard and modified setups.

The setup of the apparatus can be seen below in Figure 4.12:

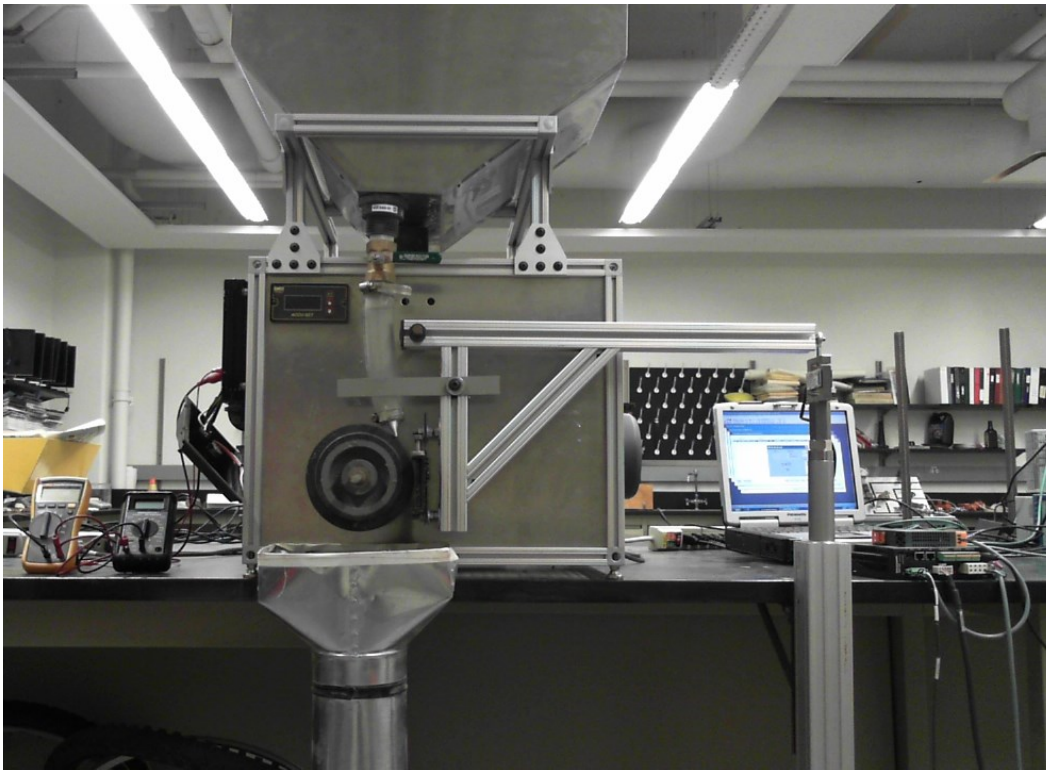

Figure 4.12 - Setup of the modified testing apparatus

4.4 Modified G65 Test Procedure

The procedure for the modified dry-sand rubber-wheel test is slightly more arduous and particular than the ASTM G65 procedure. Since the load is controlled with an actuator-PC setup, a number of steps take place before the actual wear testing begins. The following steps take place after the apparatus has been inspected and the PC hooked up to the actuator/stepper motor device. The actuator/motor should be checked by extending/retracting an appreciable distance but no so far as to reach maximum extension or contact the wheel. During these movements the load cell should be inspected to confirm that it is recording the variations in force. Stop the actuator in a location that easily allows access to the coupon holder to place the specimen.

4.4.1 Outline of Modified Test Sequence

The following list is based on the experiments performed in this thesis. Individual steps may differ slightly depending on the laboratory's capabilities. They are listed in sequential order.

- Clean the specimen with acetone, dry, and weigh to nearest 0.001 g (or with greater precision if possible)
- Place the specimen in the holder and retract actuator until approximately 110 N of vertical downward force is exerted to ensure specimen is perpendicular to wheel
- Securely tighten the specimen in the holder
- Extend actuator so no force is exerted. Coupon should be close to wheel but not touching. Note this position as the start position
- Close hopper valve and fill with abrasive media
- Set the desired wheel RPM, turn on motor and allow it to reach the desired speed
- Open the hopper valve and allow material to flow down through nozzle and over the wheel
- Extend actuator until coupon touches wheel. Record start time
- The extension process (moment coupon touches wheel to final position) should take 3 seconds for this test
- Hold at desired force value for 10 seconds
- Extend actuator (which retracts coupon) to original start position
- Wait 30 seconds to simulate shovel dump and re-position
- Simulate face re-engagement by retracting actuator in the same pattern as listed above to achieve desired force value.
- Repeat the extension-retraction process until desired cycle count is reached or lineal abrasion distance is attained
- Re-fill hopper with abrasive media if necessary
- Extend actuator so coupon is not touching wheel. Turn off wheel motor, close hopper valve
- Carefully remove specimen, allow it to cool if necessary, clean, and re-weigh with same precision
- Inspect wheel to check temperature
- With hopper valve closed, re-fill with abrasive
- Set up next iterative test run

4.4.2 Outline of Constant Load Test

For the constant load tests, the steps are: ensure the valve is closed and hopper is loaded; set a timer for the duration required to abrade 525 metres at the fixed wheel RPM; start the flow of abrasive and rotation of wheel; add hanging weight to end of lever which applies force and starts test. It would have been possible to do the constant load test with the actuator extended at a fixed position; however the standard G65 test uses a hanging dead weight. Therefore the amount of weight needed to apply the constant 130 N load was calculated and applied with lab plates.

4.5 Modified Test Parameters

The real world hoist force fluctuations happen too quickly and sporadically to be perfectly reproduced in the laboratory (see Hoist Force in Figure 3.8). However, a more accurate representation than the current ASTM G65 wear test can be achieved by adopting the varying force scenario outlined in Figure 4.13. The idea of the test was to increase the force in a "ramp up" period for approximately 3 seconds, and then level out for the next 10 seconds. The initial ramp up period mimics the forces experienced by the shovel as it begins engaging the face and hoisting upward.

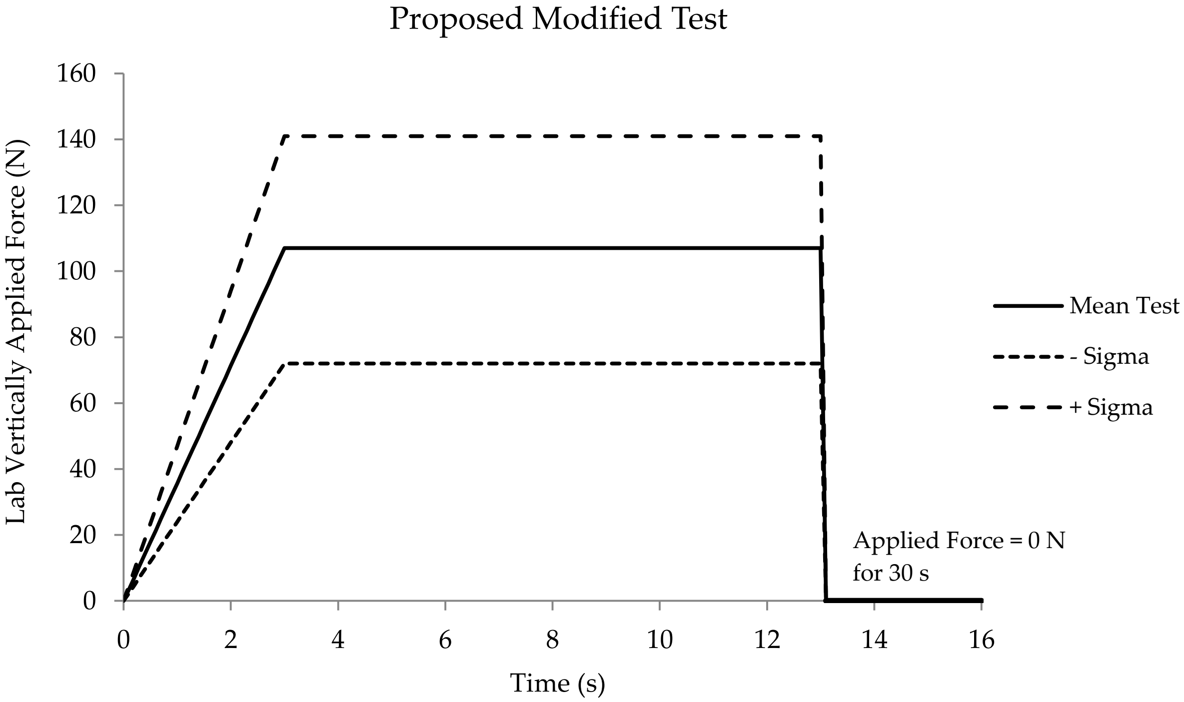

Figure 4.13 - Outline of proposed modified test

This steady increase in force shown in Figure 4.13 can also be seen in the first three seconds of Figure 3.8. As the shovel moves upward through the face, the force experienced still fluctuates but maintains a more or less constant horizontal trend. As the wheel spins, the apparatus experiences some vibrations; causing the constant force period to fluctuate in a sharp pattern similar to the data from the real world. The ramp-up sequence and fluctuation can be viewed in Figure 5.2.

Table 4.1 outlines the force values for the cyclical tests. The values for the field average peak normal force and standard deviation are listed in Table 3.1. The lab normal force is related to the field normal force through the cube root scaling method and the scaling factor of 16. The exerted lab force is obtained by dividing the lab normal force by the lever arm factor 2.82. The three difference peak lab normal forces stem from scaling the field average peak normal force as well as the values plus and minus one standard deviation from the field mean.

Table 4.1 - Field and lab force categories for the three cyclical test variations

		Test	
	$-\sigma$	Mean	$+\sigma$
Avg. Peak Field Normal (kN)	828	1231	1634
Avg. Peak Lab Normal (N)	202	301	399
Lab Exerted (N)	72	107	141

Table 4.2 below details the test matrix comparison between the standard G65 test and the modified G65 test performed in this thesis. The test parameters of the modified test are not required to be the values listed below, but rather whatever parameters suit the conditions of the field scenario that is being tested.

Table 4.2 - Test matrix comparing modified and standard G65 tests

Test	Force Applied	Test Material	Specimen Dimensions	Abrasive Material	Distance Abraded	Apparatus Requisites	Other Parameters
Modified G65 Test	Adjustable. 202 – 399 N range is used here	Any material form. Smooth, flat finish is recommended	Modifiable. 76 x 63 x 8 mm used in this test	Adaptable. Crushed particles < 1 mm preferred	Variable. Reflect real-world conditions	Force-varying instrument. Match nozzle to abrasive size	Wheel speed reflects data. 100 RPM = 0.775 m/s here
ASTM G65 Test	Value G65 Procedure dependant 45 or 130 N	Any material form. Material may determine specimen size	Rectangle. 25 x 76 x *t* mm, where 3.2<*t*<12.7	Rounded quartz grain sand (Silica sand)	Procedure dependant. 71.8 – 4309 metres	See ASTM G65 schematic. Durometer A-60 rubber wheel	Wheel speed is 200 RPM. Sand flow is 300-400 g/min

The most important variations between the standard test and modified test completed here are the forces induced on the sample coupon, the abrasive media used, speed of the rotating wheel, and the total lineal abrasion distance. The evaluation of Cr_7C_3 overlay as the testing material was specific to the goals of this thesis and is not outside the realm of the regular G65 test. The dimensions of the rubber wheel were not taken from the ASTM spec sheet; however the hardness of the rubber wheel was within the ASTM G65 standards.

In order to validate any data against similar tests performed by other individuals, results from both the modified G65 and standard G65 tests are reported as volume losses. This ensures there is no confusion caused by any variations in material densities (ASTM G65, 1980(2010)). Any other test parameters were taken directly from the ASTM G65 test outline and applied to the modified test.

5 EXPERIMENTAL RESULTS

The implementation of the linear actuator successfully recreated a more realistic load pattern for an electric shovel digging through a face than a standard G65 test does. The actuator was controlled easily to mimic the 3 second ramp up period, followed by a more accurate portrayal of real world digging conditions for 10 seconds. The speed of retraction and extension could be manipulated such that upon completion of the 13 second digging cycle, the force between the actuator and wheel could be removed nearly instantaneously for 30 seconds. This break simulated the shovel swinging, dumping, and returning to the face.

5.1 Load Varying Capability

A major aspect of the results was seeing the potential of taking real world load data and using it as input to a modified G65 wear test. Figure 5.1 shows a complete 50 cycle load sequence on a test coupon. This particular test aimed at representing the average peak normal force experienced by the shovel teeth; corresponding to 1231 kN in the field and scaled down to 301 N in the lab (labelled Desired Mean). The transient start and finish of the loading cycle was not included in calculating the average peak force. The Actual Mean line represents the laboratory average peak normal force.

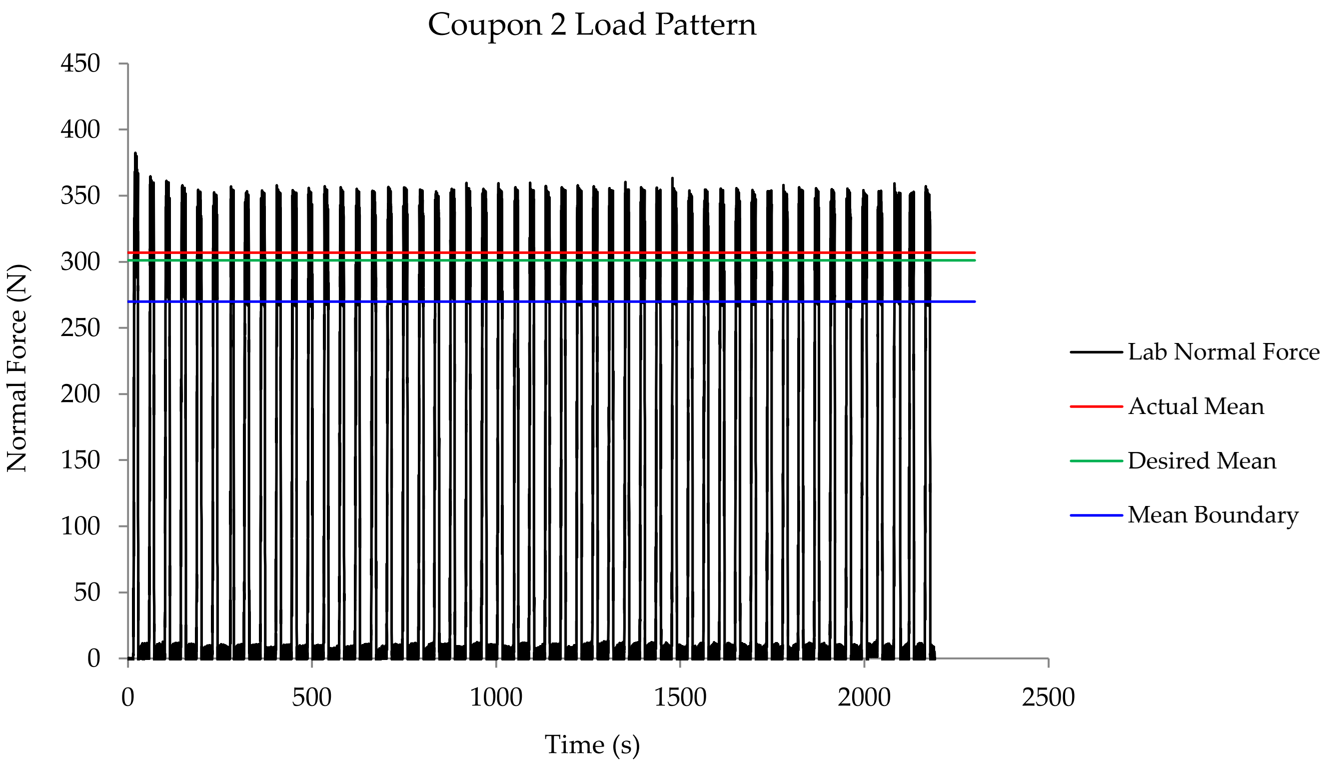

Figure 5.1 - Cyclic load pattern on sample coupon

The Mean Boundary line represents the minimum values used in calculating the Actual Mean of the thick, darker sections of the graph. These banded areas correlate to the continuous 10 second portion of a dig cycle that takes place once the ramp-up period is complete. In order to determine the value of the Mean Boundary line, the lab results were graphed and a line was marked based off of where the minimums were located during the active wear test. That is, a line was traced at the troughs of the recorded lab data points and every value above this trough was used in calculating the average peak normal force exerted in the lab. For the data depicted in Figure 5.1, the Mean Boundary value used was 270 N. In the coupon 2 test, the Actual Mean was calculated to be 307 N, with the Desired Mean being equal to 301 N. This is a 2 % variation, indicating that the modified apparatus had sufficient capabilities in mimicking the desired applied force scenarios.

In order to get a better understanding of the ramp-up and continuous dig portions, Figure 5.2 below is a close up view of two cyclic loading cycles from the coupon # 2 test pattern.

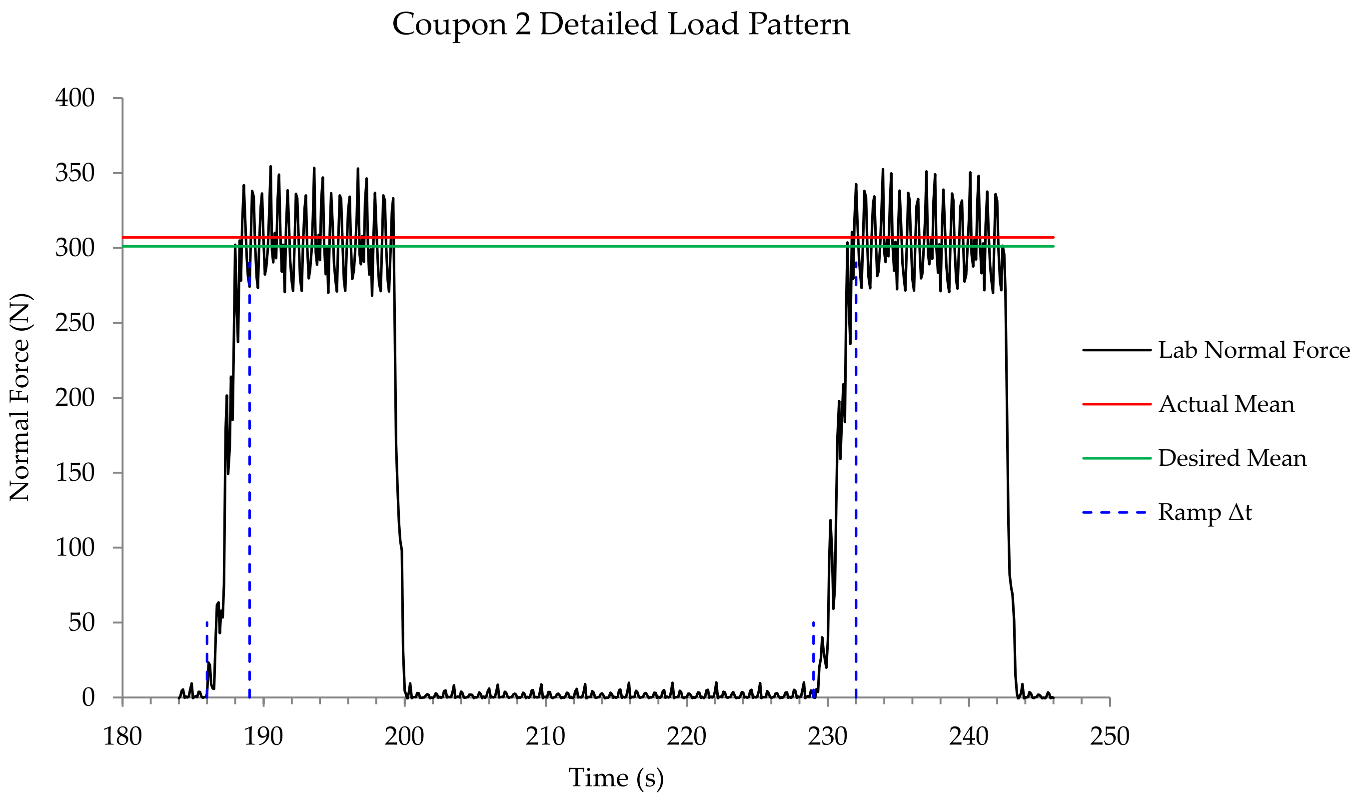

Figure 5.2 - Two cycles showing 3 second ramp up period and constant force

The dashed blue lines in Figure 5.2 show that the ramp up period was 3 seconds. This is recreated in all 50 cycles on all 9 samples. The ramp up value was determined graphically from analyzing the field data and averaging each dig cycle's ramp period. Figure 3.8 shows how hoist force and resistive force change throughout the dig cycle and similar graphs were created for the other dig cycles. The 30 second reprieve between dig cycles was achieved by extending the actuator upwards so no force was exerted on the coupon.

5.2 Coupon Volume Loss

5.2.1 Variably Loaded Coupons

The coupons were subjected to 525 meters of lineal abrasion distance. Approximately 505 m of abrasion distance was due to the 50 load cycles, and the remaining 20 m from the preliminary engagement of the coupon to ensure the desired force values would be obtained. Table 5.1 shows the initial and final masses of each coupon, as well as the corresponding volume loss when the density of the chromium carbide overlay (6.877 g/cm^3) is accounted for.

Table 5.1 - Data after 525 m of lineal abrasion at various normal loads

Coupon #	Normal Force (N)	Applied Force (N)	Pre-test Mass (g)	Post-test Mass (g)	Mass Loss (g)	Volume Loss (mm^3)
1	301	310	297.7845	297.7589	0.0256	3.72
2	301	307	311.0322	310.9789	0.0533	7.75
3	301	309	312.8373	312.8083	0.0290	4.22
4	399	401	316.0063	315.9714	0.0349	5.07
5	399	407	306.3137	306.2686	0.0451	6.56
6	399	408	307.9218	307.8859	0.0359	5.22
7	202	204	318.2482	318.2261	0.0221	3.21
8	202	186	317.5261	317.5051	0.0210	3.05
9	202	196	318.7909	318.7681	0.0228	3.32

The Normal Force column represents the ideal desired force created between the coupon and rotating wheel. The Applied Force is the average peak force that was applied during the 10 second constant bands for each coupon over all 50 cycles. The difference between the two columns stems from the ability to displace the actuator accurately enough to achieve the desired force. The maximum Applied and Normal force discrepancies are represented by coupon # 1, a +2.8 % difference, and coupon # 8 with a -7.9 % difference.

From Table 5.1, it is evident that the samples' volume loss is dependent on the normal force applied. The exceptions are coupon # 2 and coupon # 5 which showcase more volume loss than would be expected in their respective force categories. Figures 5.3 & 5.4 below are detailed SEM images of the wear scar from one of the variably loaded coupons. The two images are taken in the identical location, and the darker grey spots in the second image are the carbide particles beneath the surface. Careful comparison between the two images shows that the carbides correspond to peaks on the surface topography whereas the white matrix material corresponds to troughs. This is because the carbides are harder and more wear resistant than the matrix material surrounding them. As the coupons are abraded, the carbide particles are exposed.

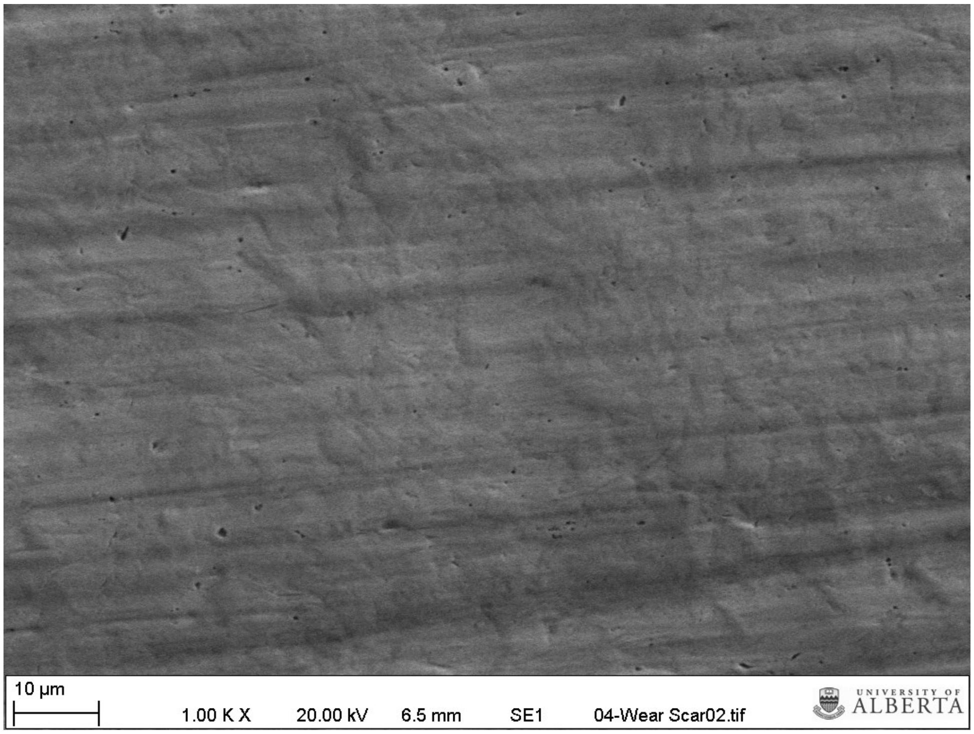

Figure 5.3 - Image taken at centre of wear scar. Wear direction is right to left

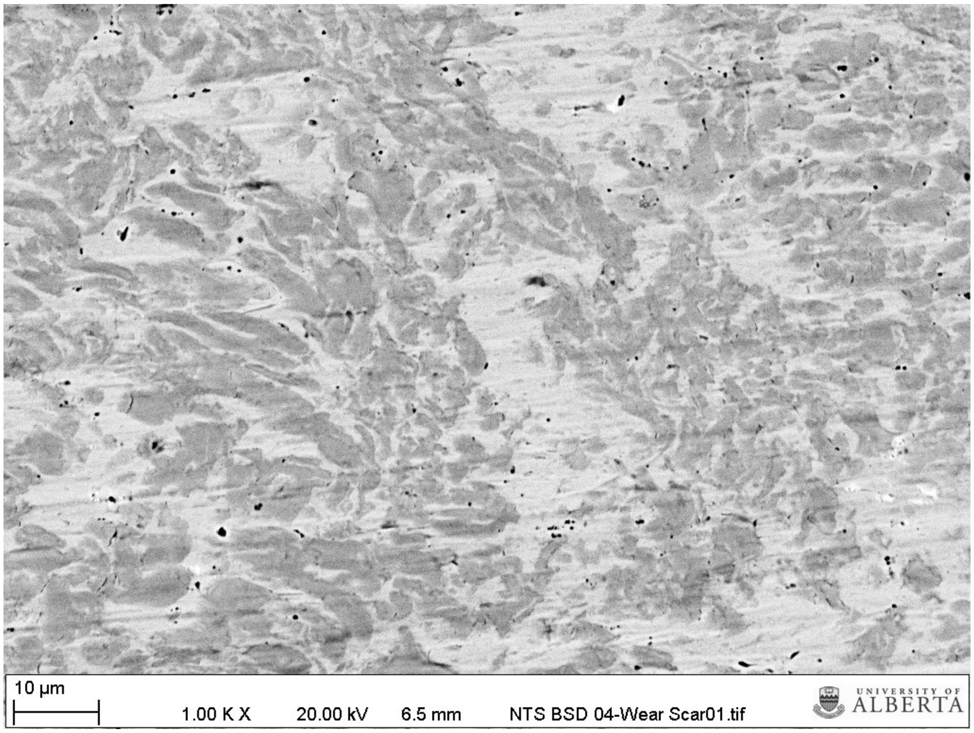

Figure 5.4 - Image at same location as Figure 5.3 – dark grey shapes represents carbides

Comparing the volume loss to the normal force exerted on the coupon-wheel interface, there is a general trend that an increase in force results in an increase in volume loss. This is shown below in Figure 5.5:

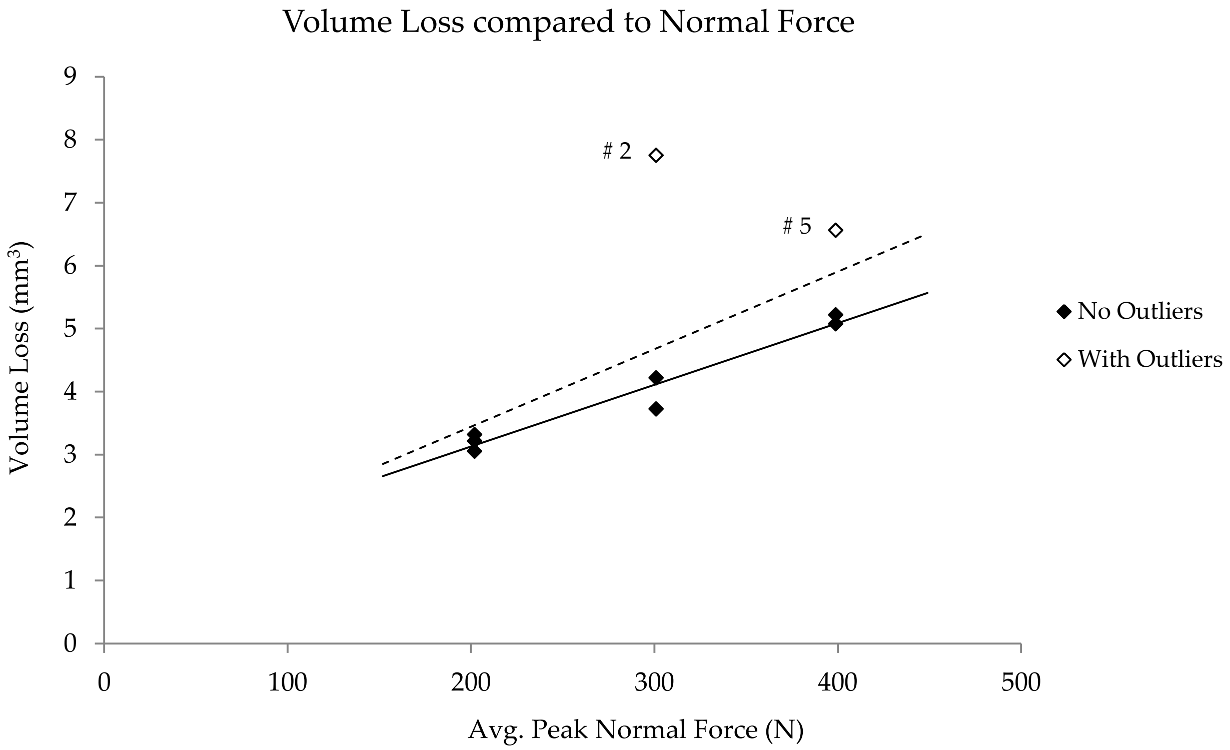

Figure 5.5 - Comparison of total volume loss with normal force on coupon

The solid black trend line represents the more correlated test values, and has a coefficient of determination (R-squared) value of 0.95. The dashed red trend line is generated from including the two major outliers, coupon # 2 (at 301 N) and coupon # 5 (at 399 N). Including the two outlier data points decreases the R-squared value to 0.42, a significant drop. By excluding only coupon # 2, the R-squared value becomes 0.83. A possible explanation of the outlying values could be a more significant loss of matrix material in coupons # 2 & 5.

5.2.2 Constantly Loaded Coupons

Comparing the volume losses reported in Table 5.1 with the two coupons re-tested under constant load conditions shows interesting results. Although the total abrasion distance remained the same at 525 metres, the normal force exerted in the constant load tests matched ASTM G65 specifications of 130 N. The other notable difference was that the abrasive media in the constant load tests was rounded quartz grain sand, versus the bitumen stripped oil sand in the cyclical tests. Table 5.2 summarizes the average wear losses experienced for each force category in the cyclic test and tabulates the average volume loss between the two constantly loaded coupons.

Table 5.2 - Comparison of average volume loss between cyclic and constant load tests

	Material Tested	# of test Specimens	Avg. Peak Normal Force (N)	Abrasion Distance (m)	Volume Loss (mm^3)
Cyclically Loaded	Tested Cr_7C_3 Overlay	3	202	525	3.19 ± 0.11
		3	301	525	5.23 ± 1.79
		3	399	525	5.62 ± 0.67
Constantly Loaded	Re-surfaced Cr_7C_3 Overlay	2	130	525	3.29 ± 0.21

The resurface coupons were ground down with the diamond wheel surface grinder until no evidence of a previous wear scar existed. No contact was made with the substrate material.

5.3 Power Draw & Abrasion Energy

It is now of interest to investigate the energy required to facilitate the volume losses measured from shovel teeth from the field and the sample coupons tested in the laboratory. As the shovel dipper moves upward through the face the hoist forces increase significantly. With this increase in hoist force there is also an increase in power draw from the shovel's two hoist motors. The power draw from the raw data was graphed in a similar fashion to the hoist force, and the energy for each dig cycle was calculated by determining the area under the power-time curve.

5.3.1 Field Data Power Draw

Before the energy calculation could be performed, a "carry-load" amount had to be subtracted from the field data power-time graph. This amount is the power required to hold out the empty dipper and handle horizontally at full extension (i.e. no movement through the face). Therefore, this power does not contribute to the wearing process of the shovel teeth. From the power-time curves and for the purpose of this thesis, the value was taken to be 150 kW. Figure 5.6 shows the power-time graphs of the first three field dig cycles.

The red lines indicate the area under the power-time curve that was used to calculate the abrasion energy exerted in each dig cycle. The energy was calculated for each individual dig cycle, as not all of the field dig scenarios were identical. The initial boundary of the abrasion energy was taken to be the moment the dipper engaged the face. The horizontal top boundary of the energy calculations was obtained from averaging the power required once the continual upward digging motion had been established. The point at which the dipper exited the face was determined using the hoist force vs. time graphs, and the time stamp from this data point was used in the energy calculations. Additional power-time graphs can be found in Appendix E.

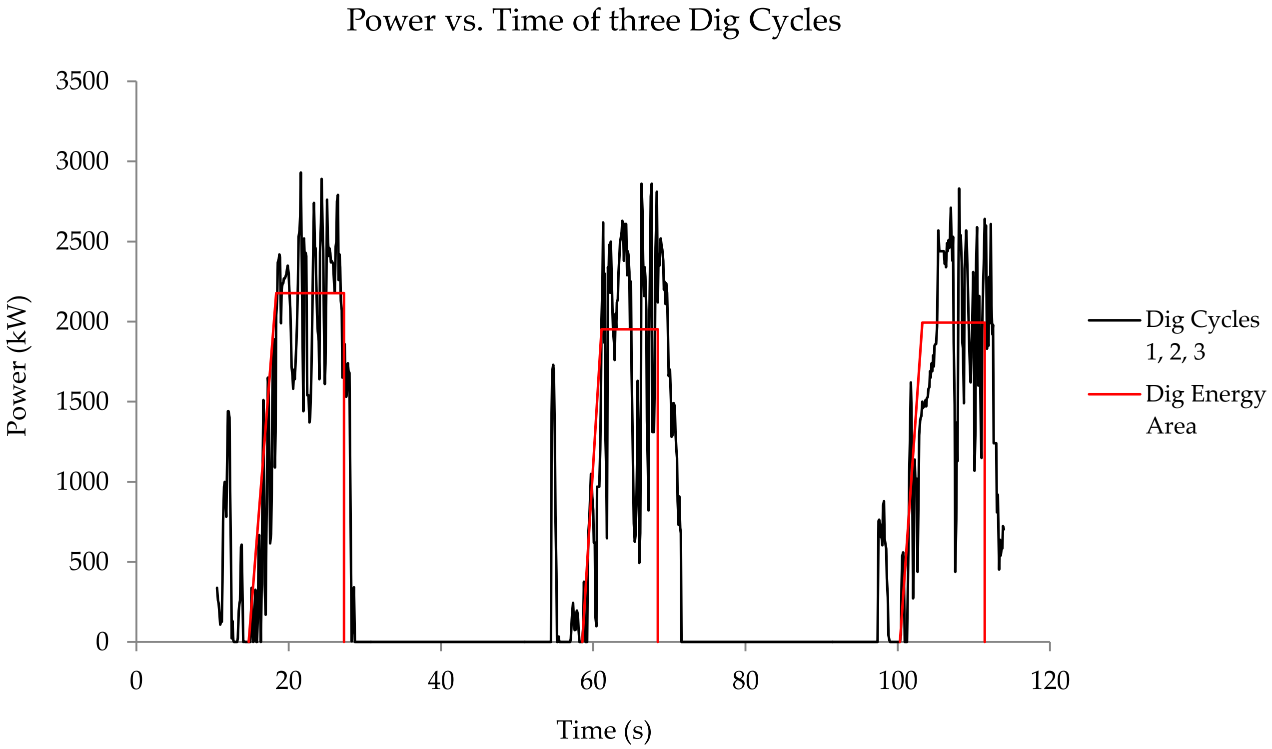

Figure 5.6 - Graphs of power draw during typical dig cycles

5.3.2 Modified Apparatus Power Draw

The power draw from the modified apparatus was determined by connecting a voltmeter and ammeter to the wheel speed control panel and measuring the voltage and current values. The values were recorded by hand and tabulated in Excel™. Since the wheel continued to spin when there was no force applied, the difference in voltage and amps required during resistance and during no resistance was used in the power calculations. Three different charts were generated, as there were three separate force categories. The graph of the median force category, the normal force being 301 N, is shown in Figure 5.7. The other two charts from the modified tests can be seen in Appendix E.

For the supplementary constant load tests using G65 abrasive and normal force, the values were recorded but a chart is not included. The shape of the chart is identical to Figures 5.7 and those shown in Appendix E; however the magnitude is less than even the lowest force category, as the normal force applied was less. The average differential power and energy causing abrasion from the constant load tests is shown in Table 5.3. The energy values for the laboratory tests reported in Table 5.3 are the values that caused the measured volume loss; that is, they are calculated from the power used per abrasion cycle, multiplied by the cycle time, and the number of cycles. For the repeatable load tests, there were 50 cycles. The constant load tests had one long cycle.

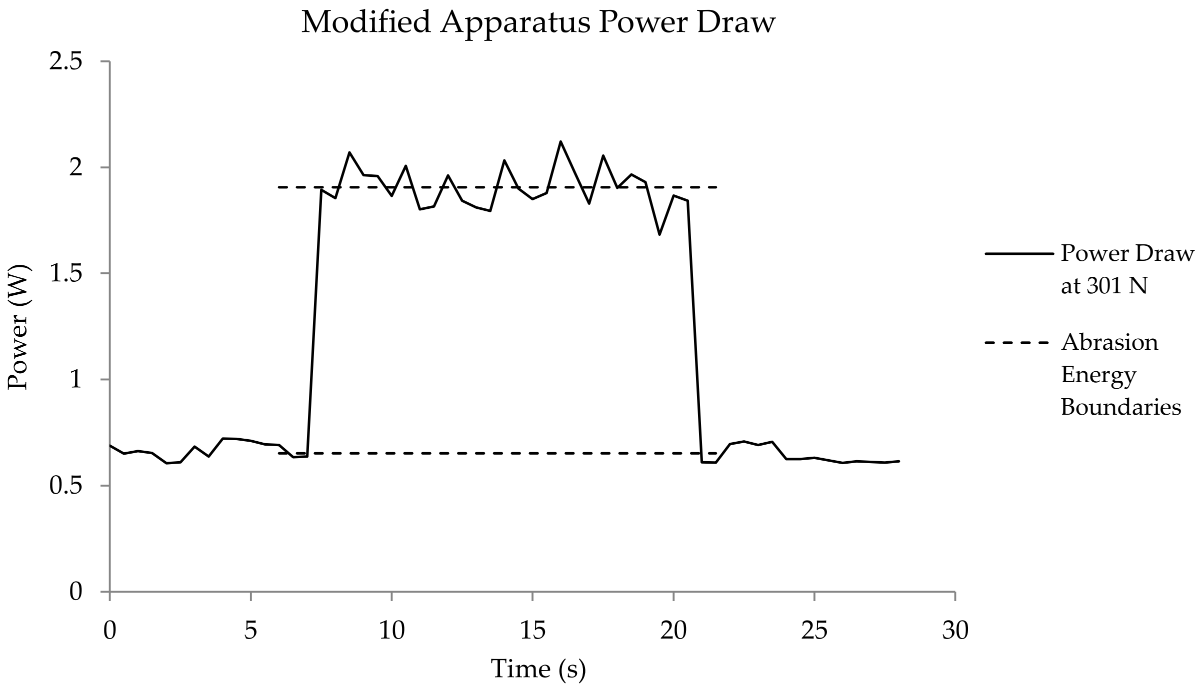

Figure 5.7 - Power Draw of Modified Apparatus at 301 N Normal Force

Rather than calculating the total area under the curve to determine the Energy, the area was taken to be the space between the two horizontal dotted lines. This represents the differential power required throughout the abrasion process (per cycle) rather than the power to rotate the wheel with no normal force applied. The top horizontal line represents the average power draw throughout the abrasion process, with the lower line being the average power needed to just spin the wheel. The total length of the power draw calculation was taken to be 13 seconds, as simulated by the test parameters of the 3 second ramp and 10 second dig.

5.3.3 Comparison of Field and Lab Data

Below are the results of the power draw from the raw data and modified test. The raw data values are the averages of all 9 dig cycles. The cyclic load values correspond to the three categories of lab normal forces that are listed in Table 4.1. The power values for the lab tests are differential power; the power that caused abrasion (per cycle). Energy is calculated from these magnitudes.

Table 5.3 - Comparison of Power and Energy values per field and test cycle

	Avg. Peak Normal Force (N)	Avg. Power Draw (W)	Avg. Abrasion Energy (J)
Field Data	1 231 000	1 738 169	20 434 482
	202	0.81	527
Cyclic Loads	301	1.25	815
	399	1.70	1107
Constant Load	130	0.27	182

5.4 Prediction of Field Wear

In this thesis, specific energy, or energy density, refers to the amount of energy in a certain volume of material (Marinescu *et al.*, 2004). Using specific energy (energy per unit volume) to predict the replacement time of teeth in the field has been attempted before by Lin (2013). The process used in Section 5.4.4 builds on Lin's work and aims to correlate the wear experienced in the lab to values measured from used shovel teeth.

5.4.1 Field Specific Energy

The values for material loss from field teeth come from new and used shovel teeth measured in the laboratory. One tooth was located in a central position on the dipper and was in service for 8 hours, displaying moderate wear. A second tooth located on an edge position was in service for 18 hours and was severely worn. Table 5.4 below summarizes the recorded mass values, and their corresponding time in the field. The volume losses were calculated based on the density of mild steel being 7850 kg/m^3.

Table 5.4 - Mass and Volume Loss data for field shovel teeth

	New unused tooth	Moderate use (8 hours)	Substantial use (18 hours)
Mass (kg)	95.7	81.1	59.2
Volume Loss (m^3)	-	0.00186	0.00465

Although the precise energy values that caused these wear measurements are undeterminable, reasonable values can be obtained by analyzing the available raw data. Table 5.3 reports the average energy expended per cycle as the dipper moves through the mining face. This energy must be multiplied by a constant A_{TP} that represents a tooth-area proportion. This constant is the ratio of one tooth's area over the entire area of the 9 dipper teeth, adapters and dipper lip that engages the face. The area of a single tooth is reported in Section 3.4.2; the total area of all 9 teeth, 9 adapters and lip shroud is calculated using measurements of the field adapters found in the lab and the specified bucket volume. The total engaged area value is equal to 2.6 m^2.

The approximate number of cycles the shovel completed within the specified time frame that facilitated the volume losses in Table 5.4 must also be determined. This is found by Equation 5-1, and involves the availability and utilization of the shovel. Considering the amount of wear visible on both teeth described in Table 5.4, it is sensible to conclude that the shovel was operating nearly continuously throughout the two wear periods. This results in higher availability and utilization values, taken to be 0.92 and 0.8, respectively.

$$\# \, of \; cycles = \frac{TF * 3600}{T_c} * A' * U' \tag{5-1}$$

Where *TF* is the time frame (either 8 hours or 18 hours), T_c is the time to complete one full dig cycle, and A' & U' are availability and utilization, respectively. Considering the average energy expended per cycle in the field, E_{Avg}, the field specific energy (converted to GPa) using the raw data is then found with Equation 5-2:

$$E_{Sf} = \frac{E_{Avg} * A_{TP} * \# \, of \; cycles}{1{,}000{,}000{,}000 * V_{Lf}} \tag{5-2}$$

5.4.2 Lab Specific Energy

Section 5.3 showed that the energy that resulted in the measured volume losses was determined from the differential power draw during the abrasion process. E_L represents the laboratory abrasion energy, per cycle. As with the field data, the energy values reported in Table 5.3 were multiplied by the number of cycles the coupon experienced. The number of cycles performed in the repeatable loading tests was 50 for all samples. The volume losses of each coupon are reported in Table 5.1. Determining the lab specific energies at each force value was done by simply dividing the lab energy expended (in Joules) by the average coupon volume loss (in mm^3), yielding GPa.

$$E_{Sl} = \frac{E_L * \# \, of \; test \; cycles}{V_L} \tag{5-3}$$

5.4.3 Comparing Specific Energies

The calculated values are reported in Table 5.5 below:

Table 5.5 - Energy per unit volume, Field vs. Lab

	Avg. Peak Normal Force (N)	Specific Energy E_s (GPa)
Field Data	1 231 000	234 / 211
	202	165
Cyclic Loads	301	156
	399	197
Constant Load	130	55

The two different specific energy results for the field data correspond to the 8 hr and 18 hr time frames, respectively. The lab specific energy values are lower than the calculated field values in all categories. The lab E_S value for the 301 N test is lower than expected due to the increased volume loss shown by coupon # 2 in Figure 5.5. If the coupon yielded less volume loss, the E_S value would be higher and therefore more representative of the increasing pattern.

5.4.4 Determining Tooth Life in the Field

The ability to predict when a tooth needs to be changed has significant implications. Equation 5-4 below yields the predicted time a shovel tooth would last under normal digging conditions in the Athabasca oil sands environment.

$$T = \frac{E_{Sl}}{E_{Fc}} * V_{Lf} * T_c * \frac{1\ hr}{3600\ s} \tag{5-4}$$

Where T is the predicted time, in hours, a shovel tooth would last in the field, and E_{Fc} is the field energy experienced per cycle, per tooth. E_{Fc} is calculated with Equation 5-5:

$$E_{Fc} = \frac{E_{Avg} * A_{Tp} * A' * U'}{1{,}000{,}000{,}000} \tag{5-5}$$

Using Equations 5-3 thru 5-5 allows for the calculation of the predicted tooth life in hours. The magnitude of E_{Sl} will vary depending what normal force value was used to calculate it. Similarly, the value of V_{Lf} will change depending on if the calculation is being performed for the 8 or 18 hour volume loss period. The values in Table 5.6 are for an availability and utilization of 0.92 & 0.8 only.

Table 5.6 - Tooth life prediction

	Avg. Peak	Field Tooth Life Prediction (hrs)	
	Normal Force (N)	8 Hour Comparison	18 Hour Comparison
Cyclical Load Tests	202	5.64	14.09
	301	5.33	13.31
	399	6.74	16.84
Constant Load Tests	130	1.89	4.73

Appendix F contains additional Tables which show the predicted hourly lifetime of a tooth with a range of availability and utilization values.

5.5 Examination of Surface Wear Scar

Two coupons were tested using parameters similar to the standard G65 test in order to further evaluate the application of a varying load instrument. The two coupons were re-finished using the diamond wheel surface grinder such that there was no evidence of a previous wear scar. Neither the wear scars generated by the modified test nor the re-finishing process on the chromium carbide overlay dug sufficiently deep into the coupon to penetrate the substrate. Optical and SEM micrographs were taken to investigate the cyclic and constant load wear scars on a smaller scale to try and better understand the processes that created them.

5.5.1 Standard Test Incorporating Dipper Velocity and Modified Distance

This test was performed exactly as the test described in the ASTM G65, however the wheel was set to rotate at the same rate as the modified test (100 RPM) and the total lineal abrasion distance was modified. This rotation speed was calculated based on the average digging velocity experienced by the shovel teeth as the dipper moves through a face. Rounded quartz grain sand was used as the abrasive, and the lineal abrasion distance matched the modified test at 525 metres. Table 5.7 below shows the test parameters and volume loss measured from the two additionally tested coupons:

Table 5.7 - Coupon volume losses from supplementary test

Coupon #	Normal Force (N)	Pre-test Mass (g)	Post-test Mass (g)	Mass Loss (g)	Volume Loss (mm^3)
8*	130	306.4591	306.4379	0.0212	3.08
9*	130	305.2808	305.2567	0.0241	3.50

*Indicates that the samples were re-finished using the surface grinder

Comparing the volume losses of coupons 8 & 9 from the modified test results in Table 5.2, the values reported in Table 5.7 are quite similar. The total abrasion distance and time of the two tests are identical, but the normal force and abrasive used are not. In the modified test, coupons 8 & 9 were tested in the lowest force category which exerts a normal force 55 % higher than the normal force applied in the standard G65 test.

5.5.2 Investigation of Wear Scar

Optical and SEM micrographs were taken of the cross-section and centre of the wear scar of coupons # 8 & 3. The SEM images of the modified test wear scar are not from the same coupon shown in Figures 5.3 & 5.4. The goal of the imaging was to determine if the varied load induced wear via different mechanism than a constant load.

In order to take cross-sectional images, the samples were cut into shape using a wet saw and were sonic cleaned using acetone and rinsed with methanol. The cross section samples were prepared in a powder moulding compound and were polished with increasing grit sandpaper up to a maximum of 1200 grit. Final polishing was done with 3 μm polycrystalline diamond suspension.

Optical images were taken of the two cross sections once polishing was complete. The samples were etched with a 40 ml H_2O; 20 ml HNO_3; 10 ml HCl; 5 g $FeCl_3$ solution. SEM images were taken of both the cross-section and surface-face of the wear scars. The SEM images shown below were obtained using a different microscope than the previous images shown in Sections 4.2.2 and 5.2, and the surface-face images were taken as-is; that is to say they were not prepared differently than the SEM images shown in previous sections, and were not subjected to the polishing or etching routine that the cross-sections samples were. Further optical and SEM images can be found in Appendix C.

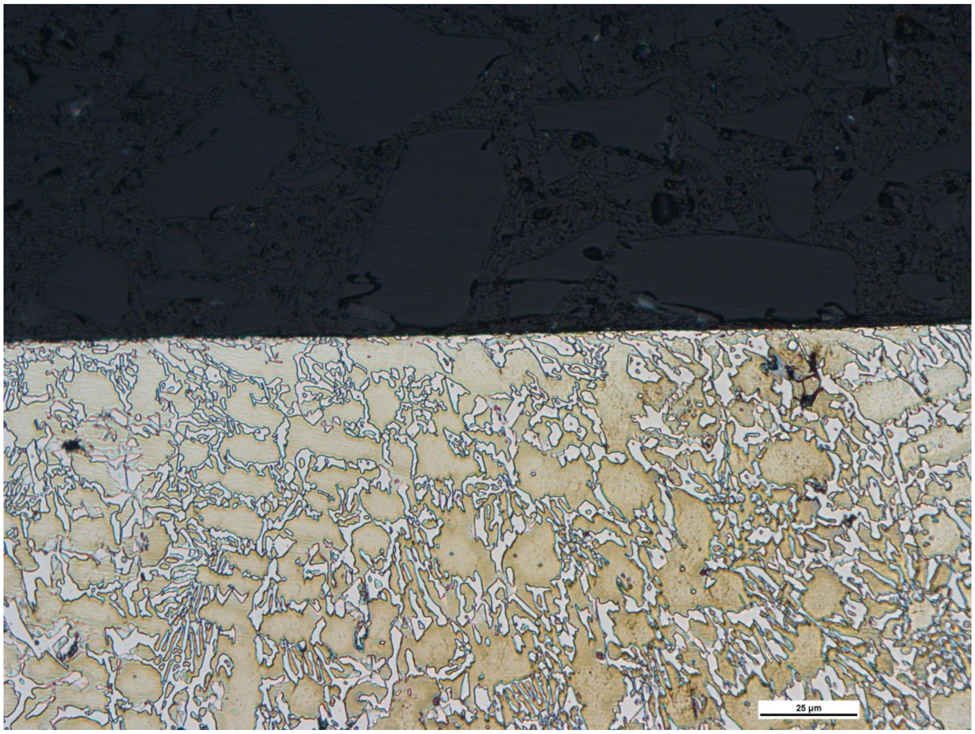

Figure 5.8 - Optical microscope image of the constant load cross-section

Abrasive direction is out of the page. Note the white arrows pointing to the more frequent and deeper grooves on the varied load image. The images are taken at the same scale, shown at 25 μm.

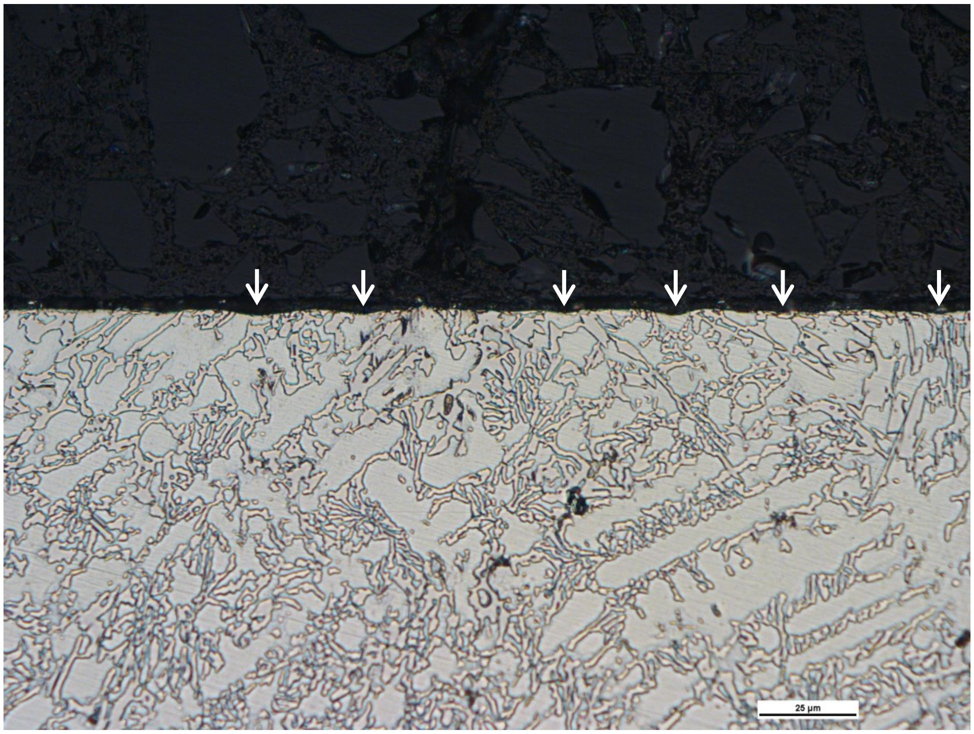

Figure 5.9 - Optical microscope image of the varied load cross-section

The SEM cross-section images show the grooves are deeper on the varied load coupons. The groove shown in Figure 5.10 was one of the deepest grooves on the constant load coupons.

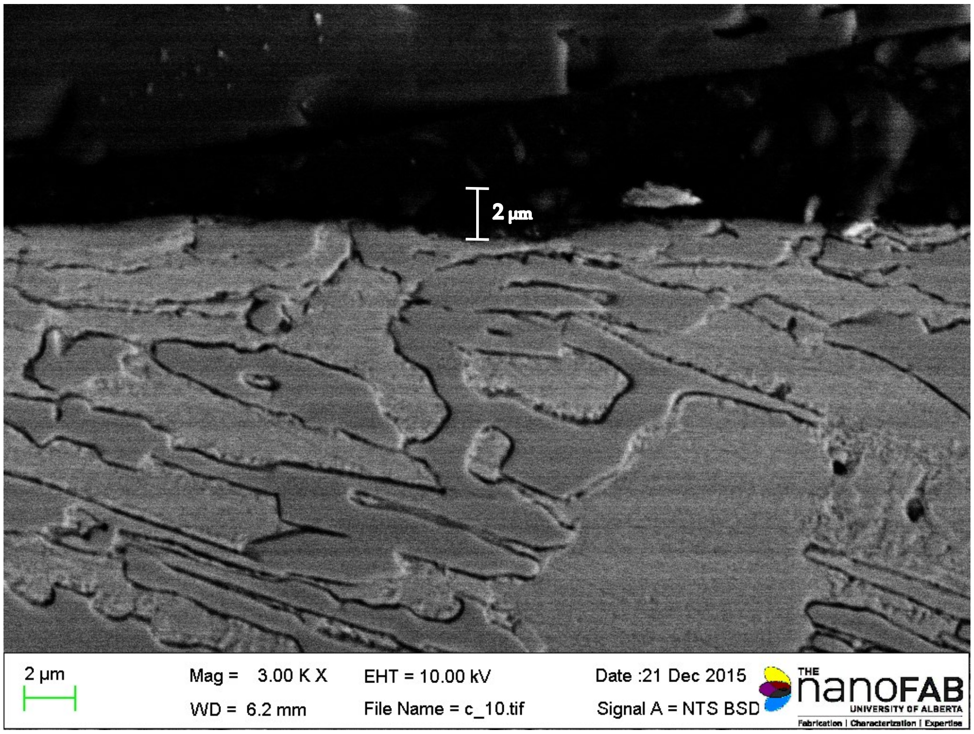

Figure 5.10 - SEM image of the constant load cross-section

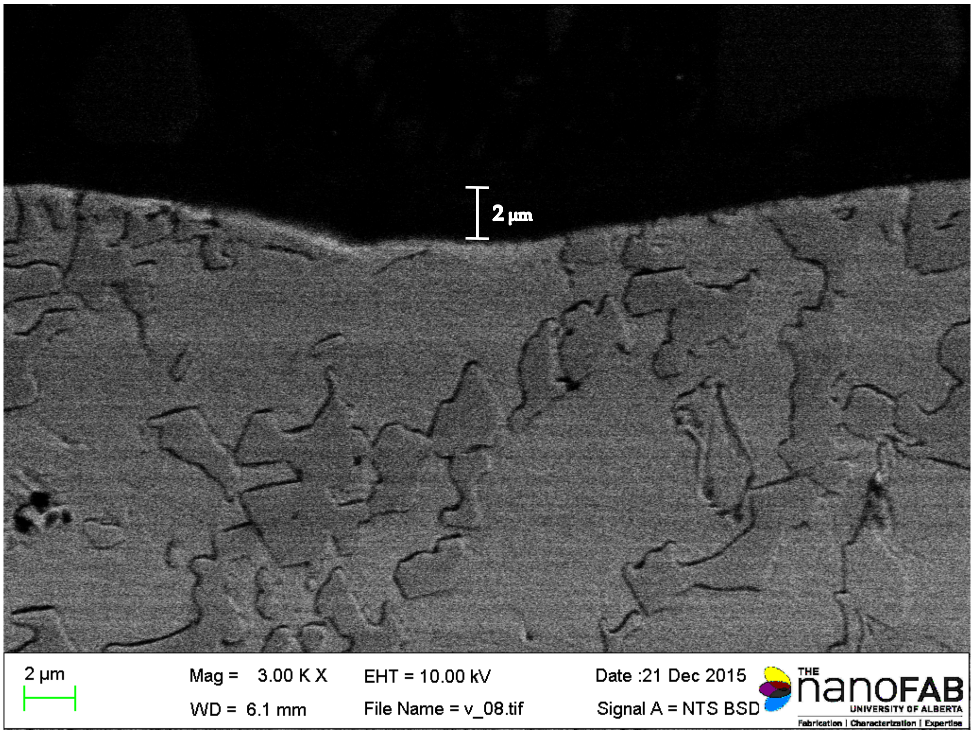

Figure 5.11 - SEM image of the varied load cross-section

6 DISCUSSION

Wear testing performed in the laboratory is a quick and inexpensive way to evaluate wear based on a set of parameters and field conditions. Typical laboratory abrasive wear tests approximate two and three-body abrasion (Hawk *et al.*, 1999). Regardless of how accurate and effective a laboratory wear test setup may be, raw field data will always be the best measure of a material's performance. In saying that, modifications can be made to existing wear tests to allow them to more accurately reflect the real-world conditions. Specific to this thesis, the ASTM G65 Dry-Sand Rubber-Wheel test can be adapted to more suitably represent the conditions experienced by the ultra-class electric shovels throughout the excavating process.

6.1 Raw Force Data Input

The goal of implementing the linear actuator was to investigate the viability of varying a force load to more accurately represent field conditions. The ability to do that was demonstrated during the experiments performed. Rather than exerting a constant force over a predetermined time, an actuator was used to increase the force at a desired rate until a calculated, scaled value was reached. The ability to repeatedly do this indicates strong potential to develop a wear test that can use field data as the input data directly, rather than simply applying a constant load.

In reality, the hoist force data collected fluctuates greatly and sporadically, perhaps at a rate that is too sensitive for meaningful tests, yet the ability to vary forces at all improves the representation of the real wear conditions. The major fluctuations brought upon by extreme outlying values seen in the data – such as zeros or exceedingly high force spikes – are more likely anomalies than true representative values.

Combining an actuator and the functionality of programming applies to more than the shovels digging in the Athabasca oil sands. With programs such as MATLAB or LabVIEW, it is possible to reduce the difference seen between the "Normal Force" and "Applied Force" columns in Table 5.1 even further. Hardly ever in the mining environment are moving pieces of equipment under a constant force for an extended period of time. As an alternative example, dozer ripper shanks experience more or less force depending on speed, ground penetration, and numerous other parameters describing the interaction between the shank and the ground. Linkages, wire ropes or other areas where ore and rock can become trapped represent other instances where forces can change over time yielding a more complicated scenario than a standard G65 test can portray.

An additional criticism of the existing G65 test is the coupon's susceptibility to bouncing off of the spinning wheel, due to the weights hanging at the end of the lever arm, preventing it from acting as a rigid bar. The actuator provides a much more stable resistance than the hanging free weights.

6.2 Coupon Wear

6.2.1 Volume Loss

The amount of volume loss was minimal for all coupons, as expected. Chromium carbide is a hard weld overlay and is used in abrasive wear resistance. Since not all weld parameters were known, the density of the overlay was determined by citing several different sources. Furthermore, the exact Vickers hardness of the overlay was also not determined, but reasonable estimates can be made, again based off reading literature.

There were two instances when the amount of wear volume experienced was quite different than the other values in the respective force categories. The greater volume loss experienced by coupons # 2 & # 5 are possibly due to the prevalence of pits on each coupon's surface. However, other coupons that were tested also had pits and did not experience any abnormally large volume losses.

An alternative explanation of the increased wear observed on the two coupons could be the distribution of carbides. It is possible the two coupons were cut from the edge of the sample plate, and therefore had a poorer distribution of the carbide particles that are resistant to wear. The lack of carbides results in an abundance of the softer matrix material. It is possible that the excess matrix material washed out and no real carbide exposure occurred. Any smaller carbide particles that were present in the vicinity could have been pulled free along with the weaker matrix compound. The values are without a doubt irregular compared to the other tested coupons. It is reasonable to believe that with a larger number of test samples and a wider range of test forces exerted, the linear trend displayed by the solid black trend line in Figure 5.5 would be a very representative prediction for the amount of volume loss expected. The black trend line in the Figure is a representation of the pattern of volume increase that seemed most likely; that is, it excludes the two major outlier values of coupon # 2 and # 5.

There is a lack of information regarding wear testing on chromium carbide overlays, specifically the amount of material lost. The ASTM G65 reports some minor volume loss for "No. 14 hard-chrome plating" using Procedure C but does not elaborate any further on the specifications of that plating. The volume losses of the coupons tested in this thesis were higher than the values reported on the ASTM standard, as they were subjected to higher forces and a larger lineal abrasion distance.

The constant load tests produced volume losses that were similar to the losses experienced by the coupons that were tested cyclically in the lowest average peak force category. The constant load was only two-thirds of the lowest repeatable load, but still resulted in appreciable volume loss. It is not expected that using re-finished coupons affected the amount of worn material, as neither the wear scars from the modified test nor the re-grinding done with the surface grinder wore through the weld overlay.

6.2.2 Wear Scars

The wear scars generated from the apparatus appeared as smooth, shiny rectangles that had a very minor depression, if any, from the original coupon surface. This was expected as the Cr_7C_3 overlays are quite hard and the amount of time each coupon was abraded was not sufficient enough to cause a major depression.

6.2.2.1 Cyclic Load

Visual inspection of the wear scar shows the grooves or pathways the particles took as they were dragged across the coupon surface. From a general inspection standpoint, it appears that the wear mode was a microcutting action, although the variably loaded coupons have the potential to be susceptible to fatigue wear as well.

Figures 5.3 & 5.4 are SEM images from a wear scar, taken at the same location. Figure 5.3 is taken using a secondary electron mode; Figure 5.4 is taking using a backscatter technique, which provides the means to observe the carbide particles. Comparing the two images, one can discern that the carbide particles match closely with peaks and ridges in Figure 5.3, whereas the lighter grey matrix material corresponds to the troughs and dips. This shows the matrix material is worn down faster, and in the process exposes fresh carbides. Although some troughs and ridges are visible upon inspection, there are no instances where carbide particles can be seen protruding from the wear scar surface. This implies that even though the matrix material wears down faster (as it is softer) the carbide particles also seem to be wearing down at a relatively constant rate.

6.2.2.2 Constant Load

Viewing the constant load wear scars with the unaided eye hints that a different wearing process may be taking place compared to the variably loaded coupons. The grooves formed from the abrasive are not as deep as the repeatable load scenario perhaps implying a particle rolling movement rather than sliding, as the abrasive is rounder in shape.

The cross-section profile of the constantly loaded wear scar is much flatter than the variably loaded coupon. This directly relates to the lack of visible grooves on the surface. The abrasive particles do not seem to impinge upon the coupon surface as much as the variably loaded coupons, despite force being constantly applied.

6.3 Power and Energy

6.3.1 Field Data

Energy values were calculated using the power draw for both the raw data and lab experiments. From the raw field data, all 9 dig cycles were graphed as power vs. time. In order to represent the power required to lift and hold an empty, extended dipper, a constant carry-load value was subtracted from each of the recorded power data points. This value had to be accounted for, as the power needed to support an empty extended dipper is always necessary, and therefore would not contribute to the energy causing abrasion. The value of the carry-load was determined graphically to be 150 kW.

With the carry-load subtracted, the energy for each individual cycle could be determined by calculating the area under the power-time curve. As each cycle was not identical, the areas computed were unique for each case. The resulting 9 cycle average was used in any subsequent calculations.

6.3.2 Lab Tests

Similar to the field data, the area under the power-time curves at each force interval represented the energy required to exert that force. However, since the wheel was constantly spinning, a differential power was calculated between when resistance was applied and when the wheel was able to spin freely. This differential power multiplied by the time it was applied yielded the abrasion energy per cycle. It was assumed that the entirety of this energy difference was transferred to the friction energy causing the abrasion. The total energy that caused the measured volume loss in the cyclic load tests was the energy per cycle multiplied by the number of cycles, 50. The constant load abrasion energy was found by multiplying the differential power by the duration of the test.

6.4 Field Wear Prediction

The ability to generate accurate field wear predictions with cheap, repeatable laboratory tests is very desirable across a number of industries. Wear in mining, like wear in many other circumstances, is very dependent on the specific conditions in which it is occurring. This prevents the ability to use a single, standard test and apply it to a particular scenario. Even within certain scenarios, such as surface mining in the Athabasca oil sands, wear rates can vary significantly depending on the material being excavated (overburden vs. oil sand) or the current season. Colder temperatures result in more consolidated faces; certain pits or overburden layers may be more quartz-rich than others which can drastically affect the rate of wear. In the experiments performed in this thesis, the goal was not to discover a relationship that could be universally applied to all oil sands operations, but to evaluate how a modified G65 wear test performed when using real world, scaled down shovel data.

A shovel's availability and utilization changes frequently and the values of its availability and utilization depend on the time frame the shovel is considered in. Generally, using a 365 day datum, the shovel will be available and utilized roughly 64 % of the time ($A' = 0.8$, $U' = 0.8$). However, over the short 8 and 18 hour periods that the field teeth investigated in this thesis were subjected to, the shovel should be available at a much higher percentage. For this reason, availability and utilization were chosen as 0.92 and 0.8, respectively. The availability value corresponds directly with the standard one hour break a shovel operator is permitted over a 12 hour shift. This equates to 40 minutes of break over 8 hours, and 90 minutes of break over the 18 hours of operation. In some instances an assistant operator is available to continue shovel operations while the main operator is on break.

As Table 5.6 shows, the prediction method employed in this thesis used in conjunction with the cyclic load tests marginally underestimated the amount of time the teeth would last in the field. The constantly loaded test produced significantly different results, as the energy expended over the total abrasion cycle was smaller in magnitude than any of the repeatable tests. If the constant load test was run for a standard G65 abrasion distance, thereby drastically increasing the total expended abrasion energy, it would not necessarily be able to improve its prediction of the field wear rate, as the volume loss experienced would correspondingly increase as well. In the author's opinion, the aspect of cyclic loading greatly improves the ability to predict field wear rates.

6.5 Contrast of Cyclic and Constant Loading Wear Scars

There are no procedures outlined in the standard G65 test that report an abrasion distance that is reasonably close to the length abraded in the modified test. Therefore, comparing volume loss or wear scars between the two tests could be skewed because of significant differences in total abrasion distance. For this reason, the total lineal abrasion distance used when performing the constant load test was set to the same value as the modified test. In this regard, it was not a true ASTM G65 test that was performed, but the test provided a means to do a comparable analysis of the standard and modified abrasion tests. The two sample coupons that were chosen for the constant load test were coupons # 8 & 9. Both coupons were in the lowest applied force category for the modified test, and therefore should have the smallest and least severe wear scars. The samples were completely re-finished with the surface grinder such that the wear face was as smooth and unblemished as before the modified tests had begun. None of the modified tests, in any force category, produced wear scars deep enough to come close to penetrating through the weld overlay.

6.5.1 Volume Loss

The similarity of the volume losses shown by the constant load and the lowest average peak force category of the cyclically loaded tests is interesting. The constant load tests on coupons 8 & 9 using rounded quartz grain sand abrasive resulted in the test coupons warming significantly. The cyclically loaded tests did not heat the coupon or wheel up any noticeable amount. Constant load tests generate much more heat energy – a possible contributor to sample volume loss. Visual analysis of the SEM abrasive images in Section 4.1 shows that the stripped oil sand has more angularity whereas the silica sand has larger particle diameters. The two abrasives should have similar hardness values, as the main component of both silica sand and oil sands is quartz.

In the additional SEM images featured in Appendix C, the surface of the wear scar on the variably loaded coupon showcases a location where significant damage has occurred, something that was not visible anywhere on the wear scars of the constantly loaded coupons. Both the optical and SEM images show that the repeated loading created deeper, more frequent wear grooves than the constant load did, a possible consequence of introducing a fatigue damage component.

6.5.2 Possibility of Fatigue Wear

Rabinowicz (1965) described fatigue wear as a relation between the stresses in the contacting materials and the number of cycles required to produce fracture. The cyclic loading performed in the modified test has the potential to introduce a fatigue damage component. Although the grooves observed in the SEM images are created from two different abrasives and two different force loads, the prevalence and severity of the grooves on the variably loaded coupons could speak towards fatigue as being a possible candidate as an additional wear mechanism induced by cyclic loading.

In the additional coupon images shown in Appendix C, the optical microscope shows that the constantly loaded coupon has a noticeable flatter cross-section compared to the variably loaded coupon. The groove depth appears to be related to the type of loading each coupon experienced. The deeper grooves are found exclusively on the cyclically load coupons, and can even be viewed under careful inspection with the naked eye.

The SEM images of the wear scar surface show marked contrast in the behaviour of the carbides. In the constant loading case, the carbides can be seen protruding from the surface. Their rod-like forms are visible and do not appear to have been broken off. Instead, the matrix material around them shows the effects of abrasion, which is not unusual or surprising. The micrographs of the cyclic loading condition, however, do not show any protruding carbides. Instead, it appears the deep grooves are formed throughout the wear scar. It is hard to determine how the carbides are worn in the cyclic loading case, but one possible scenario is the carbides are successively broken down into smaller and smaller pieces before being completely removed by the flow of abrasive.

A final difference between the two wear scars is the presence of what appears to be spalling in the centre of one of the variably loaded coupons. Appendix C shows two images of the pit-like shape where a chunk of the chromium carbide overlay has been completely torn away from the coupon surface. This was not seen anywhere on the constantly loaded coupons, and may be an additional indicator of fatigue damage inflicted by the cyclic loading cycles.

6.6 Test Adaptability

Overall, the implementation of a linear actuator allowed for easy variation of the force exerted and a much more accurate representation of a shovel digging through a face. This modification has the potential to allow for more accurate testing of other low-stress, three body abrasive wear conditions experienced in the mining industry such as in linkages, pivot pins and wire ropes. Substituting in other abrasive substances creates the ability to input raw data from shovels digging in hard rock mines or other ground materials other than the oil sand tested here.

6.7 Issues Encountered

There were no major issues encountered during testing of the coupons. Ensuring that the hopper stays full of abrasive can require lifting a heavy load up over shoulder height. This risk can be reduced if the lab where the test is performed allows for a lower height test set up.

While the test is running, keeping an accurate count of the number of cycles can be tedious, but as long as the test operator is aware this is not a major issue. If additional programming is used to control the actuator, perhaps a count function can be incorporated to automatically stop actuator movement after the cycle count has been reached.

Determining the displacement needed to apply the desired force was found by applying force on the coupon (i.e. retracting the actuator which lowered the lever arm) until the load cell reading was outputting the required values. The step count of the actuator was then noted, and the actuator was extended until no force was exerted on the coupon. The difference in the number of steps between the count at the desired force value and the step count with no force applied equals the number of steps the actuator needed to move to reapply the desired force. The step count was then divided by a whole number (in the range of 93-97 steps) which yielded a value detailing the amount of moves the actuator had to make. Reproducing the same force every cycle for 50 cycles was achieved by manually directing the actuator to retract or extend the calculated number of moves, with each move being a displacement of the 93-97 steps.

Since the actuator was moved the same amount of times each cycle, and each move corresponded to a certain number of steps, the actuator was displaced an identical amount each cycle. This process was easily timed and repeated, as demonstrated by the consistency of the load charts in Appendix D. Between the three force categories, the amount of displacement varied with the higher force loads requiring more displacement.

Ideally, a program can be incorporated to move the actuator without any manual involvement the required distance. This was not possible with the interface included with the instrument, as there was no looping function available to control the movements. It is possible that programs such as MATLAB or LabVIEW could be used in addition to the provided interface to further automate the system.

A final criticism of the experiment is the changing contact area with increased force. At the higher force categories (301 N, 399 N) the wheel was squished more against the coupon surface, creating slightly larger wear scars than the 202 N of applied force created. This is to be expected, as more normal force will cause the wheel to flatten in the vertical direction resulting in wear scars that are taller, but not any wider, in dimension.

7 CONCLUSIONS AND RECOMMENDATIONS

7.1 Conclusion

Wear is a complicated phenomenon that occurs in many forms at all stages of mineral extraction. Ground engaging tools operating at the Athabasca oil sand deposits in Northern Alberta are subjected to primarily abrasive wear. Oil sand is extremely abrasive containing a high percentage of quartz, a hard naturally occurring mineral. Some sources indicate that the economic cost of the wear attacks can surpass $1 billion annually, resulting from maintenance, replacement parts, and loss of production. Research has been done into reducing wear rates, and some progress has been made using techniques such as surface engineering that incorporate weld overlays on the base tooth material. These overlays come in the form of chromium and tungsten carbide, and can significantly improve abrasive wear resistance. Ultra-class mining shovels operate at a scale that is too large and costly to continually conduct field tests investigating wear. Laboratory tests offer a fast, economic, and reproducible way to investigate wear rates and advances in abrasion resistance.

The current standard G65 test is one of the most widely used abrasion tests worldwide. It is relatively easy to set up, and does not require a specialized skill set to perform. However, a major disadvantage of the G65 is the inability to modify the force load over time. A continuous force over a set period of time is not very indicative of abrasive wear scenarios in the mining industry. Instead, forces fluctuate over time and can increase or decrease depending on digging conditions and the operating environment. Creating a system where forces could be modified to more accurately reflect real-world operating conditions would be a considerable improvement to the existing system.

The implementation of a linear actuator and a load cell allowed for scaled down field force values to be used in an abrasive wear test on chromium carbide overlay coupons. Raw data was analyzed and resolved to reflect the forces experienced at the tip of an ultra-class shovel tooth, and scaled to magnitudes that could be applied in a laboratory setting. This allowed for the development of a modified test, where the applied force pattern could be controlled to simulate a shovel bucket moving through a face. An initial ramp-up period was observed in the field data and was successfully recreated in the lab.

The lab results were used to predict wear in the field based off of two real-world worn shovel teeth. The method employed marginally underestimated how long field teeth would last, but still showed promise considering only a small number of samples were tested and the exact wear conditions of said field teeth were not known. The results are indicative enough of the measured field wear to justify improving the standard G65 test to a version that has the ability to apply a range of forces, as well as the constant force the current test outlines. The installation of the actuator not only allows for more accurate representations of wear circumstances where the abrasive force can fluctuate, but also provides a more stable constant force than weights hanging on the end of the lever would. The constant load tests produced volume losses in the range of the modified tests performed, but this did not translate to tooth-life predicting abilities when correlated with field data. The author believes it is essential to modify the out-dated standard G65 test with one that is more flexible to accommodate a variety of wear conditions with more accuracy.

Although additional tests need to be performed to increase statistical confidence, evidence was presented that shows the wear scar varies between constant loading and cyclical loading wear scenarios. Significant differences in the scar cross-section profile and the wear surface were observed between the two loading set-ups, and the process causing damage is potentially acting very differently. The total volume loss of the coupons between the two loading cycles was very similar, contrary to what would be expected when examining SEM images of the wear scars.

7.2 Recommendations

One significant improvement that can be made to the existing modified system is to incorporate a third party program (such as LabVIEW) to move the actuator the desired amount at the specified time intervals with no human involvement. Ideally, a cycle counter could also be incorporated that would stop the test once the desired number of cycles had been attained. The only requirements of the experimenter would then be to ensure continual flow of abrasive from the nozzle and to maintain an acceptable level of abrasive material in the hopper.

Second, supplementary tests could be performed on each coupon to investigate how the wear rate changes over time. Although neither the wheel or test coupon got hot during the tests performed, it is imperative that the wheel and coupons are permitted to sufficiently cool before running consecutive tests. In addition to these tests, experiments can be run that compare different loading cycles while using the same abrasive. This can allow for direct comparison of the loading properties. It is paramount to keep other variables such as linear wheel velocity and total abrasion distance equal, however.

If the wear environment of interest is not the oil sands, the test can be performed with other crushed abrasive media; provided the media is smaller than 1 mm. This allows for the investigation of wear processes on shovels operating in hard rock environments to be completed with more confidence.

Finally, as additional programming could be used to control variations in force, the same methodology could be applied to the rate of the rotating wheel. Dig velocity is not constant through the face; future works could investigate the consequences of changing the speed of the wheel during the abrasive process to further mimic the real-world conditions.

8 WORKS CITED

Anderson, M., Chiovelli, S., & Llewellyn, R. (2003). The Use of Tungsten Carbide Materials for Oilsand Wear Applications. *International thermal spray conference* (pp. 509-518). Orlando: ASM International.

ASTM G105. (2002(2007)). *Standard Test Method for Conducting Wet Sand/Rubber Wheel Abrasion Tests.* West Conshohocken: ASTM International.

ASTM G65. (1980(2010)). *Standard Test Method for Measuring Abrasion Using the Dry Sand/Rubber Wheel Apparatus.* West Conshohocken: ASTM International.

ASTM G81. (1997(2013)). *Standard Test Method for Jaw Crusher Gouging Abrasion Test.* West Conshohocken: ASTM International.

Blouin, S., Hemami, A., & Lipsett, M. (2001). Review of Resistive Force Models for Earthmoving Processes. *Journal of Aerospace Engineering, XIV*(3), 102-111.

Bond, F. C. (1964). Lab Equipment and Tests Help Predict Metal Consumption in Crushing and Grinding. *Engineering Mining Journal, 165*, 169-175.

Bott, R. D. (2011, November). Canada's Oil Sands. (3rd). (D. M. Carson, Ed.) Calgary, Alberta, Canada.

Carrigy, M. A. (1966). *Lithology of the Athabasca Oil Sands.* Edmonton: Research Council of Alberta.

Centre, O. S. (N.D.). *Facts about Alberta's oil sands and its industry.* Fort McMurray: Government of Alberta.

Daneshmend, L. K., Hendricks, C., Wu, H., & Scoble, M. (1993). Design of a mining shovel simulator. In W. F. Bawden, & J. F. Archibald (Eds.), *Innovative Mine Design for the 21st century. Proceedings of the International Congress on Mine Design* (pp. 533-538). Rotterdam, Netherlands: A.A. Balkema.

Denker, J. S. (2015). *Introduction to Scaling Laws*. Retrieved from av8n Web site: http://www.av8n.com/physics/scaling.htm. Accessed July 15, 2015

Dusseault, M. B., & Morgenstern, N. R. (1978, May). Shear Strength of Athabasca Oil Sands. *Canadian Geotechnical Journal, XV*(2), pp. 216-238.

Eyre, T. S. (1978). The mechanisms of wear. *Tribology International, XI*(2), 91-96.

Fisher, G., Wolfe, T., Yarmuch, M., Gerlich, A., & Mendez, P. (2011). *The Use of Protective Weld Overlays in Oil Sands Mining.* Edmonton: University of Alberta.

Frimpong, S., & Hu, Y. (2004). Parametric Simulation of Shovel-Oil Sands Interactions During Excavation. *International Journal of Surface Mining, Reclamation and Environment, XVIII*(3), 205-219.

Gates, J. D. (1998, January). Two-body and three-body abrasion: A critical discussion. *Wear, 214*, 139-146.

Global, J. (2015, August 8). *4100C Boss Electric Mining Shovel - AC.* Retrieved from JOYGLOBAL: http://www.joyglobal.com/docs/default-source/product-documents/surface/electric-rope-shovels/xs-5491-1_4100c_boss_ac_bro.pdf?sfvrsn=10

Harper, D., Gill, M., Hart, K. W., & Anderson, M. (2002). Plasma transferred arc overlays reduce operating costs in oil sand processing. *International thermal spray conference* (pp. 278-283). Essen: ASM International.

Hawk, J. A. (2000). Abrasive Wear Testing. In H. Kuhn, & D. Medlin, *Mechanical Testing and Evaluation* (Vol. VIII, pp. 325-337). Materials Park, Ohio: ASM International.

Hawk, J. A., & Wilson, R. D. (2001). Tribology of Earthmoving, Mining, and Minerals Processing. In B. Bhushan (Ed.), *Modern Tribology Handbook* (Vol. II, pp. 1331-1368). Boca Raton, Florida: CRC Press LLC.

Hawk, J. A., Wilson, R. D., Tylczak, J. H., & Doğan, Ö. N. (1999, April). Laboratory abrasive wear tests: investigation of test methods and alloy correlation. *Wear, 225-229*(2), 1031-1042.

Hemami, A., Goulet, S., & Aubertin, M. (1994). Resistance of particulate media to excavation: Application to bucket loading. *International Journal of Surface Mining, Reclamation and Environment, VIII*(3), 125-129.

Hirota, K., Mitani, K., Yoshinaka, M., & Yamaguchi, O. (2005). Simultaneous synthesis and consolidation of chromium carbides (Cr3C2, Cr7C3 and Cr23C6) by pulsed electric-current pressure sintering. *Materials Science and Engineering: A, 399*(1), 154-160.

Hsu, S. M., & Shen, M. C. (2001). Wear Maps. In B. Bhushan (Ed.), *Modern Tribology Handbook* (Vol. I, pp. 317-359). Boca Raton, Florida: CRC Press LLC.

Humphrey, J. D., & Wagner, J. D. (2011). Mechanical Extraction, Loading, and Hauling. In P. Darling (Ed.), *SME Mining Engineering Handbook* (3rd ed., Vol. I, pp. 903-929). Englewood, Colorado: Society for Mining, Metallurgy, and Exploration, Inc.

JCPDS Associateship. (1986, March). *Powder Diffraction File Card No. 36-1482.* Swarthmore, PA: Joint Committee on Powder Diffraction Standards.

Joseph, T. G. (2013). Wear Welding-Lecture 5. Edmonton, Alberta, Canada: University of Alberta. Accessed: November 5, 2015

Joseph, T. G., & Shi, N. (2012). A revised dipper-ground equilibrium derivation for shovels operating in oil, sand, and soft ground. *CIM Journal, III*(1), 47-53.

Karpuz, C., Pasamehmetoglu, A. G., & Muftuoglu, Y. (1992). Performance assessment of hydraulic and cable shovels. *International Journal of Surface Mining and Reclamation, VI*(2), 73-80.

Kato, K., & Adachi, K. (2001). Wear Mechanisms. In B. Bhushan (Ed.), *Modern Tribology Handbook* (Vol. I, pp. 273-300). Boca Raton, Florida: CRC Press LLC.

Li, D. Y., Elalem, K., Anderson, M. J., & Chiovelli, S. (1999). A microscale dynamical model for wear simulation. *Wear, 225-229*, 380-386.

Lin, Z. (2013). *Abrasive Wear of Shovel Teeth in Oil Sand.* Edmonton: University of Alberta.

Llewellyn, R. (1996). Materials for controlling wear in surface mining. *CIM Bulletin, 89*(1002), 76-82.

Llewellyn, R. (1997). Resisting wear attack in oil sands mining and processing. *CIM Bulletin, 90*(1012), 75-82.

Marinescu, I. D., Rowe, W. B., Dimitrov, B., & Inasaki, I. (2004). *Tribology of Abrasive Machining Processes.* Norwich, New York: William Andrew Inc.

McKyes, E. (1985). *Soil Cutting and Tillage.* New York: Elsevier Science Publishing Company, Inc.

Morgenstern, N. R., & Scott, J. D. (1997). Oil Sand Geotechnique. *Geotechnical News*, 102-109.

Mossop, G. D. (1980, Jan. 11). Geology of the Athabasca Oil Sands. *Science, 207*(4427), 145-152.

Patnayak, S., & Tannant, D. D. (2005, December). Performance monitoring of electric cable shovels. *International Journal of Surface Mining, Reclamation and Environment, XIX*(4), 276-294.

Pierson, H. (1996). *Handbook of Refractory Carbides & Nitrides.* Westwood, NJ: William Andrew.

Rabinowicz, E. (1965). *Friction and Wear of Materials.* New York: John Wiley & Sons, Inc.

Shi, N., & Joseph, T. G. (2005). Optimizing Shovel Dipper Design for Cutting Soft Rock and Soils. *International Mining Congress and Fair of Turkey* (pp. 145-151). Izmir: The Chamber of Mining Engineers of Turkey.

Smart, R. F., & Moore, J. C. (1979, September). Materials Selection for Wear Resistance. *Wear, 56*(1), 55-67.

Stavropoulou, M., Xiroudakis, G., & Exadaktylos, G. (2013). Analytical model for estimation of digging forces and specific energy of cable shovel. *Coupled Systems Mechanics, II*(1), 23-51.

Teare, M., Cruickshank, R., Miller, S., Overland, S., & Marsh, R. (2014). *ST98-2014 Alberta's Energy Reserves 2013 and Supply/Demand Outlook 2014-2023.* Calgary: Alberta Energy Regulator.

Torrance, A. A. (2005). Modelling abrasive wear. *Wear, 258*, 281-293.

Tylczak, J. H., Hawk, J. A., & Wilson, R. D. (1999). A comparison of laboratory abrasion and field wear results. *Wear, 225-229*(2), 1059-1069.

Wolfe, T. (2010). *Homogeneity of Metal Matrix Composites Deposited by Plasma Transferred Arc Welding.* Edmonton: University of Alberta.

Xiao, B., Xing, J. D., Feng, J., Zhou, C. T., Li, Y. F., Su, W., . . . Cheng, Y. H. (2009). A comparitive study of Cr7C3, Fe3C and Fe2B in cast iron both from ab initio calculations and experiments. *Journal of Physics D: Applied Physics, 42*, 115415-115431.

Zum Gahr, K. H. (1988). Modelling of Two-Body Abrasive Wear. *Wear, 124*(1), 87-103.

Appendix A Sample Raw Data

Time (s)	Hoist Length (m)	Crowd Length (m)	Dig v (m/s)	Hoist F (kN)	Crowd F (kN)	Hoist P (kW)	Crowd P (kW)	Hoist Current (A)	Crowd Current (A)	Hoist Voltage (V)	Crowd Voltage (V)
16.968	16.937	2.907	-0.438	732	384	320	179	753	447	246	464
17.069	16.896	2.954	-0.438	1,780	225	780	105	1872	256	241	475
17.170	16.852	3.003	-0.670	1,930	205	1,290	96	2731	236	273	470
17.271	16.775	3.063	-0.695	2,590	537	1,800	265	3005	703	346	436
17.372	16.706	3.107	-0.695	2,500	779	1,740	344	2650	910	379	437
17.473	16.639	3.138	-0.670	1,790	620	1,200	274	1744	716	397	442
17.574	16.570	3.193	-0.592	1,290	640	765	274	1173	702	377	452
…	…	…	…	…	…	…	…	…	…	…	…
…	…	…	…	…	…	…	…	…	…	…	…
…	…	…	…	…	…	…	…	…	…	…	…
…	…	…	…	…	…	…	…	…	…	…	…
23.533	11.776	4.649	-1.159	-2,250	714	2,610	232	2644	957	571	280
23.634	11.660	4.681	-1.082	-2,240	822	2,420	267	2456	995	569	310
23.735	11.555	4.680	-1.082	-2,010	770	2,180	280	2206	955	571	339
23.836	11.448	4.742	-1.082	-1,930	726	2,090	311	2098	1010	575	356
23.937	11.340	4.778	-1.082	-1,880	739	2,030	317	2018	1003	581	365
24.038	11.201	4.834	-1.004	-1,780	774	1,790	332	1951	954	529	402
24.139	11.106	4.877	-1.004	-2,570	696	2,580	389	2773	1040	537	432
…	…	…	…	…	…	…	…	…	…	…	…
…	…	…	…	…	…	…	…	…	…	…	…
…	…	…	…	…	…	…	…	…	…	…	…
…	…	…	…	…	…	…	…	…	…	…	…
43.026	3.506	6.035	0	0	8.4	1.441	0.109	833	14	1	9
43.127	3.506	6.036	0	0	19.177	4.370	0.249	842	32	3	9
43.228	3.506	6.037	0	0	18.644	4.012	0.242	773	35	3	8
43.329	3.506	6.039	0	0	12.585	5.723	0.163	827	27	4	7
43.430	3.506	6.043	0	0	5.327	2.948	0.069	852	10	2	8
43.531	3.506	6.039	0	0	0	4.557	-0.121	878	-20	3	7
43.632	3.512	6.040	0	0	0	5.668	-0.048	819	-11	4	5

Appendix B Abrasive Media SEM Images

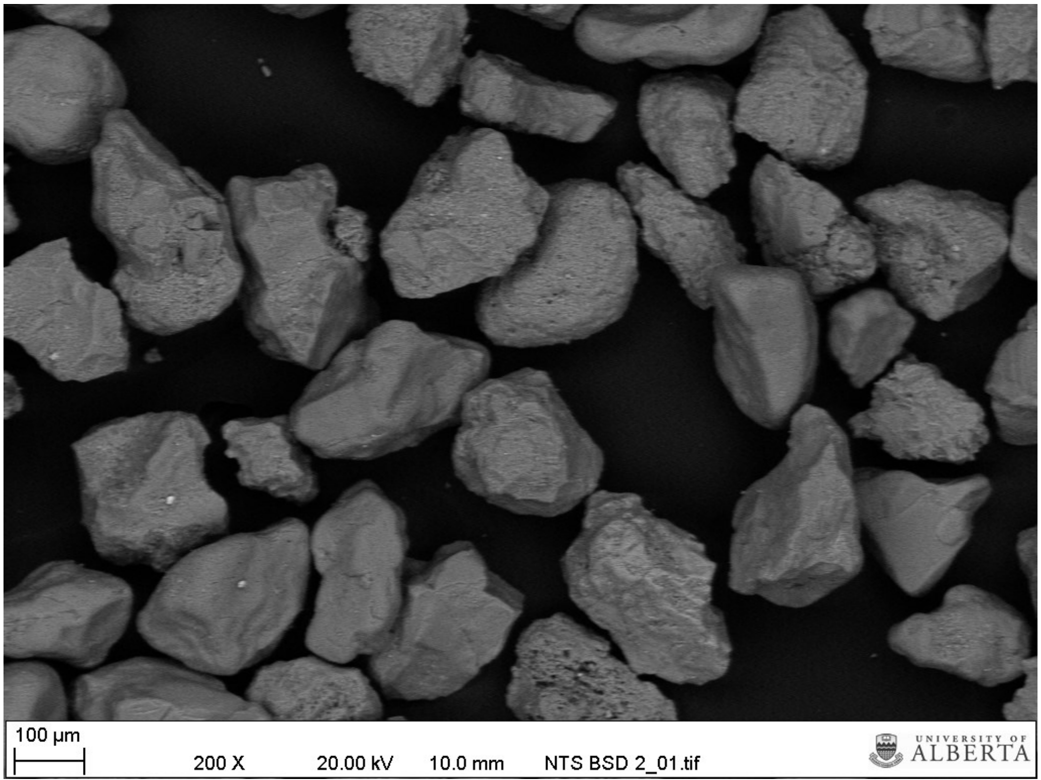

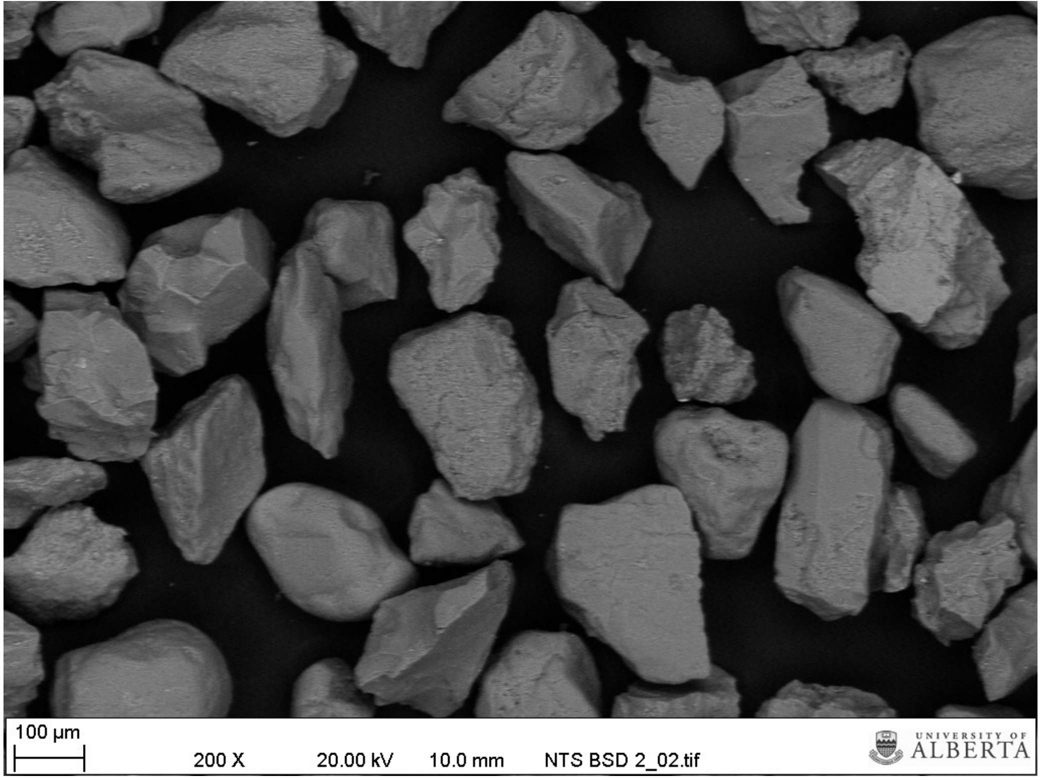

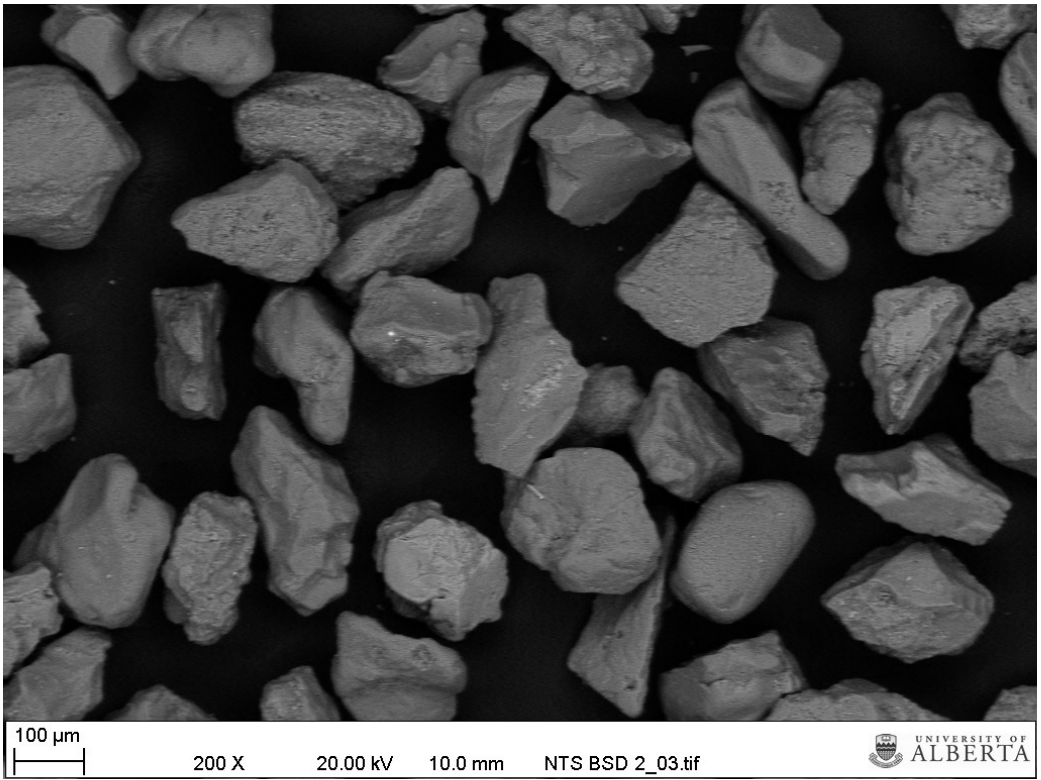
100 µm
200 X
20.00 kV
10.0 mm
NTS BSD 2_03.tif
UNIVERSITY OF ALBERTA

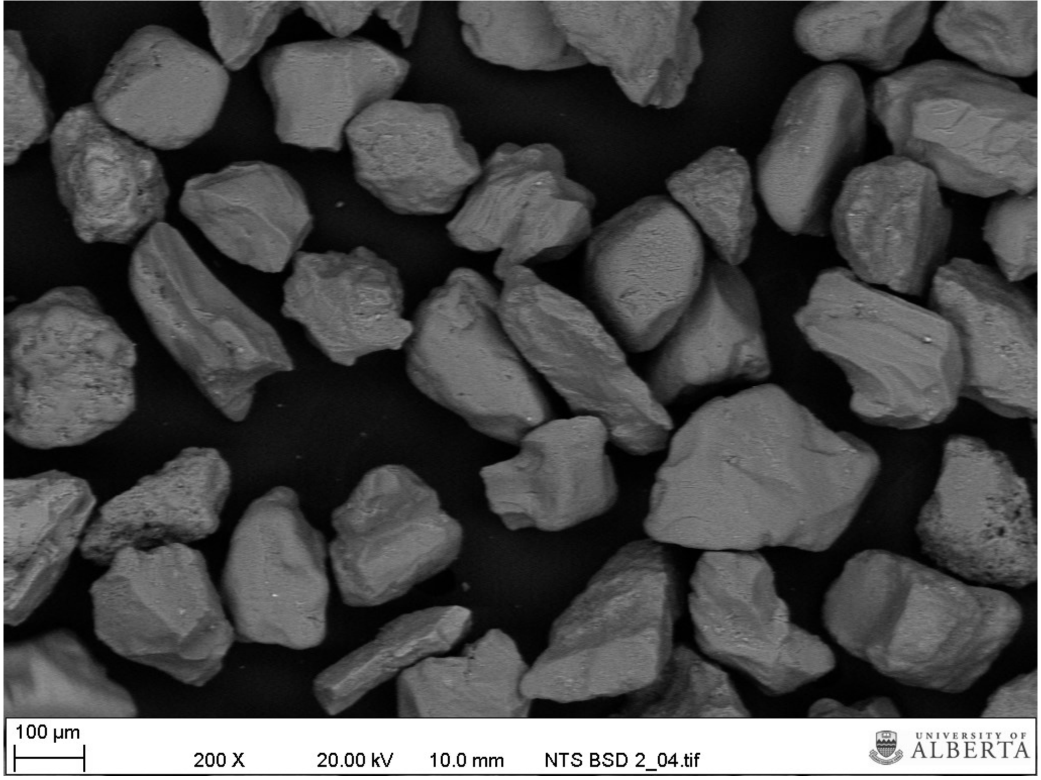
100 µm
200 X
20.00 kV
10.0 mm
NTS BSD 2_04.tif
UNIVERSITY OF ALBERTA

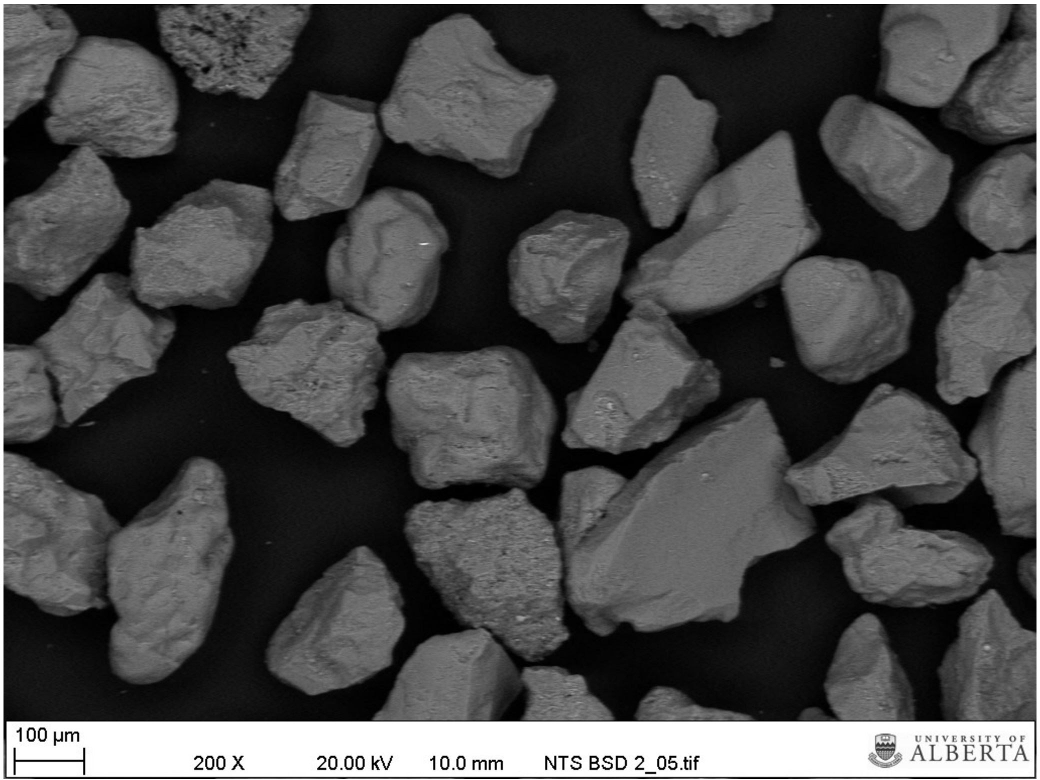
100 µm
200 X
20.00 kV
10.0 mm
NTS BSD 2_05.tif
UNIVERSITY OF ALBERTA

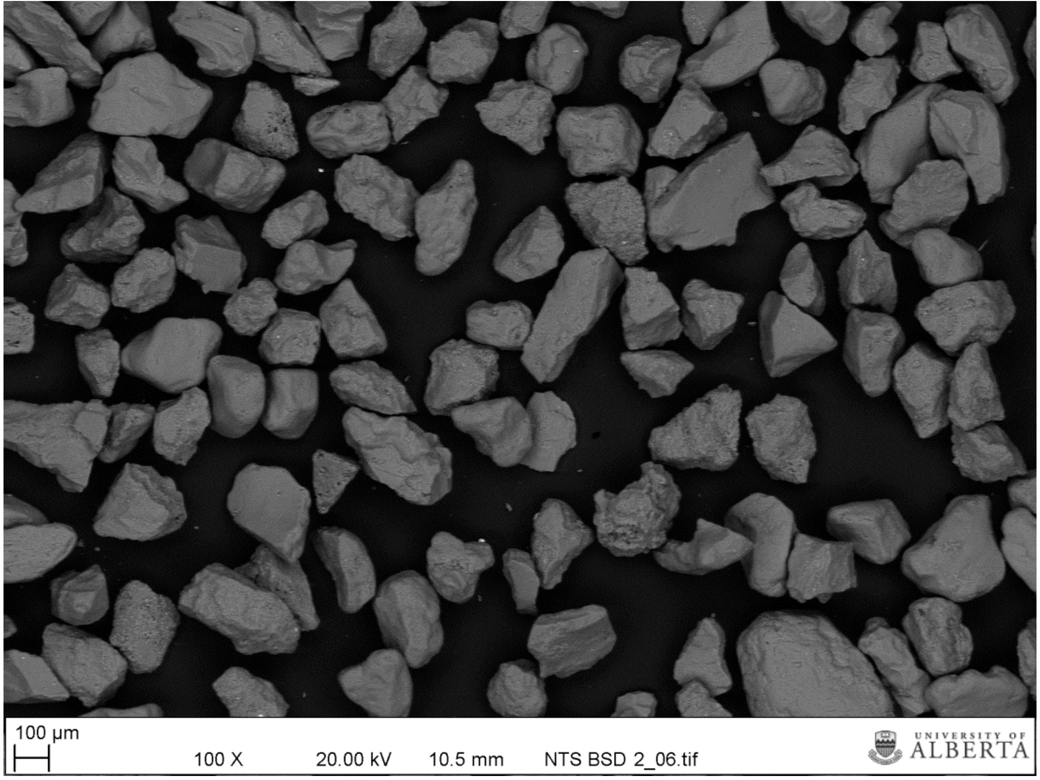
100 µm
100 X
20.00 kV
10.5 mm
NTS BSD 2_06.tif
UNIVERSITY OF ALBERTA

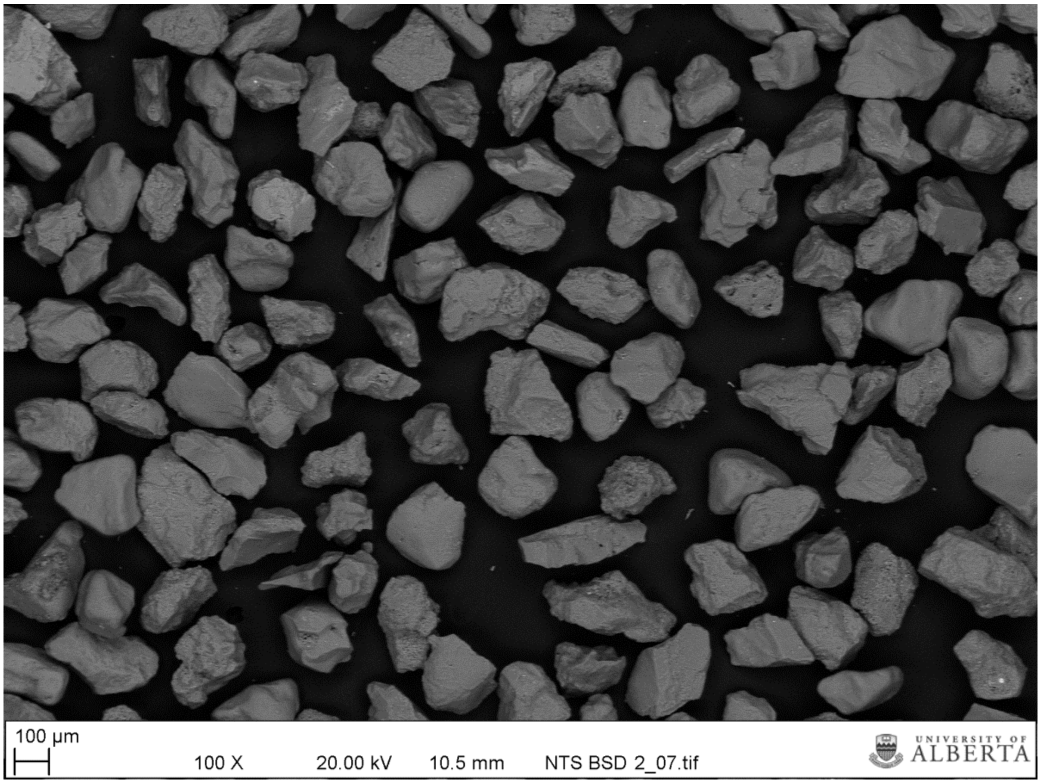
100 µm
100 X
20.00 kV
10.5 mm
NTS BSD 2_07.tif
UNIVERSITY OF ALBERTA

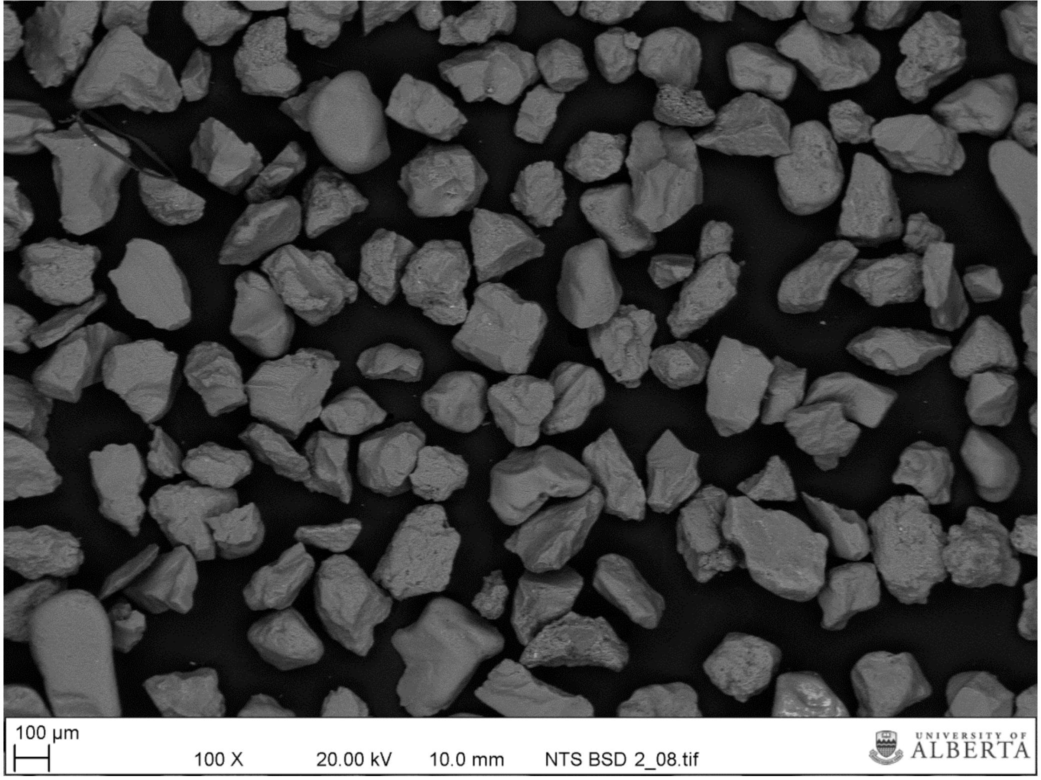
100 µm
100 X
20.00 kV
10.0 mm
NTS BSD 2_08.tif
UNIVERSITY OF ALBERTA

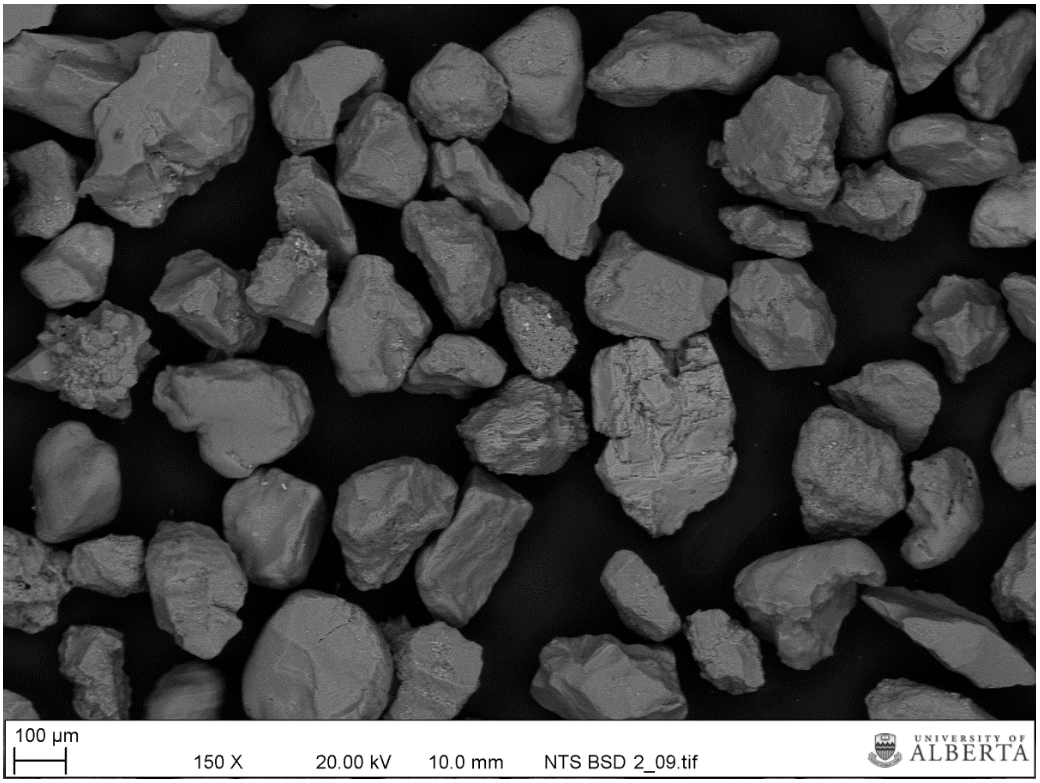
100 µm
150 X
20.00 kV
10.0 mm
NTS BSD 2_09.tif
UNIVERSITY OF ALBERTA

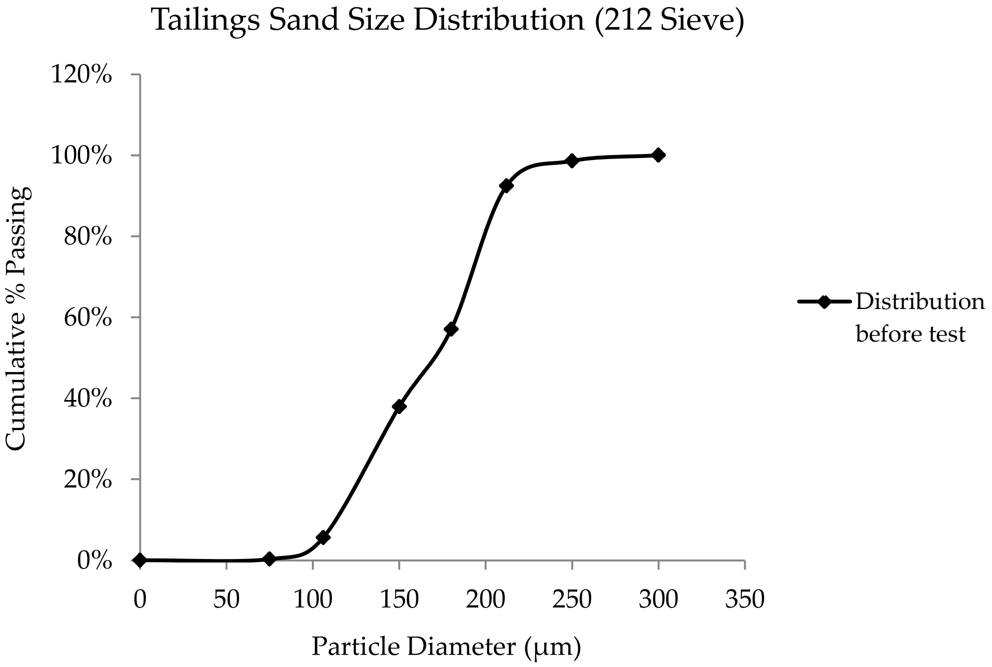
Tailings Sand Size Distribution (212 Sieve)
Cumulative % Passing
120%
100%
80%
60%
40%
20%
0%
0
50
100
150
200
250
300
350
Particle Diameter (µm)
Distribution before test

Appendix C Additional Coupon Images

The coupon images below show wear scars after 525 m of lineal abrasion under the cyclic loading conditions. As the normal force exerted increased, the wear scar area increased as well; however, only the height of the wear scar changed. This is to be expected, as the wheel has a set width. Direction of wear is top to bottom in all images.

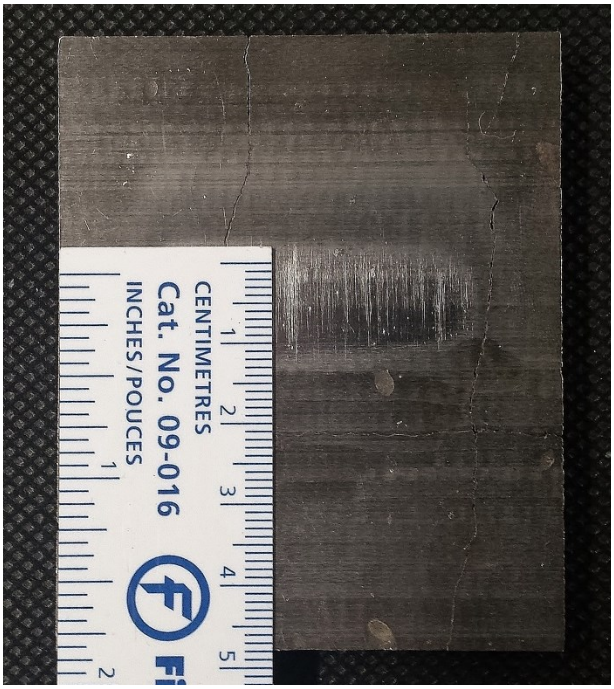

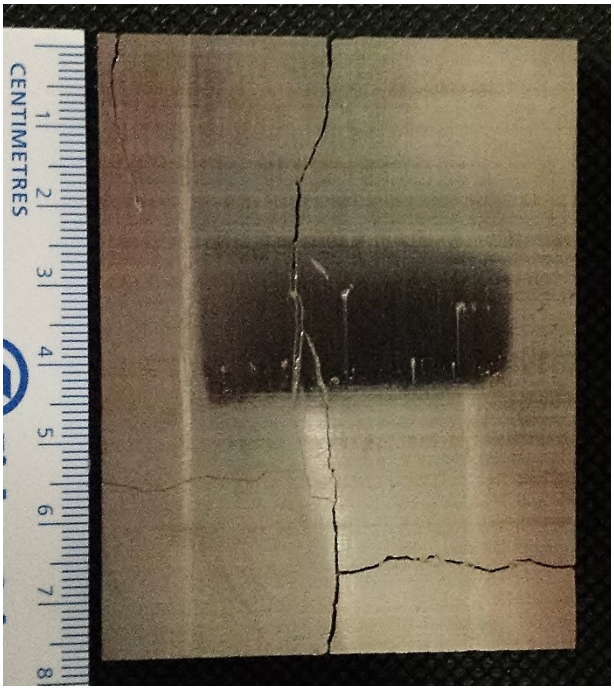

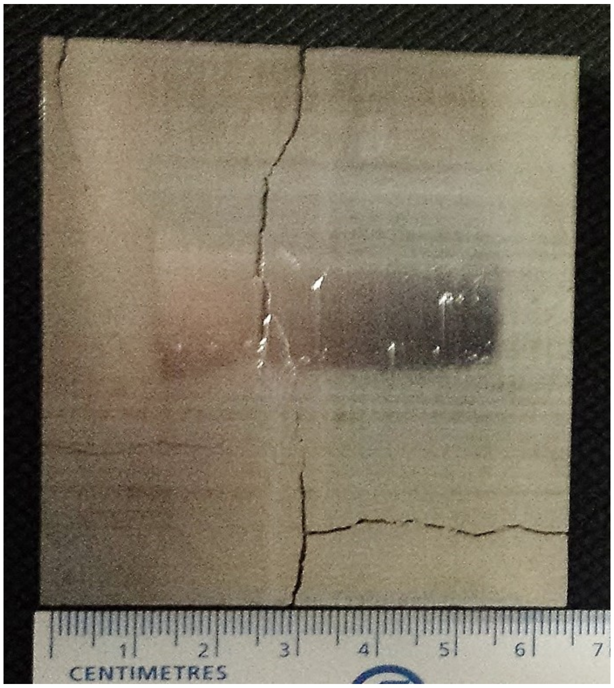

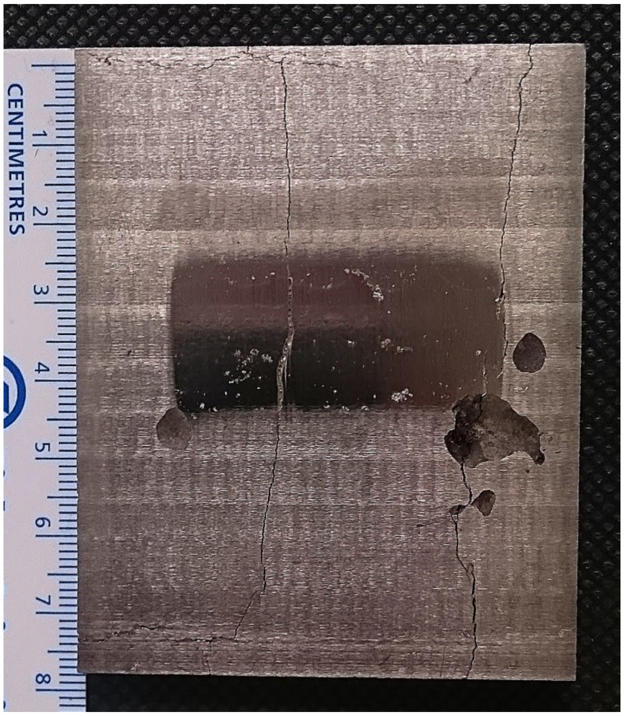

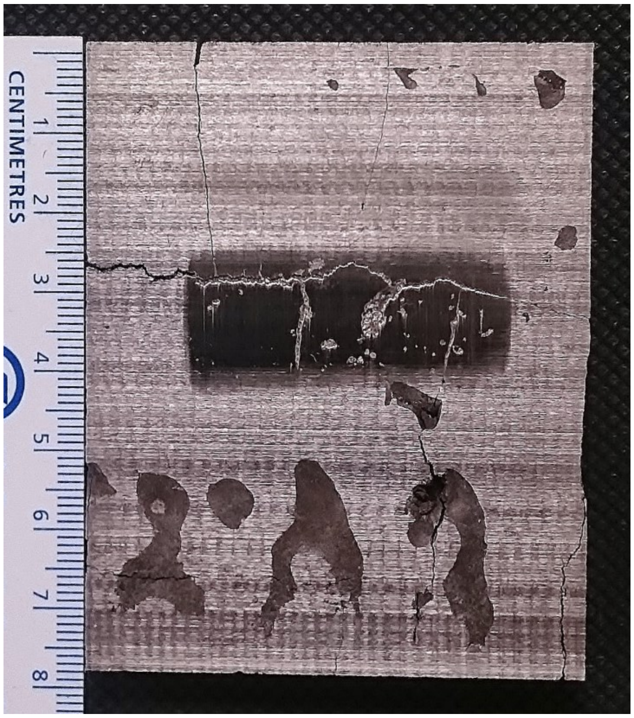

The dull, irregular depressions are the pits previously mentioned. In real-world applications, large pits are filled in on-site. It is possible that the presence of the pits can influence or skew the wear rates, as coupons # 5 (left) & # 7 had significant pits and had higher material loss, but coupon # 9 (right) also had pits and did not seem to suffer from exaggerated CrC loss comparatively. No coupons had any major pits present within their wear scar boundaries; however some cooling cracks were present.

This is the side view of the coupons. The top half is the CrC overlay and the bottom half is the base 44W steel. A sketch of this profile can be seen in Figure 4.8.

The following two images are taken at the exact same location of a test coupon's wear scar. Careful examination shows the darker regions (the carbides) in the second image more or less correspond to peaks in topography on the first image. This is better illustrated in Figures 5.3 & 5.4. Note: the direction of abrasive particle travel in the following images is right to left.

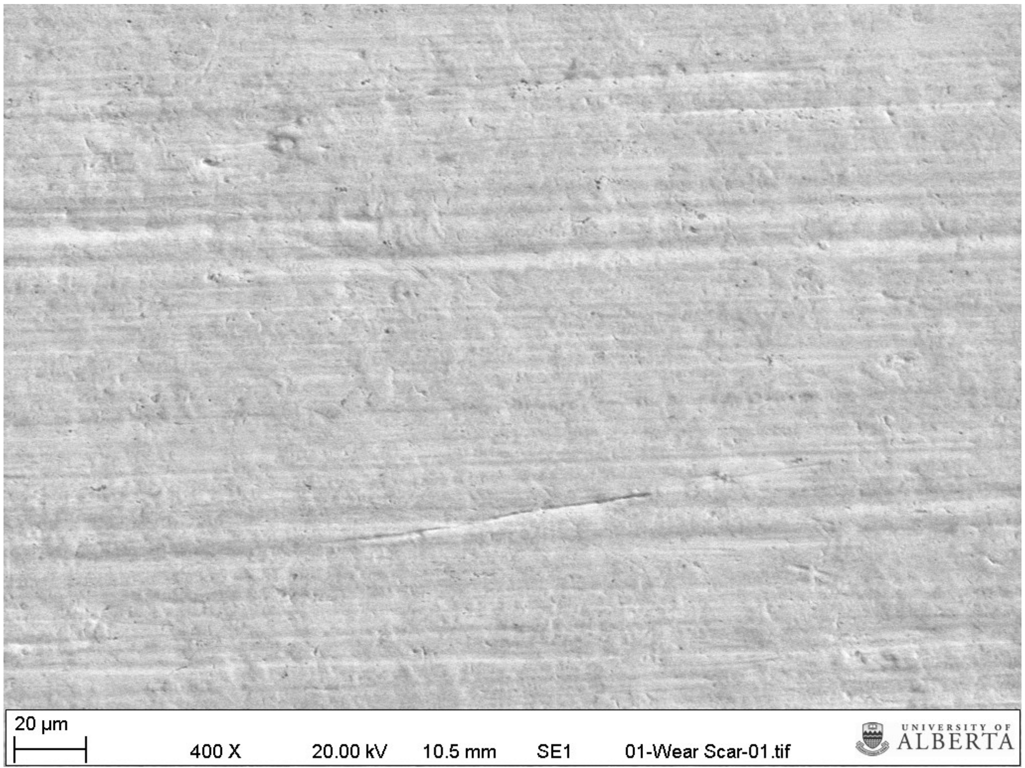

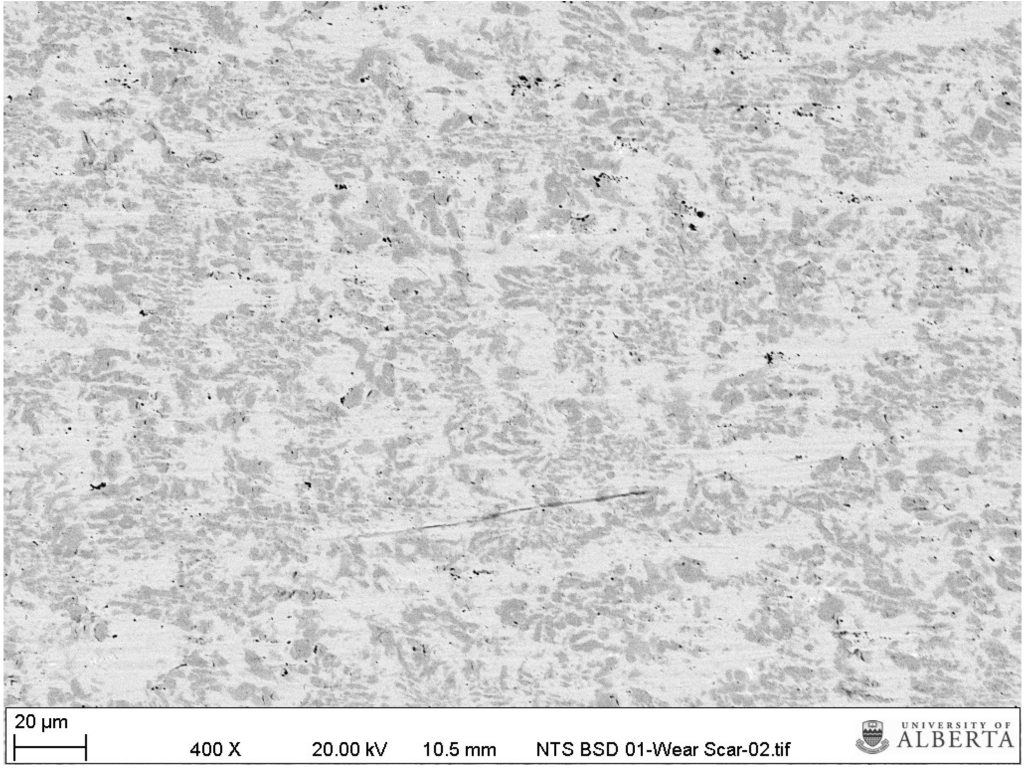

The following two images were taken at the boundary of the wear scar and the smooth surface-ground finish. All coupons were abraded in the perpindicular direction to the motion of the diamond wheel surface grinding. The boundary is indicated by the white arrows. In the second image, the wear scar is revealed to be much more finely ground down, to a polished-like finish.

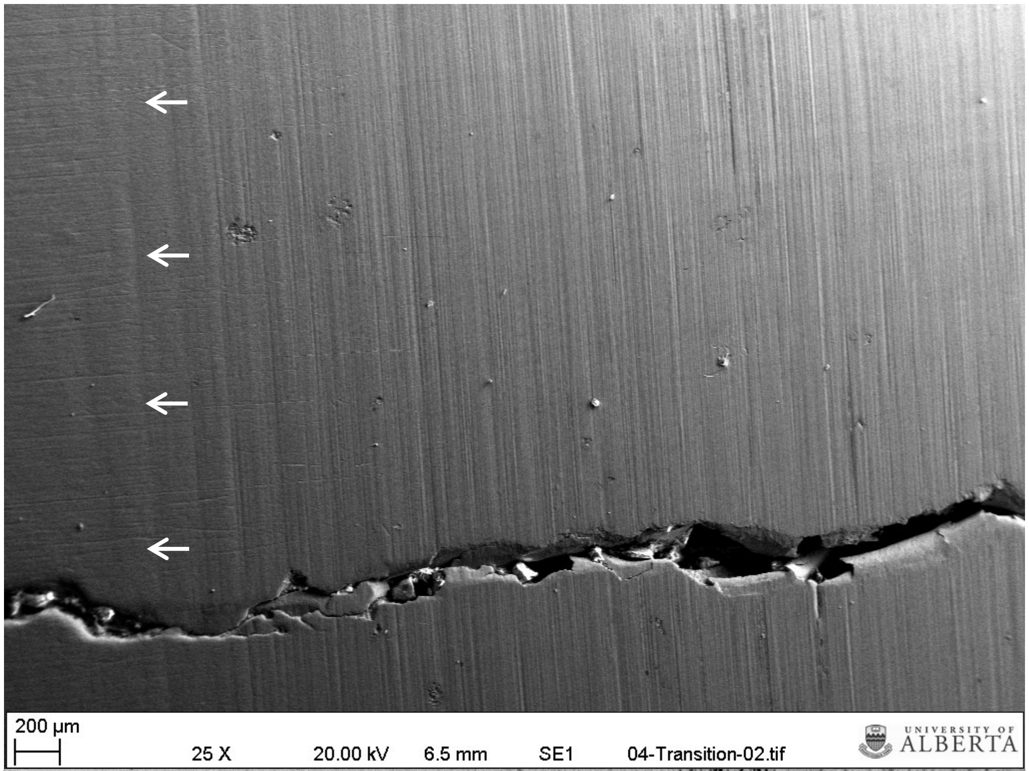

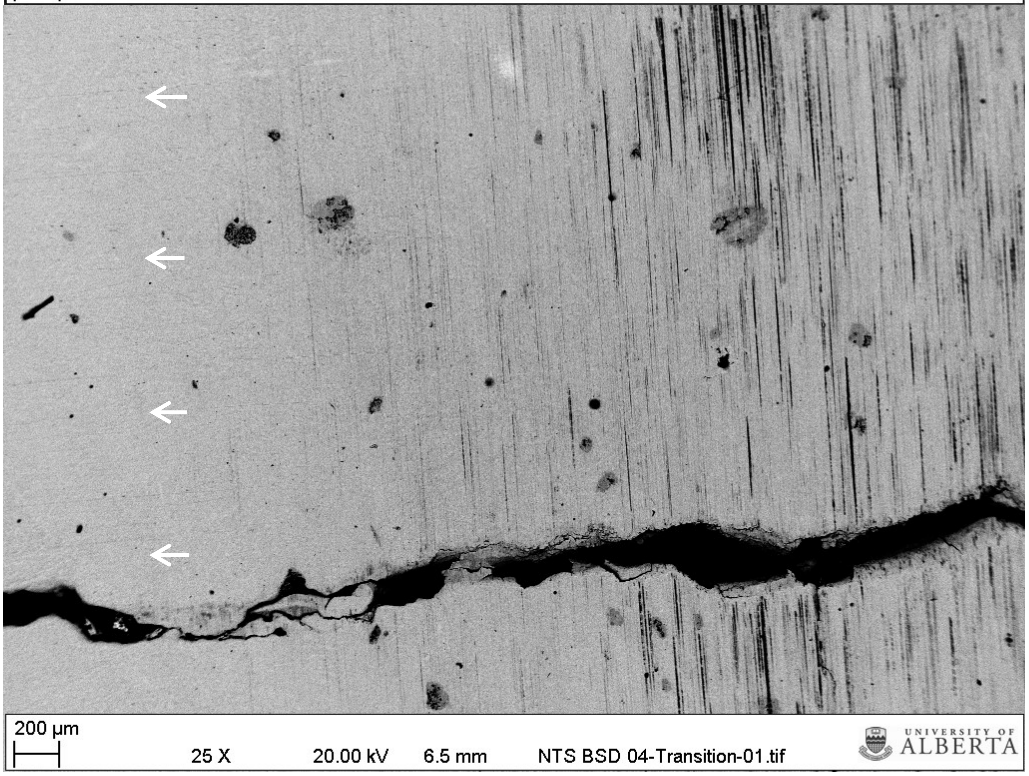

Additional optical microscope images showing the flatter topography of the constantly loaded coupons versus the more undulatory surface of the variably loaded coupons. Abrasive flow direction is out of the page.

Constant Load:

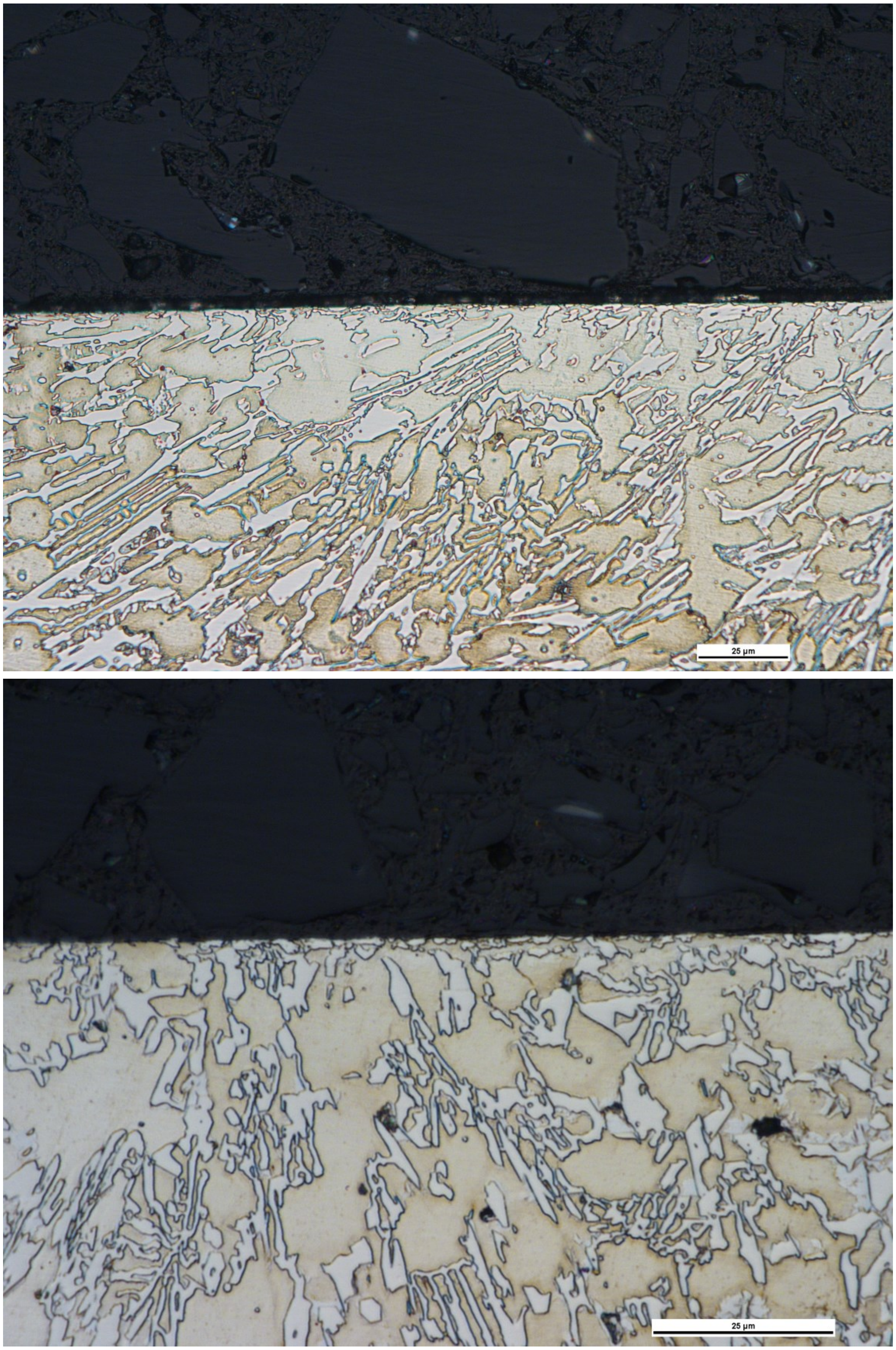

Cyclical Load:

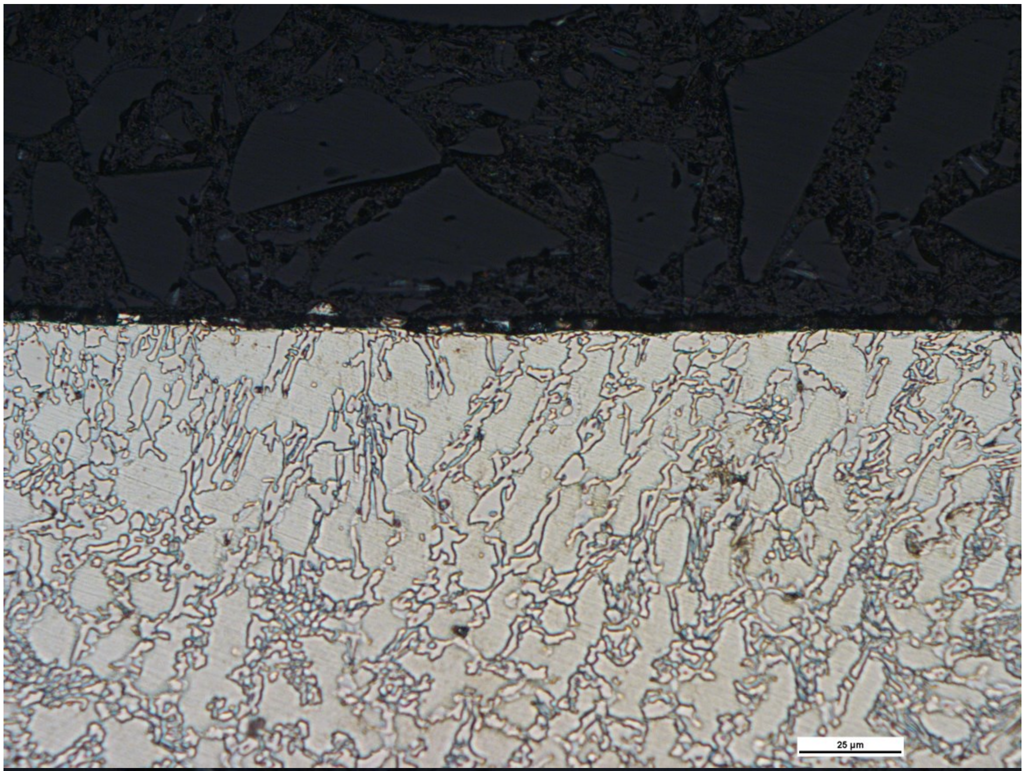

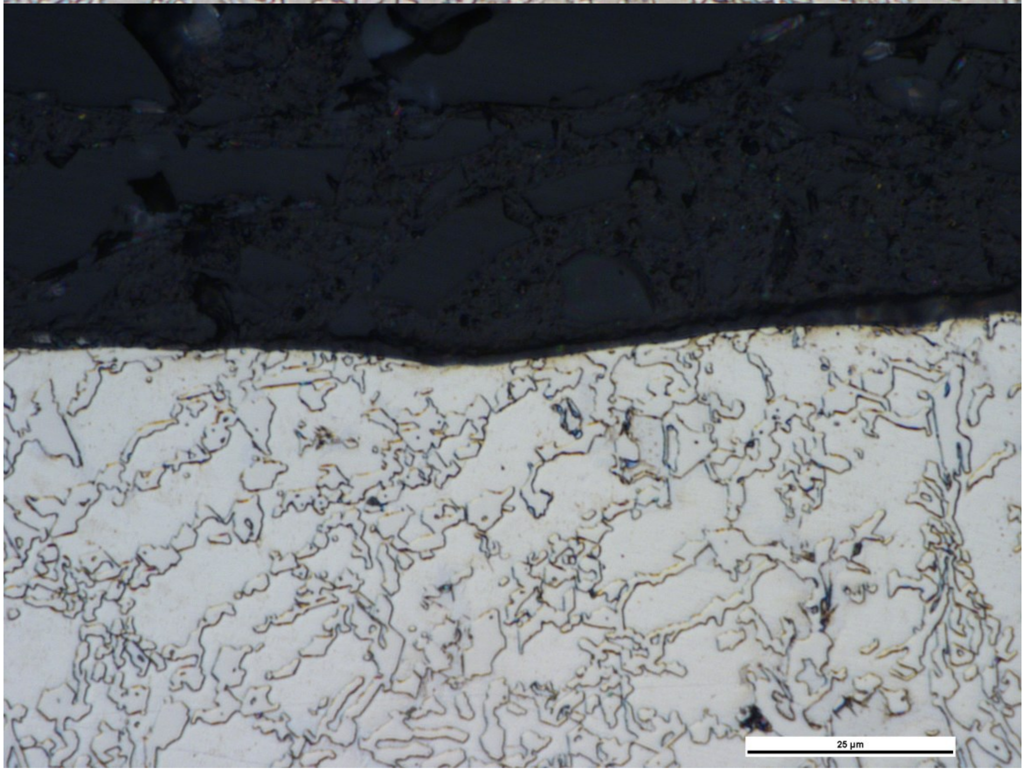

The subsequent set of images are taken from the second round of SEM imaging, and are from a different SEM machine than the previous images in this Appendix. The first four images below are taken in the centre of a constantly loaded coupon. The white squares represent selected areas of interest. The objects protruding from the surface are believed to be the carbides, still intact.

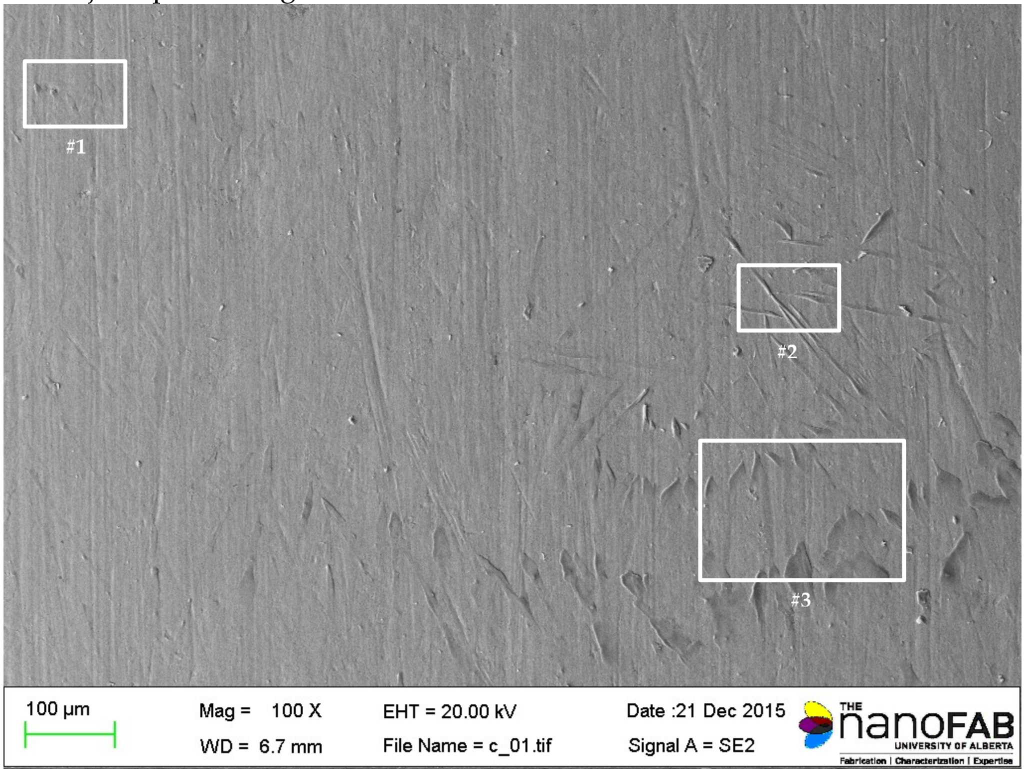

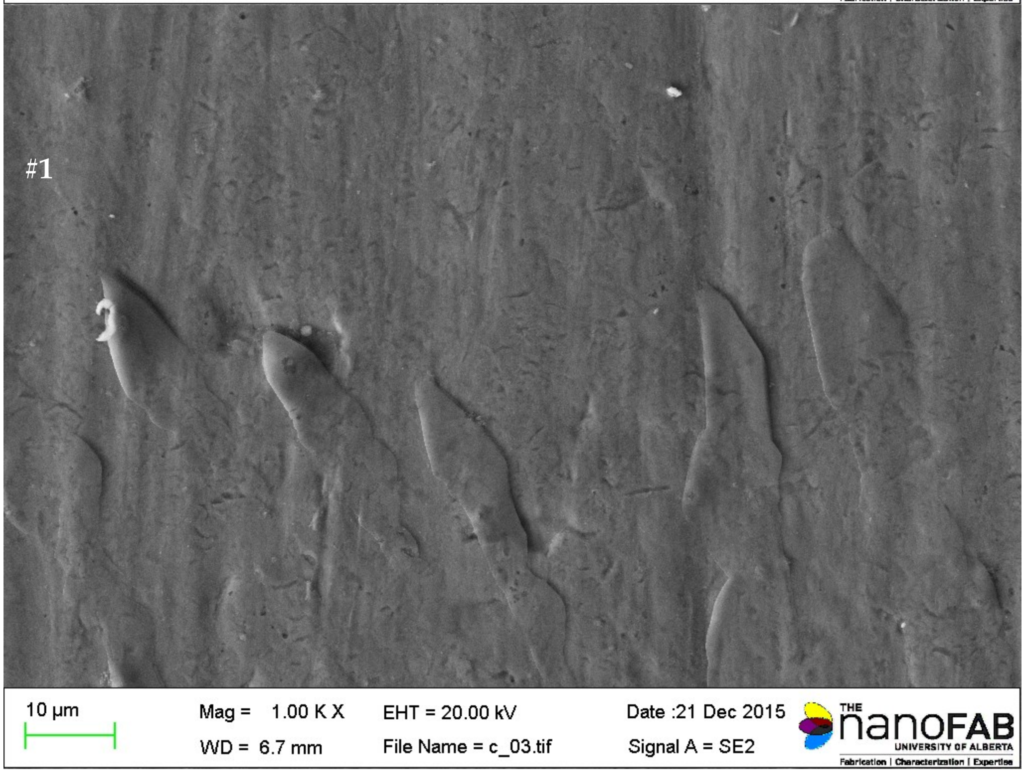

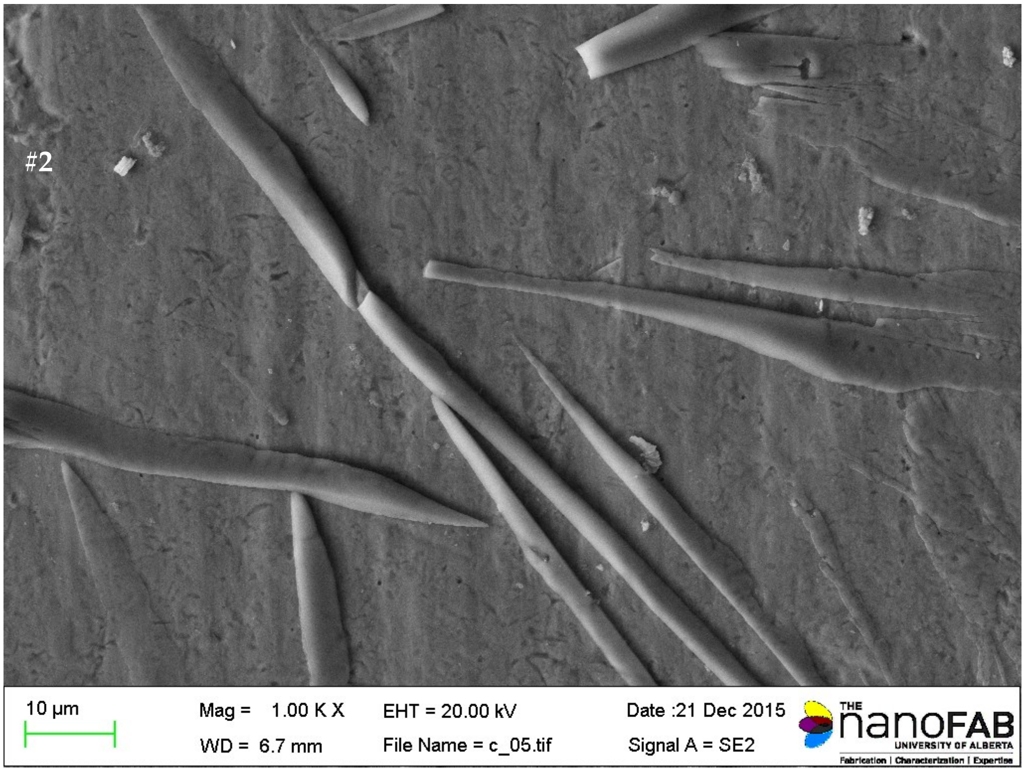

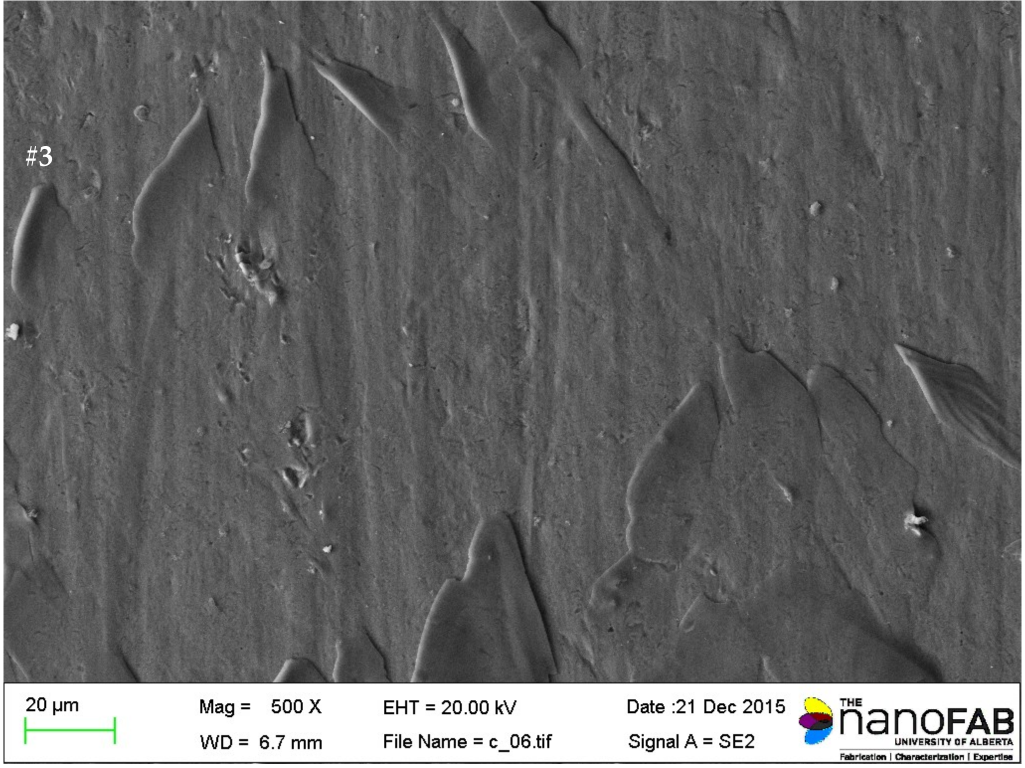

The carbides in these images do not appear to be broken or torn out. Instead, the softer iron matrix material around the carbides is what is worn down (as expected). The second selected area of intrest particularly highlights the rod-like shape of the carbides.

These images are of the variably loaded coupon. Similar to those on Page 95, but from a different machine. Note the lack of protruding carbides that were present in the constant load images.

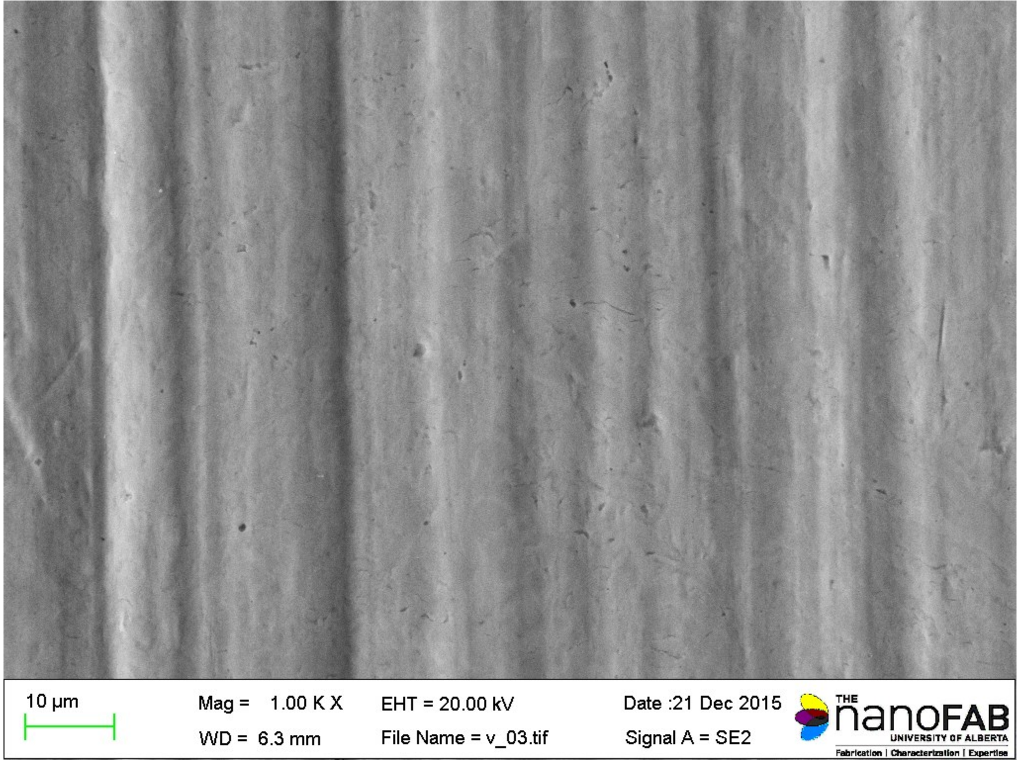

The two images shown here are from the centre of the wear scar. The deep grooves are very noticeable, and the backscatter image below shows the darker regions representing the carbides are visible below the coupon's surface.

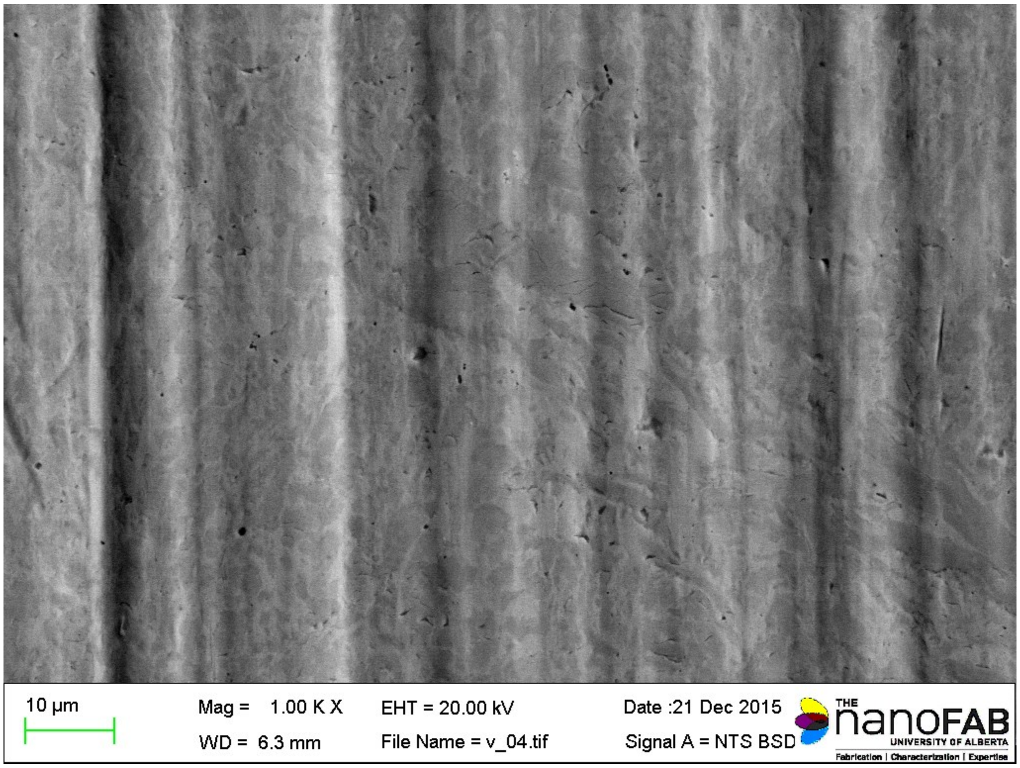

The large pit shown below is the surface damage mentioned in Section 6.5.2. Nothing like this was visible on the constantly loaded wear scars. It is possible this is an instance of spalling due to the fatigue damage from the variably applied load.

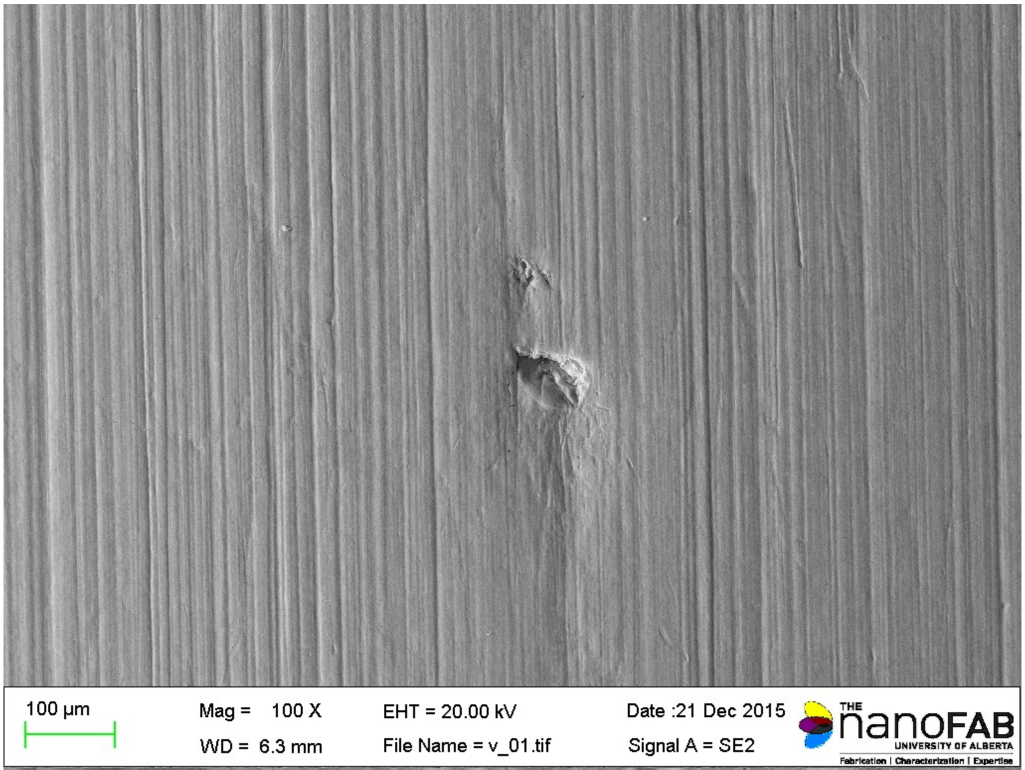

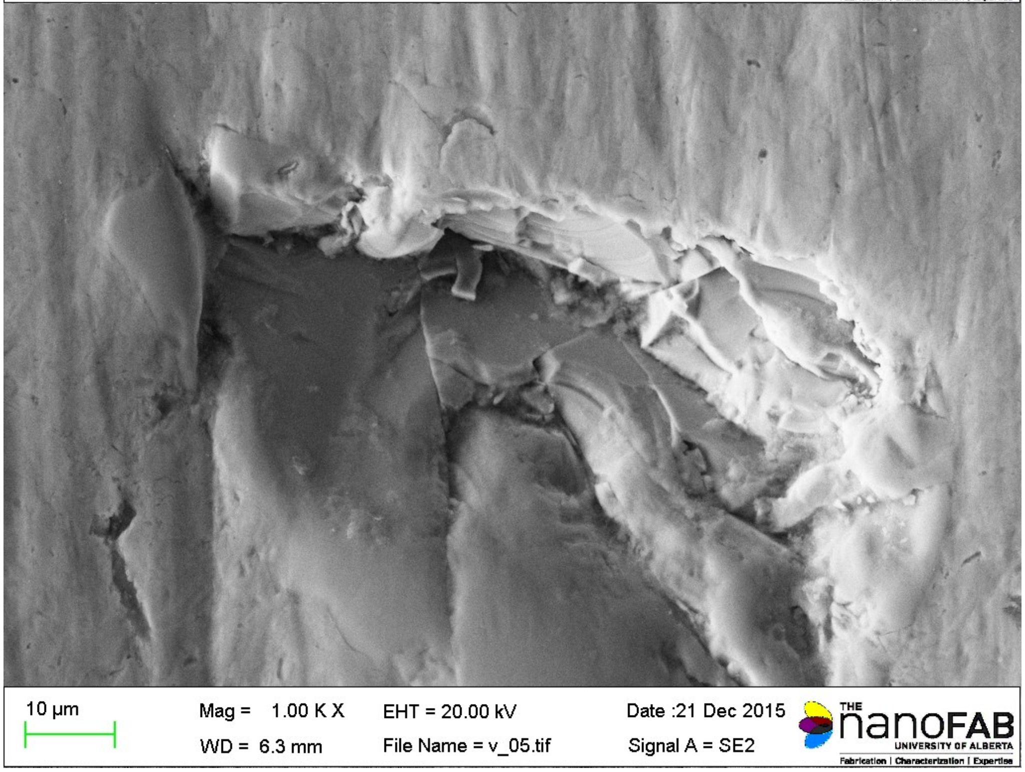

Below are two additional SEM cross section images. The profile of the variably loaded coupon is wavier than shown by the contantly loaded coupon and the grooves are deeper.

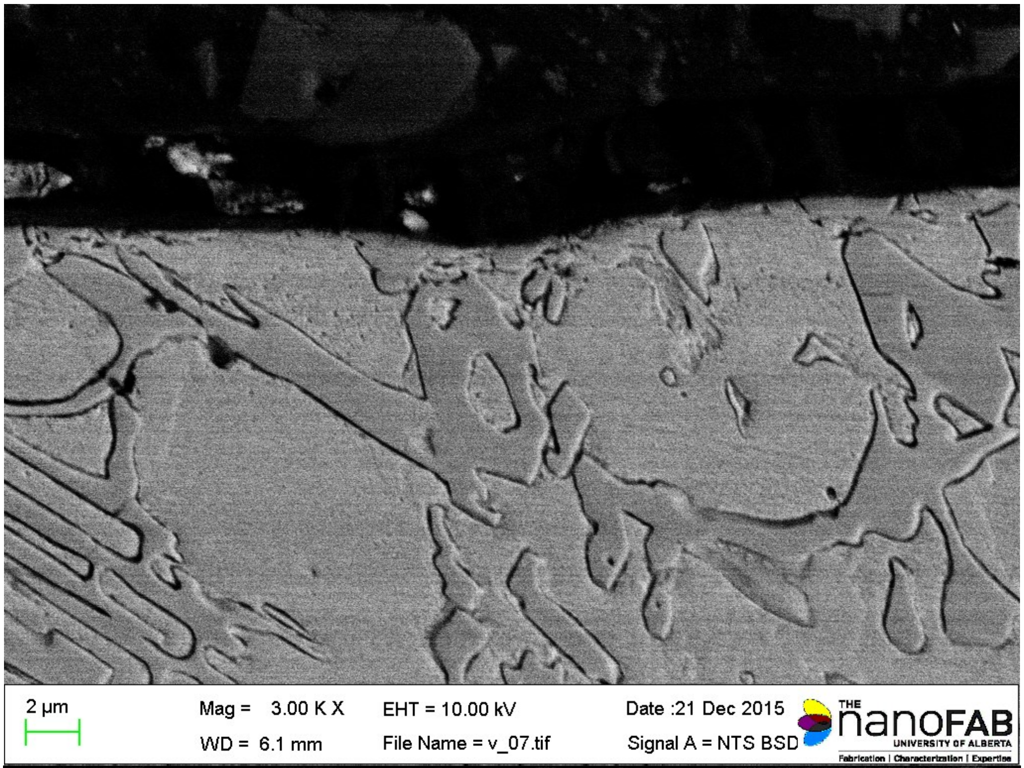

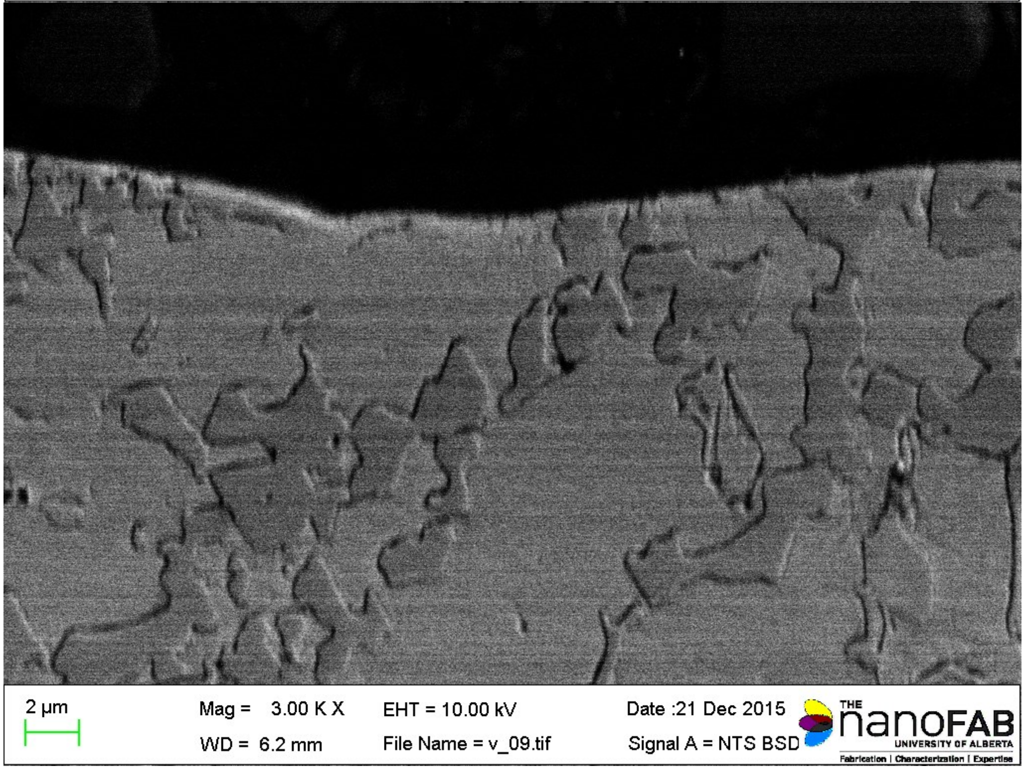

Appendix D Coupon Loading Patterns

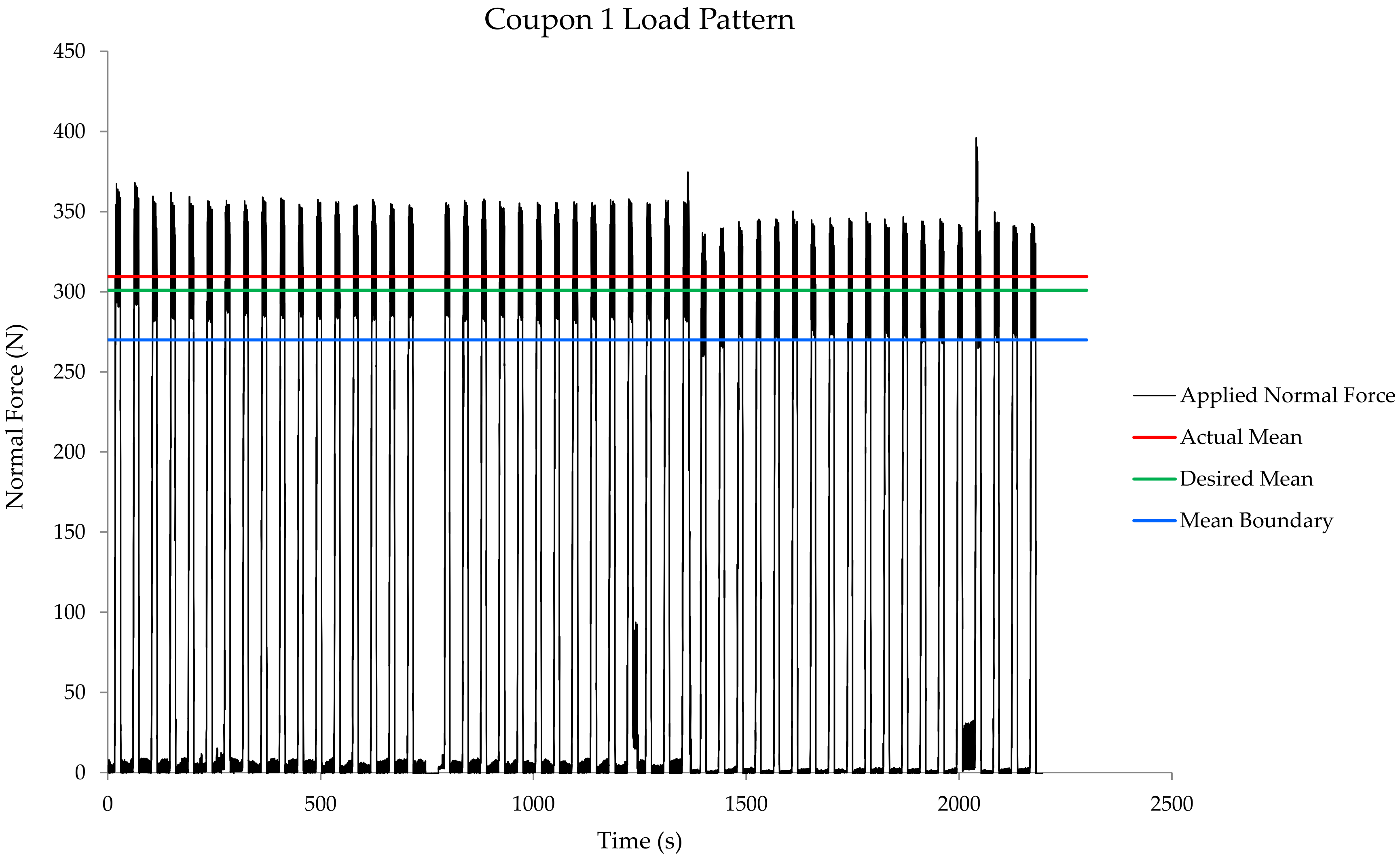

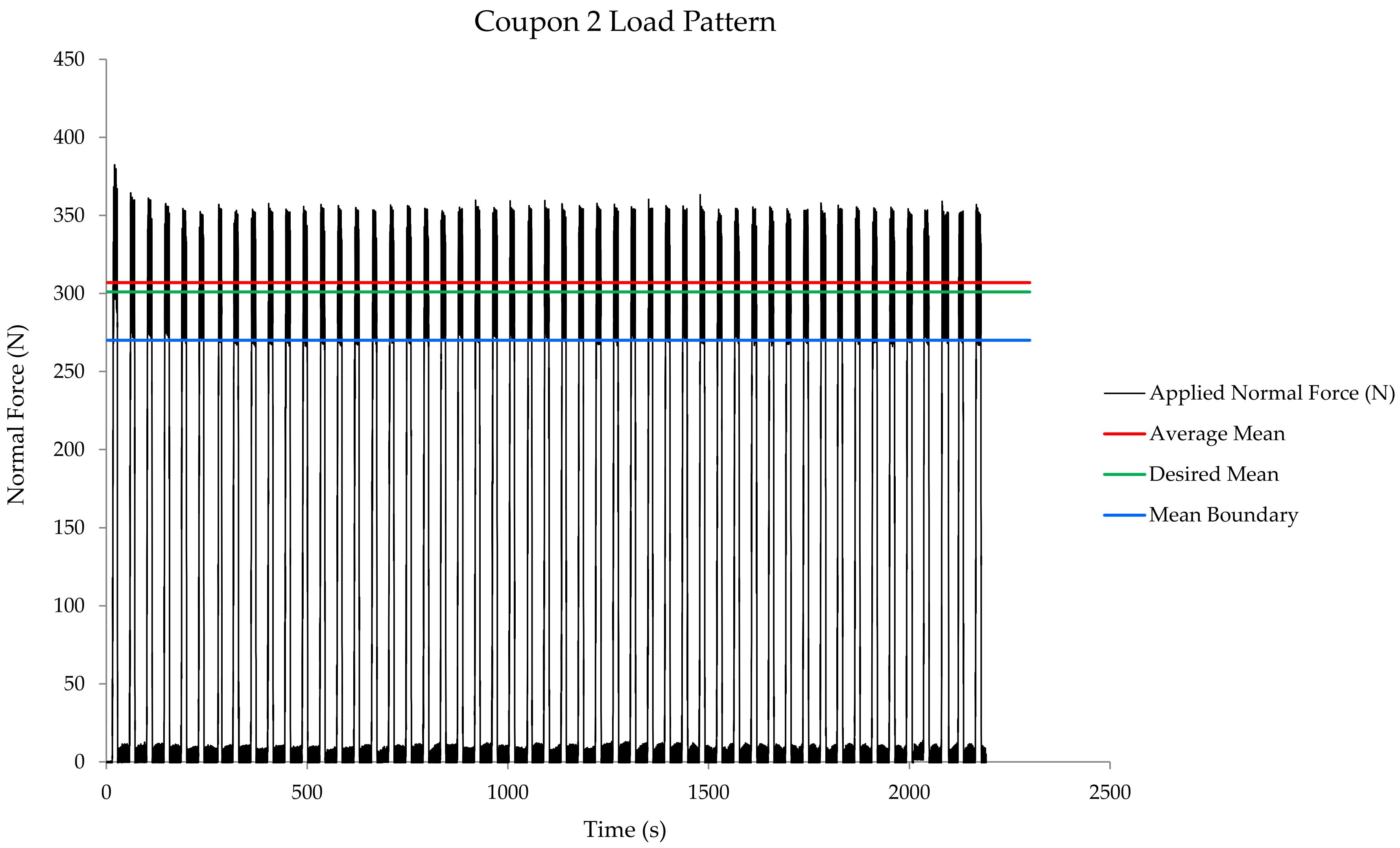

The average mean was calculated using an AVERAGEIF() function in Microsoft Excel™. The criteria that defined which data was used in the average was ">270", or, any points that were greater than 270 N. This number represents 90 % of the desired value of 301 N.

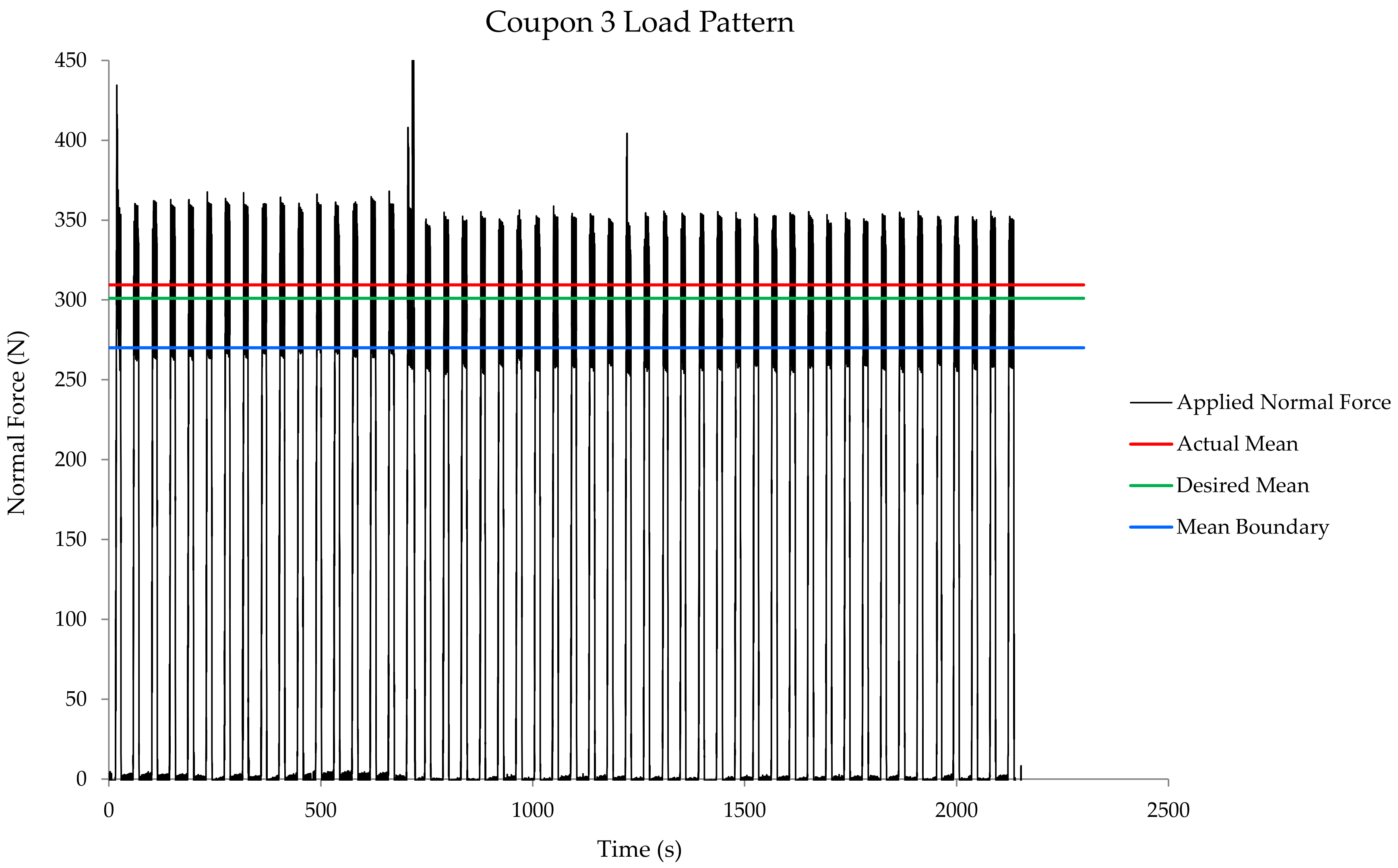
Coupon 3 Load Pattern
Normal Force (N)
450
400
350
300
250
200
150
100
50
0
0
500
1000
1500
2000
2500
Time (s)
Applied Normal Force
Actual Mean
Desired Mean
Mean Boundary

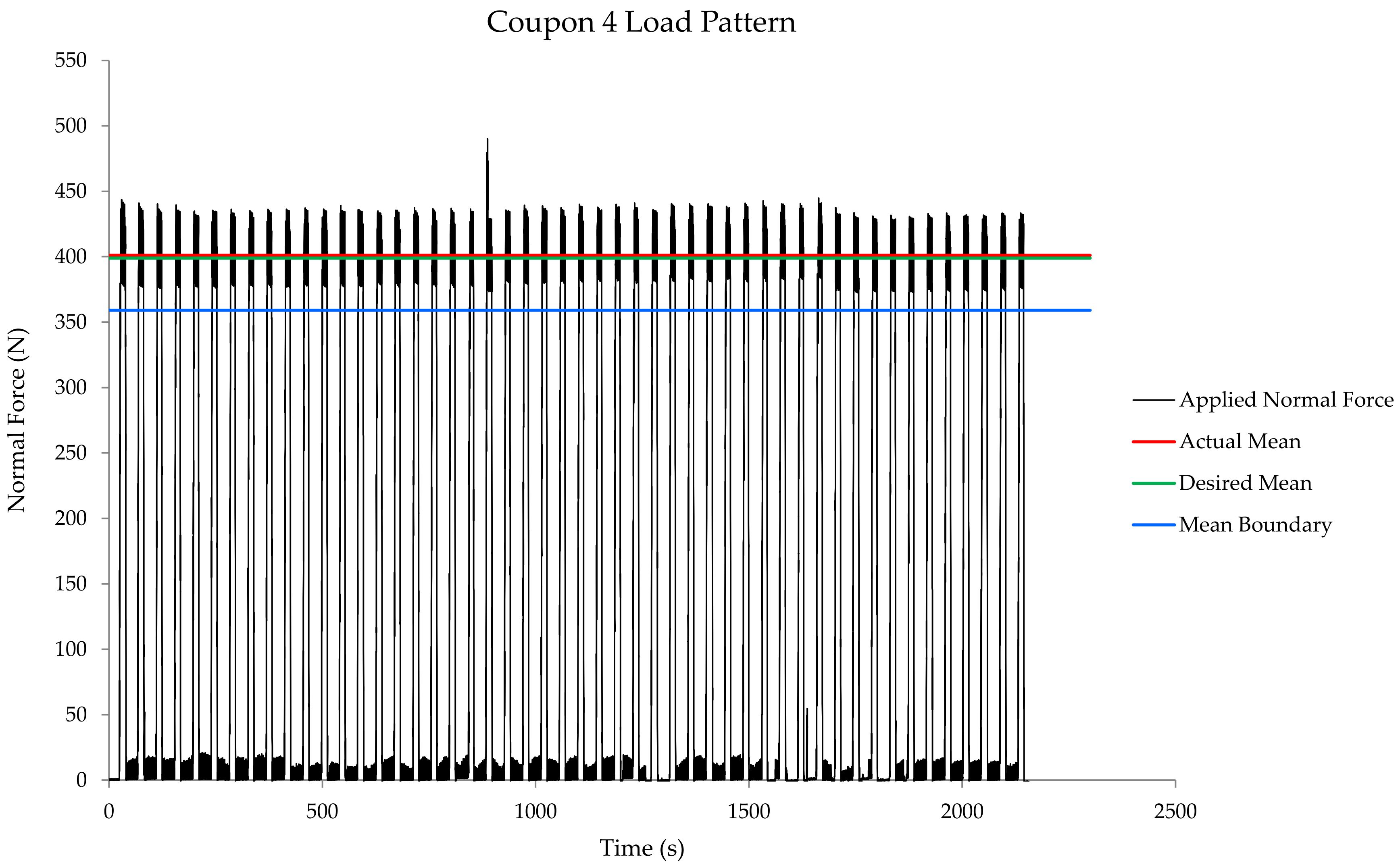
Coupon 4 Load Pattern
Normal Force (N)
550
500
450
400
350
300
250
200
150
100
50
0
0
500
1000
1500
2000
2500
Time (s)
Applied Normal Force
Actual Mean
Desired Mean
Mean Boundary

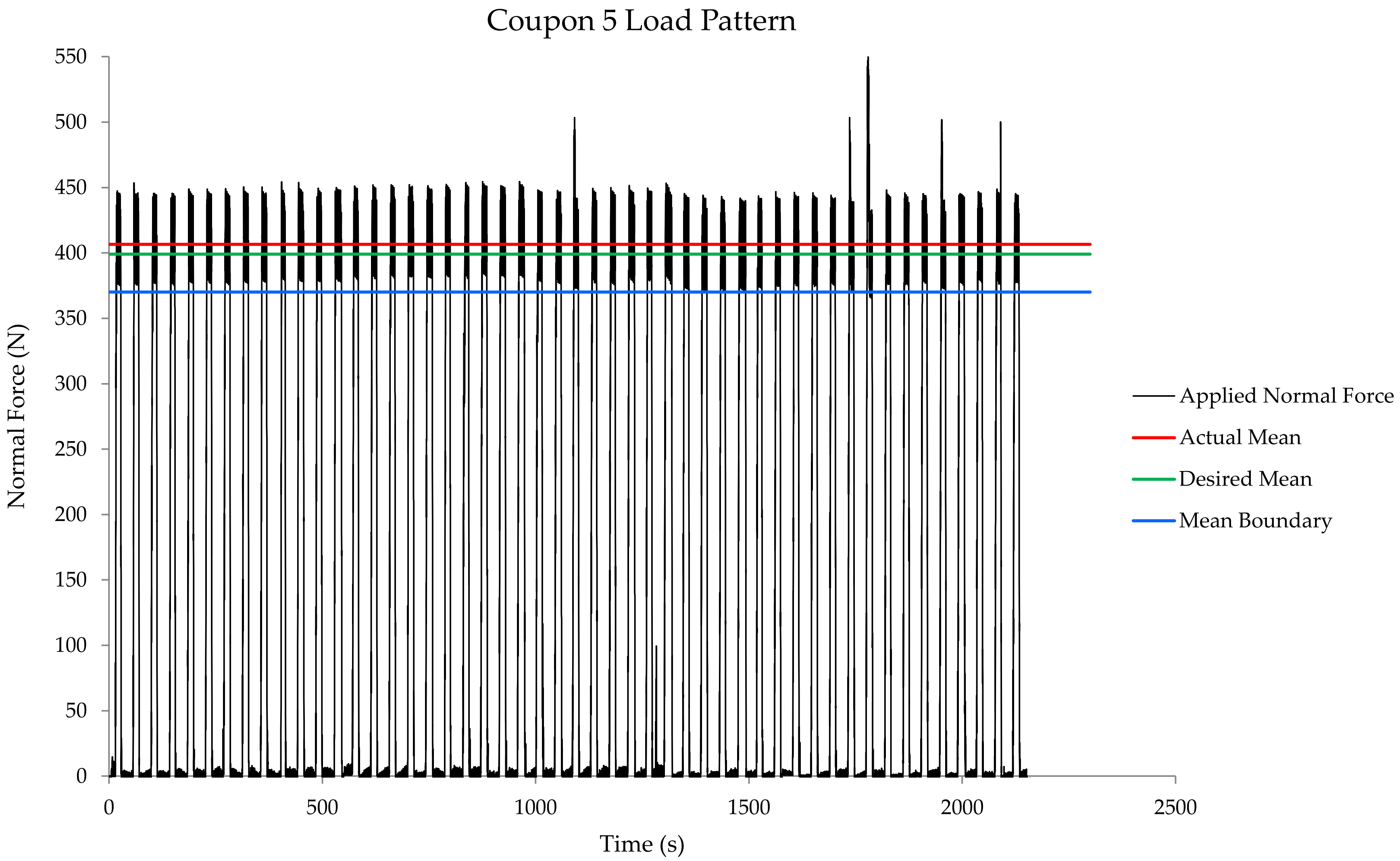
Coupon 5 Load Pattern
Normal Force (N)
550
500
450
400
350
300
250
200
150
100
50
0
0
500
1000
1500
2000
2500
Time (s)
Applied Normal Force
Actual Mean
Desired Mean
Mean Boundary

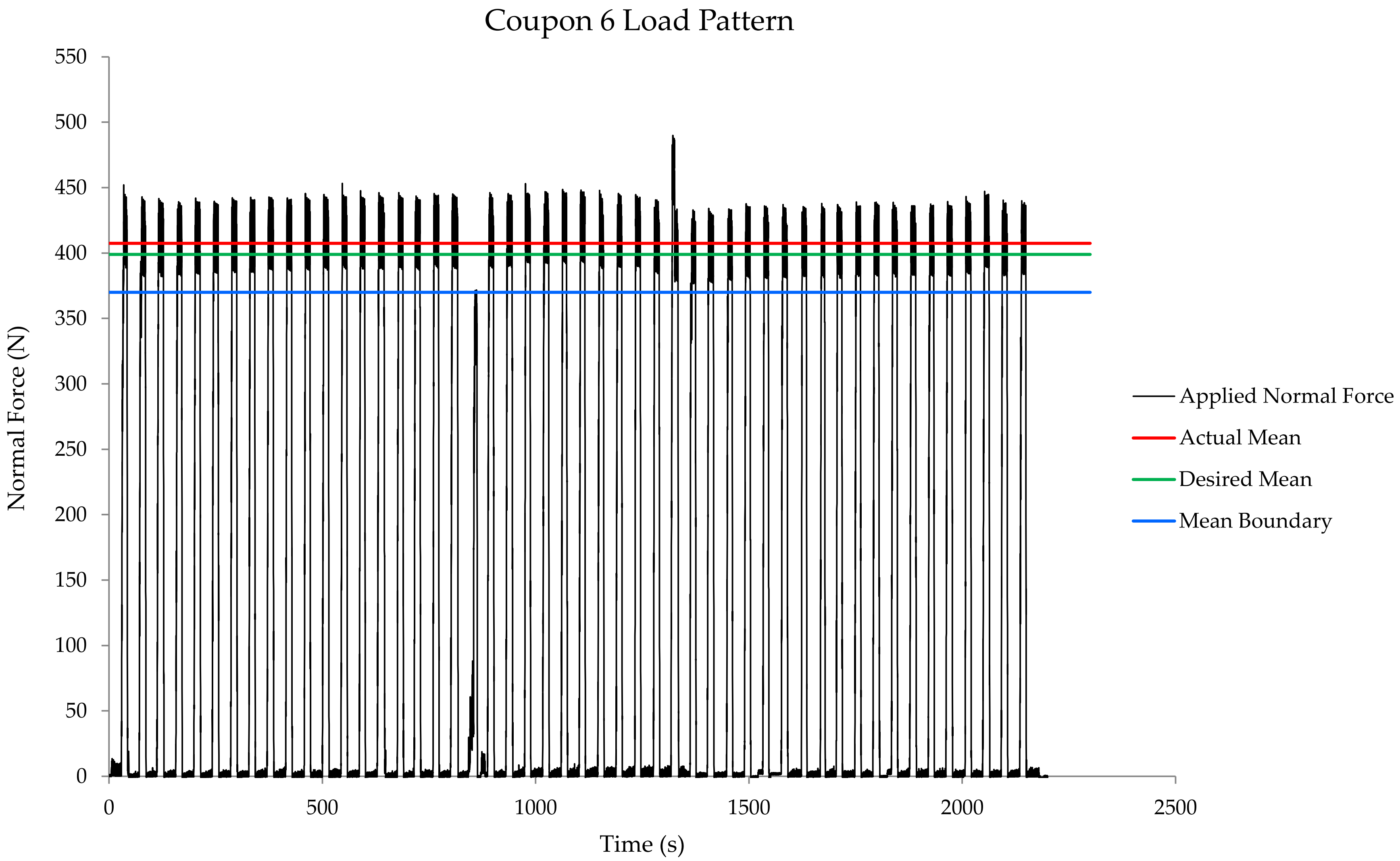
Coupon 6 Load Pattern
Normal Force (N)
550
500
450
400
350
300
250
200
150
100
50
0
0
500
1000
1500
2000
2500
Time (s)
Applied Normal Force
Actual Mean
Desired Mean
Mean Boundary

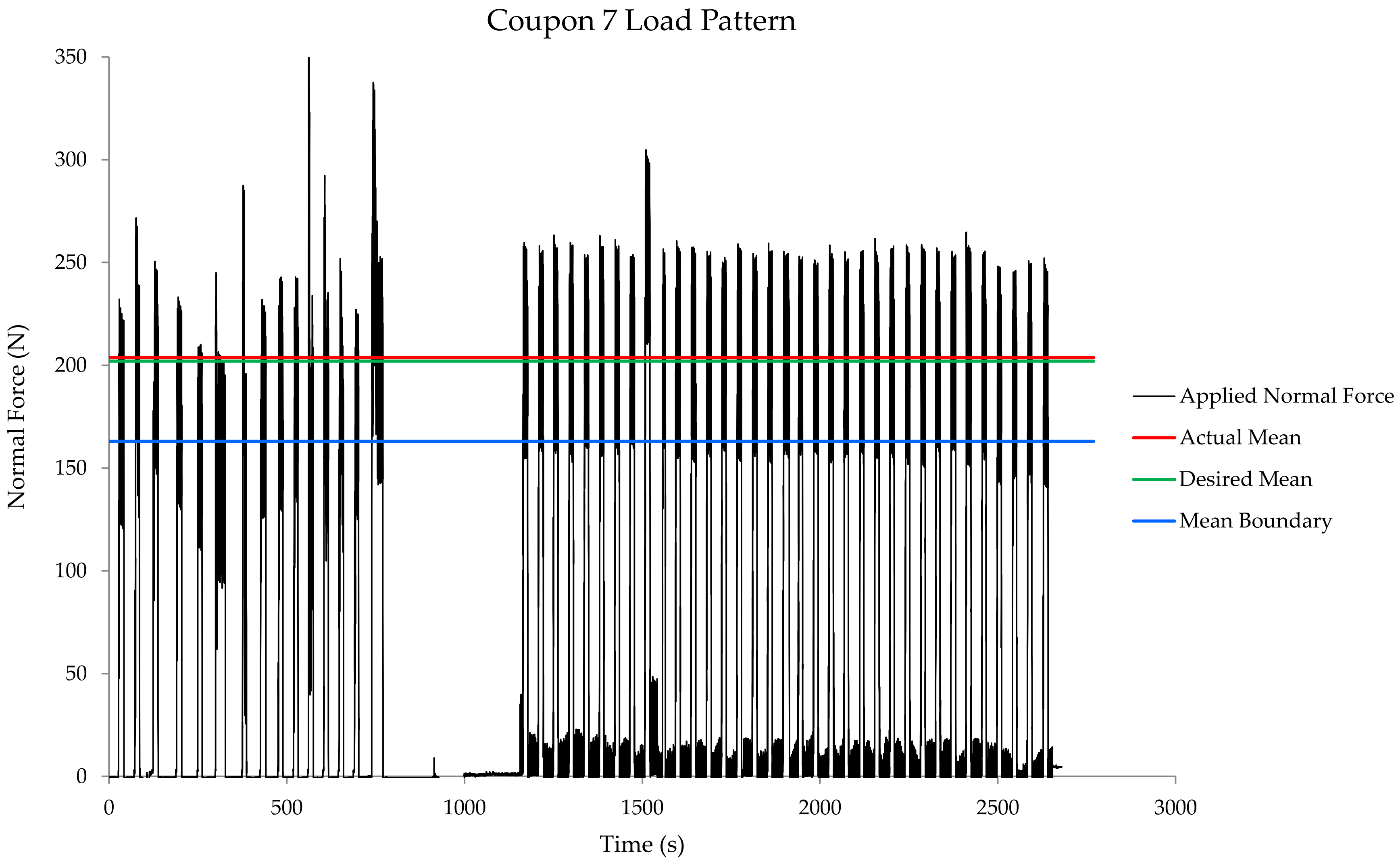
Coupon 7 Load Pattern
Normal Force (N)
350
300
250
200
150
100
50
0
0
500
1000
1500
2000
2500
3000
Time (s)
Applied Normal Force
Actual Mean
Desired Mean
Mean Boundary

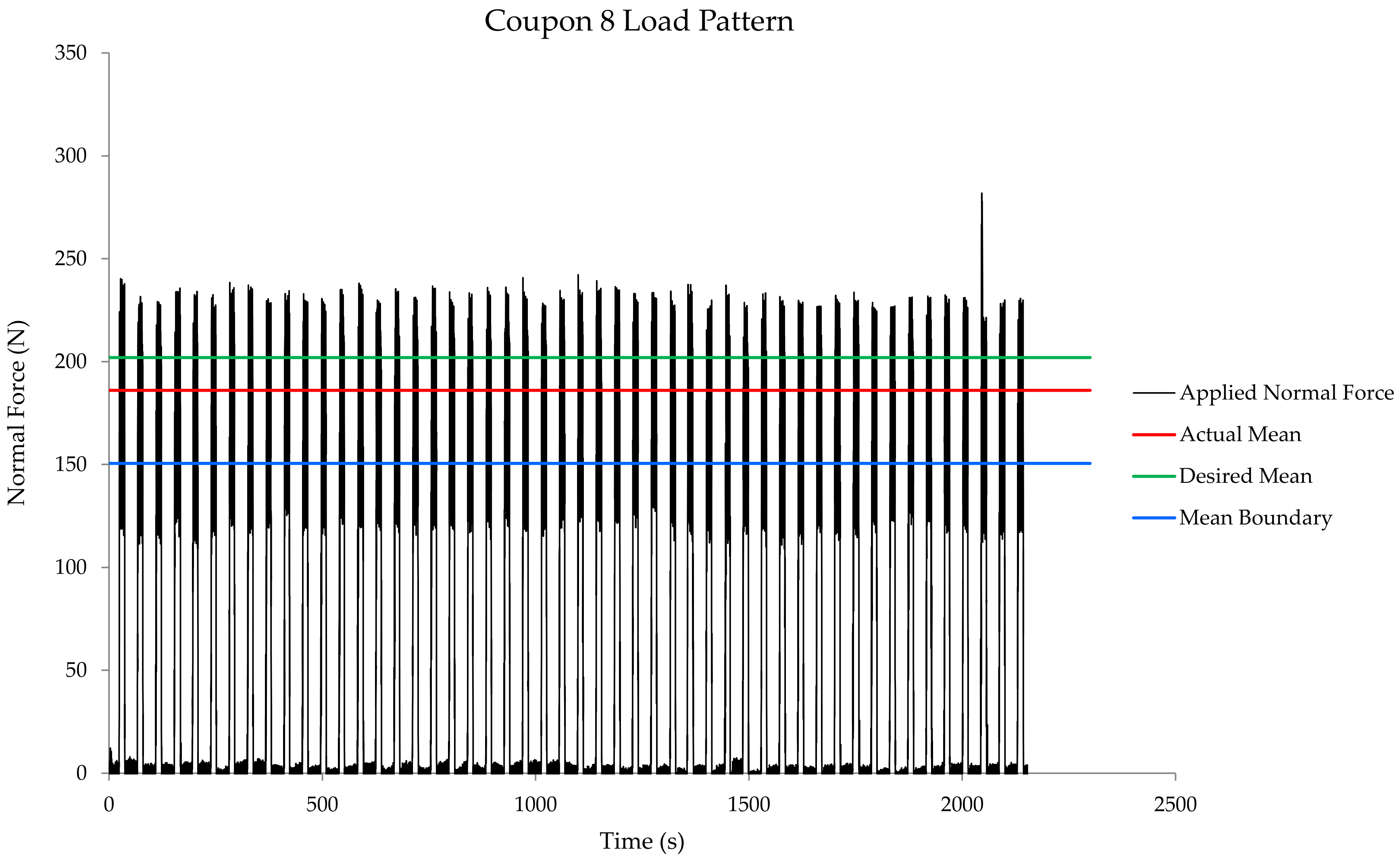
Coupon 8 Load Pattern
Normal Force (N)
350
300
250
200
150
100
50
0
0
500
1000
1500
2000
2500
Time (s)
Applied Normal Force
Actual Mean
Desired Mean
Mean Boundary

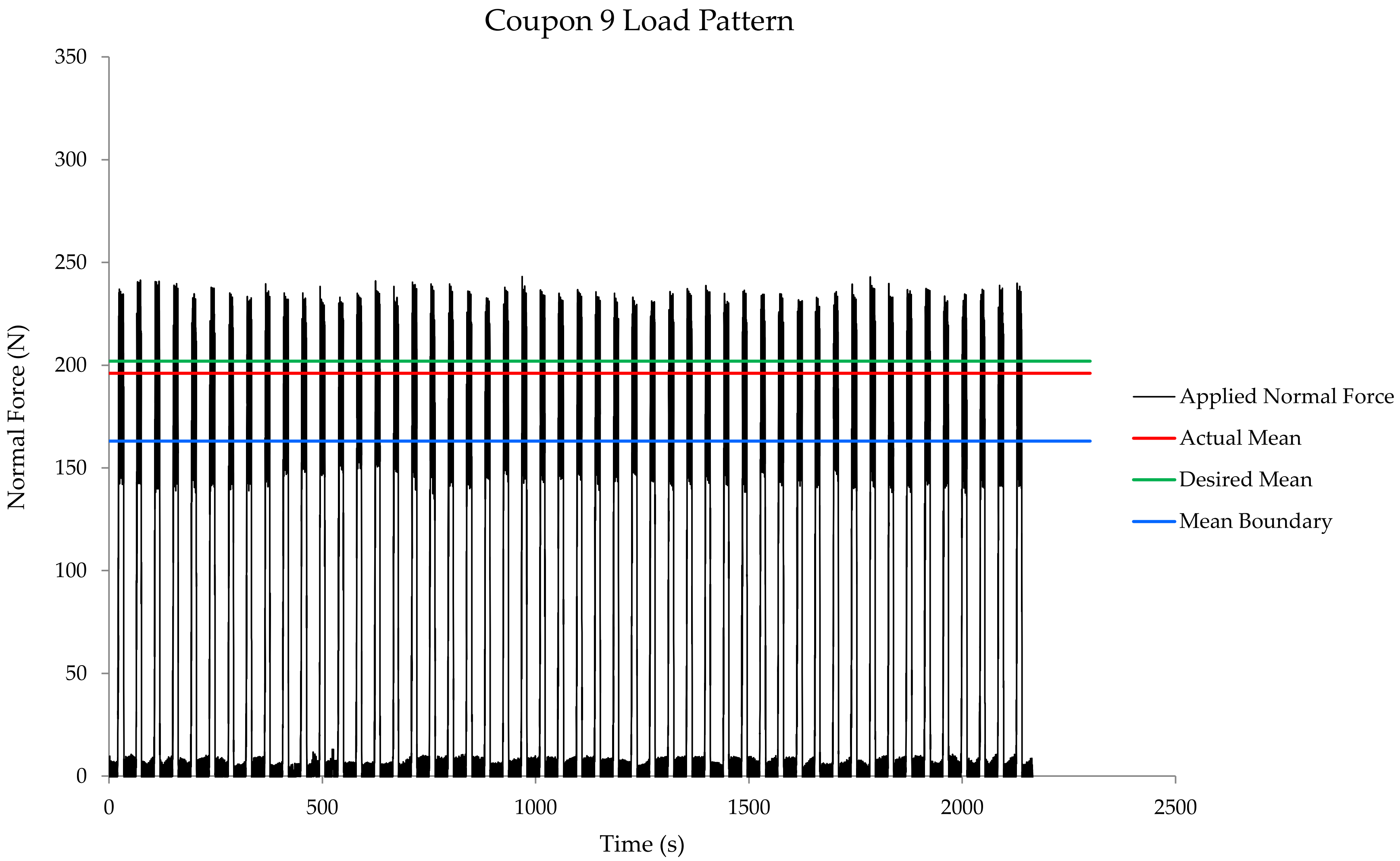
Coupon 9 Load Pattern
Normal Force (N)
350
300
250
200
150
100
50
0
0
500
1000
1500
2000
2500
Time (s)
Applied Normal Force
Actual Mean
Desired Mean
Mean Boundary

Appendix E – Additional Power Draw Graphs

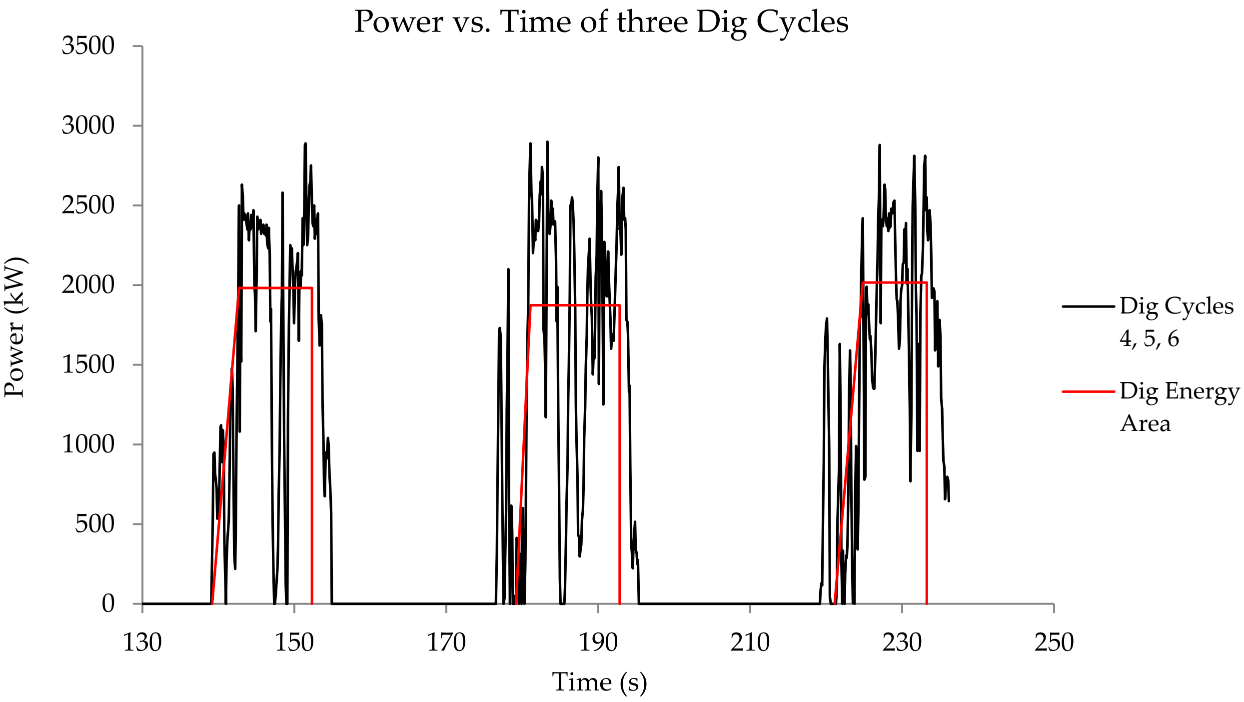

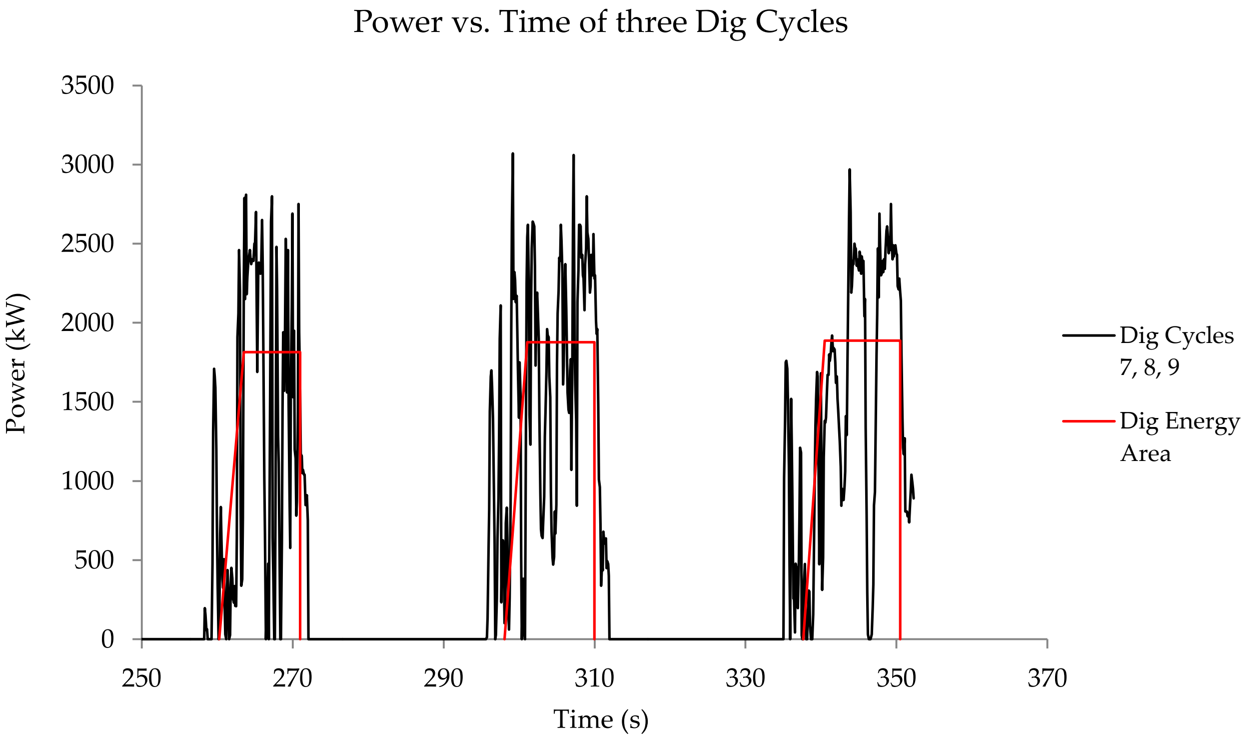

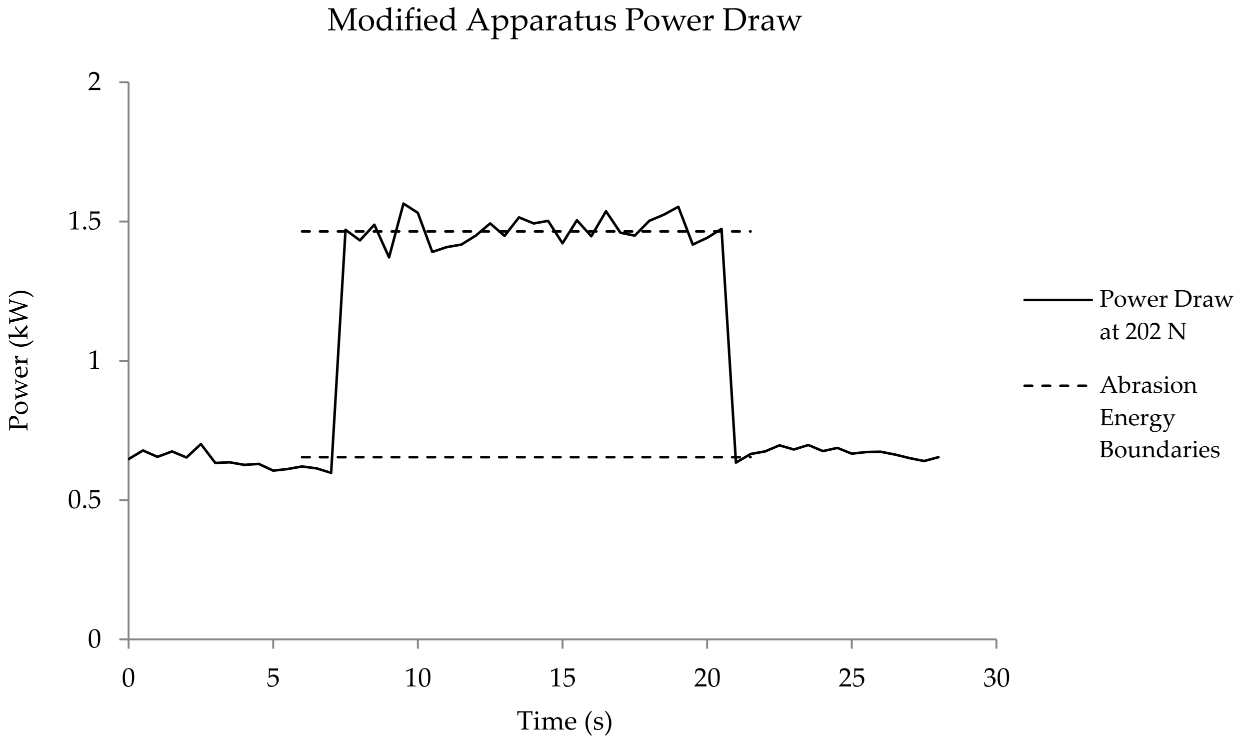
Modified Apparatus Power Draw
Power (kW)
2
1.5
1
0.5
0
Time (s)
0
5
10
15
20
25
30
Power Draw at 202 N
Abrasion Energy Boundaries

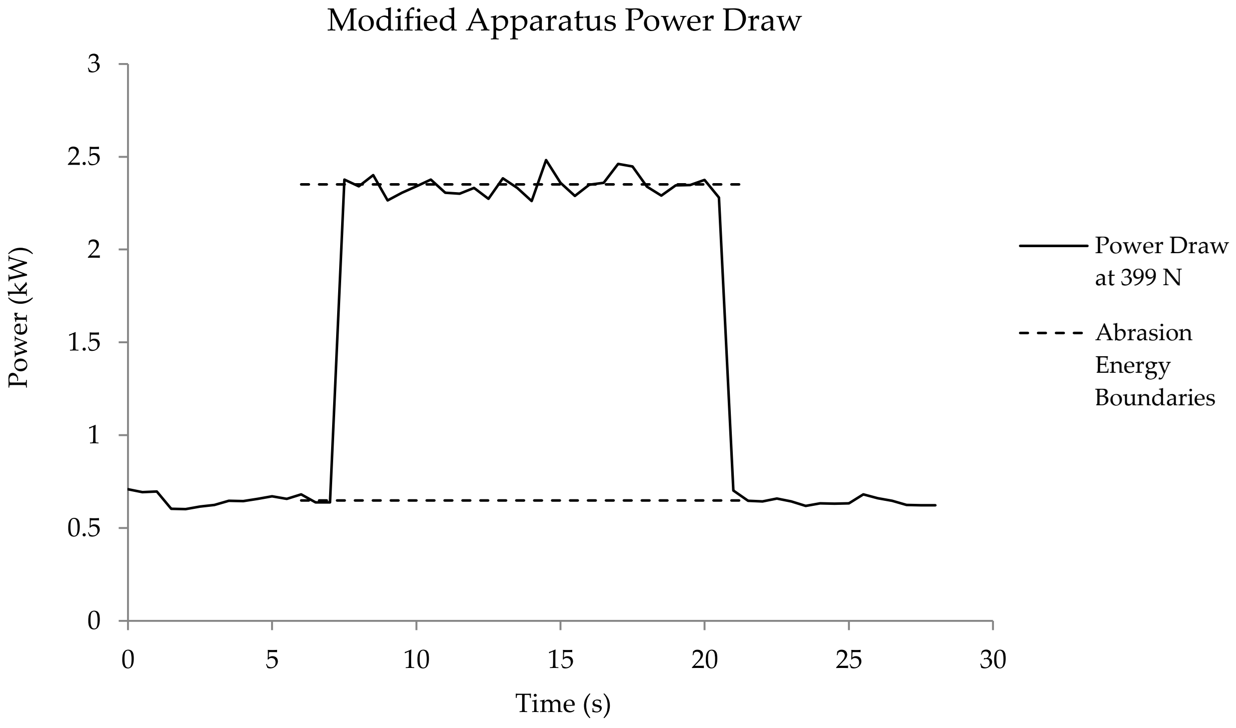
Modified Apparatus Power Draw
Power (kW)
3
2.5
2
1.5
1
0.5
0
Time (s)
0
5
10
15
20
25
30
Power Draw at 399 N
Abrasion Energy Boundaries

Appendix F – Additional Field Wear Predictions

Additional results from the field tooth life predictions of the cyclical loading tests are reported. All values reported below are in hours. The Tables are organized top to bottom with respect to the average peak force categories of 202 N, 301 N, and 399 N. The values are predictions based off of the 8 hour wear volume measured from the field teeth in the lab. Bold values are reported in the Results section. Availability is listed vertically, and the utilization values are listed horizontally.

			- σ Force – 8 hour predictions					
A′ / *U′*	0.8	0.81	0.82	0.83	0.84	0.85	0.86	0.87
0.9	5.76	5.69	5.62	5.55	5.49	5.42	5.36	5.30
0.91	5.70	5.63	5.56	5.49	5.43	5.36	5.30	5.24
0.92	**5.64**	5.57	5.50	5.43	5.37	5.31	5.24	5.18
0.93	5.58	5.51	5.44	5.38	5.31	5.25	5.19	5.13
0.94	5.52	5.45	5.38	5.32	5.25	5.19	5.13	5.07
0.95	5.46	5.39	5.33	5.26	5.20	5.14	5.08	5.02

			301 N Force – 8 hour predictions					
A′ / *U′*	0.8	0.81	0.82	0.83	0.84	0.85	0.86	0.87
0.9	5.44	5.38	5.31	5.25	5.18	5.12	5.06	5.01
0.91	5.38	5.32	5.25	5.19	5.13	5.07	5.01	4.95
0.92	**5.33**	5.26	5.20	5.13	5.07	5.01	4.95	4.90
0.93	5.27	5.20	5.14	5.08	5.02	4.96	4.90	4.84
0.94	5.21	5.15	5.09	5.02	4.96	4.91	4.85	4.79
0.95	5.16	5.09	5.03	4.97	4.91	4.85	4.80	4.74

			+ σ Force – 8 hour predictions					
A′ / *U′*	0.8	0.81	0.82	0.83	0.84	0.85	0.86	0.87
0.9	6.89	6.80	6.72	6.64	6.56	6.48	6.41	6.33
0.91	6.81	6.73	6.65	6.57	6.49	6.41	6.34	6.26
0.92	**6.74**	6.65	6.57	6.49	6.42	6.34	6.27	6.20
0.93	6.67	6.58	6.50	6.42	6.35	6.27	6.20	6.13
0.94	6.59	6.51	6.43	6.36	6.28	6.21	6.13	6.06
0.95	6.53	6.44	6.37	6.29	6.21	6.14	6.07	6.00

Additional results from the field tooth life predictions of the cyclical loading tests are reported. All values reported below are in hours. The Tables are organized top to bottom with respect to the average peak force categories of 202 N, 301 N, and 399 N. The values are predictions based off of the 18 hour wear volume measured from the field teeth in the lab. Bold values are reported in the Results section. Availability is listed vertically, and the utilization values are listed horizontally.

			- σ Force – 18 hour predictions					
A′ / *U′*	0.8	0.81	0.82	0.83	0.84	0.85	0.86	0.87
0.9	14.41	14.23	14.06	13.89	13.72	13.56	13.40	13.25
0.91	14.25	14.07	13.90	13.73	13.57	13.41	13.25	13.10
0.92	**14.09**	13.92	13.75	13.58	13.42	13.27	13.11	12.96
0.93	13.94	13.77	13.60	13.44	13.28	13.12	12.97	12.82
0.94	13.79	13.62	13.46	13.30	13.14	12.98	12.83	12.68
0.95	13.65	13.48	13.32	13.16	13.00	12.85	12.70	12.55

			301 N Force – 18 hour predictions					
A′ / *U′*	0.8	0.81	0.82	0.83	0.84	0.85	0.86	0.87
0.9	13.61	13.44	13.28	13.12	12.96	12.81	12.66	12.51
0.91	13.46	13.29	13.13	12.97	12.82	12.67	12.52	12.38
0.92	**13.31**	13.15	12.99	12.83	12.68	12.53	12.38	12.24
0.93	13.17	13.01	12.85	12.69	12.54	12.40	12.25	12.11
0.94	13.03	12.87	12.71	12.56	12.41	12.26	12.12	11.98
0.95	12.89	12.73	12.58	12.43	12.28	12.13	11.99	11.86

			+ σ Force – 18 hour predictions					
A′ / *U′*	0.8	0.81	0.82	0.83	0.84	0.85	0.86	0.87
0.9	17.22	17.01	16.80	16.60	16.40	16.21	16.02	15.83
0.91	17.03	16.82	16.61	16.41	16.22	16.03	15.84	15.66
0.92	**16.84**	16.64	16.43	16.24	16.04	15.85	15.67	15.49
0.93	16.66	16.46	16.26	16.06	15.87	15.68	15.50	15.32
0.94	16.49	16.28	16.08	15.89	15.70	15.52	15.34	15.16
0.95	16.31	16.11	15.91	15.72	15.54	15.35	15.17	15.00

Additional results from the field tooth life predictions of the constant loading tests are reported. All values reported below are in hours. The values are predictions based off of the 8 hour (top Table) and 18 hour (bottom Table) wear volume measured from the field teeth in the lab. Bold values are reported in the Results section. Availability is listed vertically, and the utilization values are listed horizontally.

			Constant Load 8 hour predictions					
A′ / *U′*	0.8	0.81	0.82	0.83	0.84	0.85	0.86	0.87
0.9	1.93	1.91	1.89	1.86	1.84	1.82	1.80	1.78
0.91	1.91	1.89	1.87	1.84	1.82	1.80	1.78	1.76
0.92	**1.89**	1.87	1.85	1.82	1.80	1.78	1.76	1.74
0.93	1.87	1.85	1.83	1.80	1.78	1.76	1.74	1.72
0.94	1.85	1.83	1.81	1.78	1.76	1.74	1.72	1.70
0.95	1.83	1.81	1.79	1.77	1.74	1.72	1.70	1.68

			Constant Load 18 hour predictions					
A′ / *U′*	0.8	0.81	0.82	0.83	0.84	0.85	0.86	0.87
0.9	4.83	4.77	4.72	4.66	4.60	4.55	4.50	4.44
0.91	4.78	4.72	4.66	4.61	4.55	4.50	4.45	4.40
0.92	**4.73**	4.67	4.61	4.56	4.50	4.45	4.40	4.35
0.93	4.68	4.62	4.56	4.51	4.45	4.40	4.35	4.30
0.94	4.63	4.57	4.51	4.46	4.41	4.36	4.30	4.26
0.95	4.58	4.52	4.47	4.41	4.36	4.31	4.26	4.21